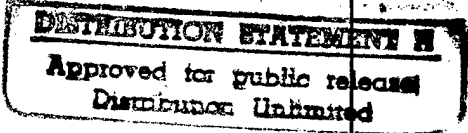


REPORT DOCUMENTATION PAGE			Form Approved OMB No. 0704-0188	
Public reporting burden for this collection of information is estimated to average 1 hour per response, including the time for reviewing instructions, searching existing data sources, gathering and maintaining the data needed, and completing and reviewing the collection of information. Send comments regarding this burden estimate or any other aspect of this collection of information, including suggestions for reducing this burden, to Washington Headquarters Services, Directorate for Information Operations and Reports, 1215 Jefferson Davis Highway, Suite 1204, Arlington, VA 22202-4302, and to the Office of Management and Budget, Paperwork Reduction Project (0704-0188), Washington, DC 20503.				
1. AGENCY USE ONLY (Leave blank)		2. REPORT DATE 15 Dec 97	3. REPORT TYPE AND DATES COVERED	
4. TITLE AND SUBTITLE The Electrodeposition of Cobalt, Iron, and Antimony and their Aluminum Alloys from Room-Temperature Aluminum Chloride 1-Methyl-3-Ethylimidazolium Chloride Molten Salt			5. FUNDING NUMBERS	
6. AUTHOR(S) John A. Mitchell				
7. PERFORMING ORGANIZATION NAME(S) AND ADDRESS(ES) The University of Mississippi			8. PERFORMING ORGANIZATION REPORT NUMBER 97-035D	
9. SPONSORING/MONITORING AGENCY NAME(S) AND ADDRESS(ES) THE DEPARTMENT OF THE AIR FORCE AFIT/CI, BLDG 125 2950 P STREET WPAFB OH 45433			10. SPONSORING/MONITORING AGENCY REPORT NUMBER	
11. SUPPLEMENTARY NOTES				
12a. DISTRIBUTION AVAILABILITY STATEMENT Unlimited Distribution In Accordance With AFI 35-205/AFIT Sup 1			12b. DISTRIBUTION CODE	
				
13. ABSTRACT (Maximum 200 words)				
<p style="font-size: 2em; margin: 0;">19971230 159</p> <p style="font-size: 1.2em; margin: 0;">DDIC QUALITY INSTANT</p>				
14. SUBJECT TERMS			15. NUMBER OF PAGES 133	
			16. PRICE CODE	
17. SECURITY CLASSIFICATION OF REPORT	18. SECURITY CLASSIFICATION OF THIS PAGE	19. SECURITY CLASSIFICATION OF ABSTRACT	20. LIMITATION OF ABSTRACT	

To the Graduate Council:

I am submitting herewith a dissertation written by John A. Mitchell entitled "The Electrodeposition of Cobalt, Iron, Antimony and their Aluminum Alloys from Acidic Aluminum Chloride-1-Methyl-3-ethylimidazolium Chloride Room Temperature Molten Salts." I have examined the final copy of this dissertation for form and content and recommend that it be accepted in partial fulfillment of the requirements for the degree of Doctor of Philosophy, with a major in chemistry.

Dr. Charles L. Hussey, Professor and Chairman
Department of Chemistry

We have read this dissertation
and recommend its acceptance:

Dr. Jon F. Parcher, Professor of Chemistry

Dr. David E. Graves, Professor of Chemistry

Dr. Steven R. Davis, Professor of Chemistry

Dr. Allen B. Jones , Professor and Chair of Pharmaceutics

Dr. Michael R. Dingerson, Dean of the Graduate School and
Associate Vice-Chancellor for Research

STATEMENT OF PERMISSION TO USE

In presenting this dissertation in partial fulfillment of the requirements for a Doctor of Philosophy degree at The University of Mississippi, I agree that the Library shall make it available to borrowers under the rules of the Library. Brief quotations from this dissertation are allowable without special permission, provided that accurate acknowledgment of the source is made.

Permission for extensive quotation from or reproduction of this dissertation may be granted by my major professor, or in his absence, by the Head of Interlibrary Services when, in the opinion of either, the proposed use of the material is for scholarly purposes. Any copying or use of the material in this dissertation for financial gain shall not be allowed without my written permission.

Signature _____

Date _____

**The Electrodeposition of Cobalt, Iron, and Antimony and their Aluminum Alloys
from Room-Temperature Aluminum Chloride 1-Methyl-3-Ethylimidazolium
Chloride Molten Salt**

**A Dissertation
Presented for the
Doctor of Philosophy
Degree
The University of Mississippi**

John A. Mitchell

December, 1997

For my parents, to whom I will always be indebted.

For my Special Forces instructors, to whom I am eternally grateful.

ACKNOWLEDGMENTS

I would like to express my sincere gratitude to Dr. Charles L. Hussey for all his encouragement and guidance. This work represents the many hours of ceaseless support and education he has given me.

I would like to thank the members of my dissertation committee, Dr. Steven Davis, Dr. David Graves, Dr. Jon Parcher, and Dr. Allen Jones, for their patient advice and assistance.

Many thanks are due to Dr. Gery R. Stafford at the Materials Science and Engineering Laboratory of the National Institute of Standards and Technology, Gaithersburg, Maryland, for his collaboration. He was instrumental in performing the characterization of the metal-aluminum alloy electrodeposits and assisting us in the characterization of the cobalt-aluminum alloys.

I would like to thank Dr. Ellen Lackey in the School of Engineering for the characterization of my zinc deposits the University of Mississippi SEM/EDS facility.

I also thank my colleagues, Dr. Bobbie Joe Clark, Dr. William R. Pitner, Dr. Charles Rajaram Sabapathy, Mr. Montray C. Leavy, Ms. Gemma Stewart, and especially Mr. Brian, J. Tierney, who made my education possible and enjoyable.

ABSTRACT

The electrodeposition of cobalt, iron, antimony, and their aluminum alloys was investigated in the room-temperature molten salt, aluminum chloride-1-methyl-3-ethylimidazolium chloride ($\text{AlCl}_3\text{-MeEtimCl}$). Solutions of Co(II), Fe(II), and Sb(III) were prepared by controlled-potential coulometric anodization of the respective metal in Lewis acidic melt. The plating and stripping of these metals was investigated using cyclic voltammetry, rotating disk and rotating ring-disk electrode voltammetry, controlled potential coulometry, and potential step chronoamperometry. Bulk deposits of the pure and aluminum-alloyed metals were analyzed using scanning electron microscopy, energy dispersive x-ray spectroscopy, atomic absorption spectroscopy, and x-ray diffraction methods.

The underpotential co-deposition of aluminum was observed during the electrodeposition of cobalt and iron; however, this phenomenon did not occur during the electrodeposition of antimony. The results of this investigation suggest that both a positive work function difference between the transition metal and aluminum and the mutual solubility of these components determine whether or not the co-deposition of aluminum takes place.

Two electroanalytical techniques were developed for the analysis of co-deposited aluminum alloys: the first was based on anodic linear sweep voltammetry at a rotating-ring-disk electrode. The second was derived from the transition metal ion concentration

changes observed during bulk deposition experiments. In the first technique, an alloy deposit was stripped from the disk electrode while the ring potential was held at a value where only one of the ions oxidized from the alloy could be reduced. In the second technique, the concentration of transition metal ions was monitored in an undivided cell with an anode made from the depositing metal. The co-deposition of aluminum was signalled by an increase in the transition metal ion concentration. The alloy composition data resulting from both techniques were in excellent agreement with that obtained from the analysis of partial currents by means of sampled-current voltammetry.

Chronoamperometry was used to study the nucleation of antimony and iron on glassy carbon substrates. The electrodeposition of these metals was found to involve three-dimensional nucleation with hemispherical diffusion-controlled growth of the nuclei. Comparison of the experimental dimensionless current-time transients with theoretical transients indicated that the nucleation of iron followed a progressive mechanism whereas the nucleation of antimony followed a progressive mechanism at a finite number of active sites. Analysis of the potential dependence of the nucleation rate according to the Atomistic Theory of Nucleation suggested that active sites on the glassy carbon substrate act as critical nuclei.

The formal potentials of the Co(II)/Co, Fe(II)/Fe, and Sb(III)/Sb couples were found to be: 0.86 ± 0.02 , 0.52 ± 0.01 , and 1.02 ± 0.03 V, respectively, in the 60.0-40.0 m/o AlCl₃-MeEtimCl molten salt at 25 °C. The diffusion coefficients of cobalt(II), iron(II), and antimony(III) were found to be: $(3.4 \pm 0.1) \times 10^{-7}$; $(2.6 \pm 0.3) \times 10^{-6}$; and $(1.1 \pm 0.1) \times 10^{-6}$ cm² s⁻¹, respectively.

TABLE OF CONTENTS

LIST OF TABLES.....	xii
LIST OF FIGURES.....	xiv
LIST OF SYMBOLS.....	xix
CHAPTER	PAGE
I	
INTRODUCTION.....	1
1.1 Room-temperature haloaluminate ionic liquids.....	2
1.1.1 History and background.....	2
1.1.2 Acid-Base properties of the $\text{AlCl}_3\text{-MeEtimCl}$ molten salt	4
1.1.3 Physical and electrochemical properties of the $\text{AlCl}_3\text{-MeEtimCl}$ molten salts.....	7
1.1.4 Electrodeposition of metals and alloys from both high temperature and room-temperature chloroaluminate melts.....	11
1.1.5 Fundamentals of the electrodeposition of metals.....	14
1.1.6 Three-dimensional nucleation.....	18
1.2 Objective.....	24
II EXPERIMENTAL.....	26
2.1 Chemicals.....	26

2.2	Equipment.....	27
2.2.1	Electrochemical cells and electrodes.....	28
2.2.2	Analysis of bulk deposits.....	30
2.3	Electrochemical techniques.....	30
III.	ELECTRODEPOSITION OF COBALT.....	39
3.1	Anodization of cobalt.....	39
3.2	Cyclic and rotating disk electrode voltammetry of cobalt(II).....	41
3.3	Sampled-current voltammetry for the reduction of cobalt(II).....	46
3.4	Underpotential deposition of cobalt.....	49
3.5	Analysis of cobalt-aluminum thin films by anodic linear sweep voltammetry.....	54
IV.	ELECTRODEPOSITION OF IRON.....	63
4.1	Anodic dissolution of iron.....	63
4.2	Voltammetry of iron(II).....	63
4.3	Sampled-current voltammetry of iron(II).....	73
4.4	Analysis of iron-aluminum thin films by anodic linear sweep voltammetry.....	75
4.5	Underpotential deposition of aluminum on iron.....	82
4.6	Nucleation of iron on glassy carbon.....	82
4.7	Bulk deposition experiments.....	87
4.8	Characterization of bulk iron deposits by SEM-EDS.....	89
V.	ELECTRODEPOSITION OF ANTIMONY.....	63
5.1	Anodic dissolution of antimony.....	96

5.2 Voltammetry of antimony(III).....	96
5.3 Sampled-current voltammetry of antimony(III).....	105
5.4 Nucleation of antimony on glassy carbon.....	110
5.5 Characterization of bulk antimony deposits.....	116
VI. SUMMARY AND CONCLUSIONS.....	122
LIST OF REFERENCES.....	127
BIOGRAPHICAL SKETCH OF THE AUTHOR.....	134

LIST OF TABLES

TABLE.....	PAGE
1.1 Mathematical models describing kinetic and diffusion controlled three dimensional nucleation.....	19
3.1 Results for the anodization of cobalt	40
4.1 Results for the anodization of iron	64
4.2 Cyclic voltammetric data for the reduction of Fe(II).....	70
4.3 Nucleation data for the electrodeposition of iron on glassy carbon.....	86
5.1 Results for the anodization of antimony electrodes.....	97
5.2 Cyclic voltammetric data for the reduction of Sb(III).....	104
5.3 Nucleation data for the electrodeposition of antimony on glassy carbon.....	113
6.1 Summary of different electrodeposition mechanisms.....	124
6.2 Formal potentials of redox couples studied in this research....	126
6.3 Diffusion coefficients and Stokes-Einstein products	126

LIST OF FIGURES

FIGURE	PAGE
1.1	Structure of room-temperature molten salts.....5
1.2	Distribution of the anionic species as a function of composition.....6
1.3	Phase diagram for the AlCl_3 -MeEtimCl molten salt system.....8
1.4	Electrochemical potential window for the AlCl_3 -MeEtimCl molten salt system.....10
1.5	Crystal growth mechanisms for overpotential and underpotential deposition.....16
1.6	Schematic diagram of a typical chronoamperometric experiment.....21
2.1	Typical cyclic voltammograms.....34
2.2	Comparison between stationary and rotating electrode voltammetry.....36
3.1	Voltammograms of cobalt(II) at platinum.....42
3.2	Voltammograms of cobalt(II) at gold.....43
3.3	Voltammograms of cobalt(II) at tungsten.....44
3.4	Voltammograms of cobalt(II) at glassy carbon.....45
3.5	Sampled-current voltammograms for the reduction of Co(II) at platinum.....47
3.6	Plot of $\text{Co}_x\text{Al}_{1-x}$ alloy composition as a function of potential.....50
3.7	Underpotential deposition of cobalt(II) at platinum and gold.....51
3.8	Underpotential deposition of aluminum on a cobalt electrode.....53

3.9	Dependence of $\text{Co}_x\text{Al}_{1-x}$ deposit composition on deposition charge.....	57
3.10	Variation of the $\text{Co}_x\text{Al}_{1-x}$ alloy composition with immersion time.....	58
3.11	Disk and ring voltammograms at a Pt-RRDE.....	59
3.12	Disk and ring voltammograms at a Pt-RRDE.....	60
4.1	Voltammograms of cobalt(II) at platinum.....	66
4.2	Voltammograms of cobalt(II) at tungsten.....	67
4.3	Voltammograms of cobalt(II) at gold.....	68
4.4	Voltammograms of cobalt(II) at glassy carbon.....	69
4.5	Plot of j_1 versus $\omega^{1/2}$ for the reduction of Fe(II).....	72
4.6	Sampled-current voltammograms for the reduction of Fe(II) at platinum.....	74
4.7	Composition of $\text{Fe}_x\text{Al}_{1-x}$ as a function of potential.....	76
4.8	Disk and ring voltammograms at a Pt-RRDE.....	79
4.9	Disk and ring voltammograms at a Pt-RRDE.....	80
4.10	Underpotential deposition of aluminum onto iron.....	83
4.11	Current-time transients for the reduction of Fe(II) at glassy carbon.....	85
4.12	Plot of $\log A_r N_o$ versus overpotential.....	88
4.13	SEM images of iron, constant potential.....	91
4.14	SEM images of iron, constant potential.....	92
4.15	SEM images of iron, constant current.....	93
4.16	SEM images of iron, constant current.....	94
5.1	Voltammograms of antimony(III) at platinum.....	99
5.2	Voltammograms of antimony(III) at tungsten.....	100

5.3	Voltammograms of antimony(III) at gold.....	101
5.4	Voltammograms of antimony(III) at glassy carbon.....	102
5.5	Plot of j_1 versus $\omega^{1/2}$ for the reduction of Sb(III).....	106
5.6	Sampled-current voltammogram for the reduction of Sb(III).....	108
5.7	Underpotential deposition of aluminum onto antimony.....	109
5.8	Plot of j_1 versus $t^{-1/2}$ for the reduction of Sb(III).....	111
5.9	Current-time transients for the reduction of Sb(III) at glassy carbon.....	112
5.10	Plot of $\log i_0$ versus overpotential for Sb(III).....	114
5.11	Plot of N_0 , A_0 , and $N_0 A_0$ versus overpotential.....	117
5.12	SEM images of antimony, constant potential.....	119
5.13	SEM images of antimony, constant current.....	120

LIST OF SYMBOLS

- A : electrode surface area, cm^2
- A_t : first-order nucleation rate constant, s^{-1}
- C_0^* : bulk concentration of reactant species, mol cm^{-3}
- D_0 : diffusion coefficient of species O, $\text{cm}^2 \text{s}^{-1}$
- e : elementary charge, $1.60219 \times 10^{-19} \text{ C}$
- E_{app} : applied potential, V
- E° : standard potential, V
- $E^{\circ'}$: Formal potential, V
- E_p^a : anodic voltammetric peak potential, V
- E_p^c : cathodic voltammetric peak potential, V
- E_p : UPD stripping potential, V
- ΔE_p : underpotential shift ($E_p - E_p^a$), V
- $E_{p/2}$: voltammetric half-peak potential, V
- F : Faraday constant, 96485 C eqv^{-1}
- $g(t)$: number density of growth centers, cm^{-2}
- i_p^a : anodic voltammetric peak current, A
- i_p^c : cathodic voltammetric peak current, A
- $(i_p^c)_0$: uncorrected cathodic voltammetric peak current, A
- i_1 : (a) rotating-disk electrode voltammetric limiting current, A
: (b) current-sampled voltammetric limiting current, A

- i_M : maximum of current-time transient, A
 i_λ : current at E_λ , A
 j : current density (i/A), A cm⁻²
 j_l : limiting current density (i_l/A), A cm⁻²
 k : Boltzmann constant, 1.38066×10^{-23} J K⁻¹
 K_{eq} : equilibrium constant
 m : number of moles, mol
m/o : mole percent
 M : symbol for a metal atom
 M_{ad} : symbol for a metal atom adsorbed on a substrate
 M : molecular weight, g mol⁻¹
 n : number of electrons associated with an electron reaction, eqv mol⁻¹
 N_0 : number density of nuclei, cm⁻²
 n_c : critical nucleus
 O : oxidized species
 Q : charge, C
 R : reduced species
 R : Avogadro's number, 8.31441 J mol⁻¹ K⁻¹
 S : symbol for a substrate
 t : time, s
 t_s : sampling time for current-sampled voltammetry
 t_M : time corresponding to i_M

- T : temperature, K
- V : volume of solution, L
- Δw_M : weight change of the metal anode M, g
- x : dimensionless parameter containing information about the nucleation rate
- z : charge of the metal ion
- α : (a) dimensionless parameter containing information about the nucleation rate
: (b) transfer coefficient
- η : overpotential, V
- η : absolute viscosity, $\text{g cm}^{-1} \text{s}^{-1}$
- γ : kinematic viscosity, $\text{cm}^2 \text{s}^{-1}$
- v : linear potential scan (sweep) rate, V s^{-1}
- ρ : density, g cm^{-3}
- χ_{Al} : mole fraction of aluminum chloride
- ω : angular velocity (rotation rate) of a rotating-disk electrode, s^{-1} (or rad s^{-1})

CHAPTER I. INTRODUCTION

The worldwide consumption of aluminum is now in the tens of millions of tons and on the rise each year (1). The aluminum industry is the world's largest electrochemical industry. It accounts for more than 12% of all the electricity used in the world through the Hall-Heroult process for aluminum production. These facts alone establish aluminum as an important industrial material that must possess some very desirable physical, chemical and metallurgical properties.

Aluminum is the most abundant metallic element on the surface of the earth and is the most widely used nonferrous metal. It is light; its density is about one third that of iron. In its alloyed form, it is soft and ductile. Aluminum forms a self-protecting oxide layer and is therefore highly resistant to corrosion, even upon exposure to chloride-containing media such as sea water. It can be hardened and made more corrosion resistant by alloying with other metals, e.g., magnesium and transition metals such as cobalt, copper, and zinc. It has high electrical and thermal conductivity and is an indispensable construction material for the electronics, automotive, and aerospace industry. In this era of environmental concerns, it is significant that aluminum poses no serious health hazards.

Electrodeposition is a common technique for creating metal alloy films from aqueous solutions. Unlike solidification, the electrodeposition of alloys usually leads to materials with a more uniform composition and structure. Aluminum-transition metal alloys may be used

to make strong, lightweight, anti-corrosive structures, materials with unusual magnetic properties, and other materials of technological significance. Despite their importance, very little research has been focused on the electrodeposition of aluminum alloys due to the negative potential of the Al(III)/Al couple in aqueous solution (-1.66 V versus the normal hydrogen electrode, NHE); the deposition of aluminum from aqueous media is not practical because hydrogen is evolved before Al(III) is reduced (2).

The incorporation of hydrogen into the atomic structure of alloys made by aqueous electrodeposition leads to materials with adverse properties (3), including defects in the structure of these materials (4-6). The evolution and co-deposition of hydrogen also leads to a loss in current efficiency during the plating process. The problem caused by hydrogen evolution and co-deposition can often be avoided by the use of plating baths based on aprotic, nonaqueous solvents. The need for a low melting liquid medium from which aluminum can be electrodeposited has led to the development of the class of ionic liquids known today as room-temperature haloaluminate molten salts.

1.1 Room-Temperature Haloaluminate Molten Salts

1.1.1 History and Background

Room-temperature haloaluminate molten salts or more appropriately ionic liquids, are made by combining aluminum chloride with various quaternary ammonium halide salts. The first of these ionic liquids, a mixture of N-ethylpyridinium bromide and aluminum chloride, was used by Hurley and Wier in 1951 for the electrodeposition of aluminum (7-11). This system proved to be the model for the room-temperature molten salts used today. However,

the N-ethylpyridinium bromide system has three disadvantages: it is susceptible to photodecomposition, the N-ethylpyridinium cation is quite easily reduced, and the melt is a liquid over a narrow composition range. Other binary molten salts with improved chemical and physical properties were designed based on this model of a quaternary organic halide salt combined with an aluminum halide.

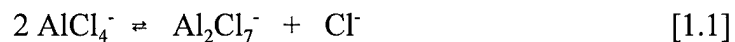
In 1978, Carpio *et al.*(12), found that if the organic component was a 1-(alkyl)pyridinium chloride salt instead of a bromide salt, then the resulting room-temperature molten salt had improved properties. For example, melts made from AlCl_3 and 1-(1-butyl)pyridinium chloride (BupyCl) were found to have a wider potential window, and they were liquid at room temperature over a wider range of compositions. In addition, they displayed no light sensitivity compared to melts derived from N-ethylpyridinium bromide.

In 1982, Wilkes *et al.*(13), introduced a new family of room-temperature molten salts that were prepared by combining aluminum chloride with a dialkylimidazolium chloride salt. Their choice of these salts was based on predictions resulting from Modified Neglect of Diatomic Overlap (MNDO) molecular orbital calculations. These MNDO calculations suggested that the dialkylimidazolium cations were extremely resistant to reduction. Of the dialkylimidazolium chlorides, 1-methyl-3-ethylimidazolium chloride (MeEtimCl) was found to result in melts with the best overall chemical, electrochemical, and physical properties. The AlCl_3 -MeEtimCl melt has become the system of choice because it is a liquid at room temperature over a wider range of composition than the AlCl_3 -BupyCl melt. This is apparently due to the lower symmetry of the MeEtim⁺ ion relative to the Bupy⁺ ion (4). The AlCl_3 -MeEtimCl melt also has a wider potential range than the AlCl_3 -BupyCl melt because

MeEtim⁺ is more difficult to reduce than Bupy⁺ (13). Room-temperature molten salts have gained wide acceptance as electrochemical solvents. This is in part due to the many unique properties of these unusual molten salts. For example, these room-temperature molten salts do not require a supporting electrolyte to make them conductive, and they exhibit other favorable properties like excellent chemical and thermal stability, low vapor pressure, low melting point, high electrical conductivity, and adjustable Lewis acidity. These molten salts have also proven to be excellent solvents for a wide range of organic, organometallic, and inorganic solutes. The structures of these room-temperature haloaluminate molten salt systems appear in Figure 1.1.

1.1.2 Acid-Base Properties of the AlCl₃-MeEtimCl Molten Salt

One of the many useful characteristics of chloroaluminate molten salts, such as AlCl₃-MeEtimCl, is that the Lewis acidity of the melt may be altered simply by changing the composition of the melt (Figure 1.2). The principal reaction governing the acidity is described by the following equation.



For the AlCl₃-MeEtimCl melt, the equilibrium constant for this reaction is approximately 10⁻¹⁷ at 40 °C (14). The Lewis acidity of AlCl₃-MeEtimCl melt is analogous to the Brønsted acidity of water:

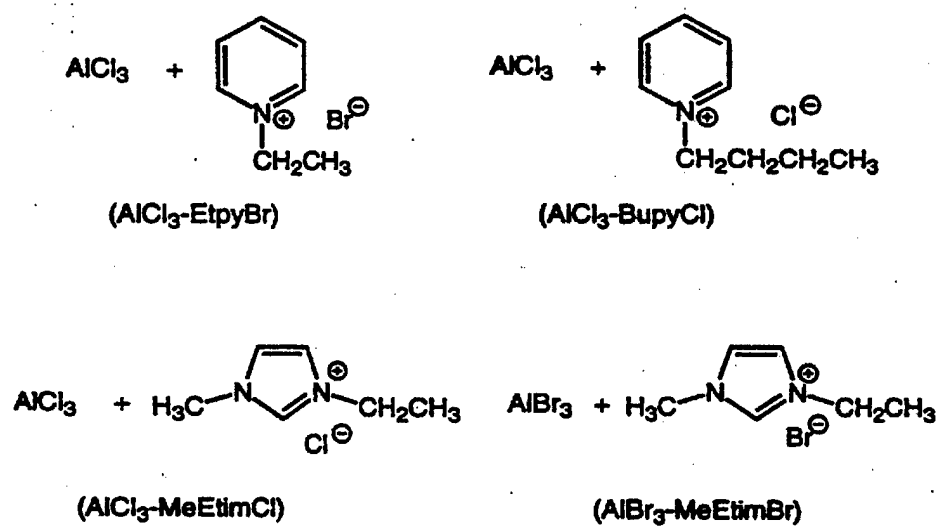


Figure 1.1. Structures of room-temperature haloaluminate molten salts (15).

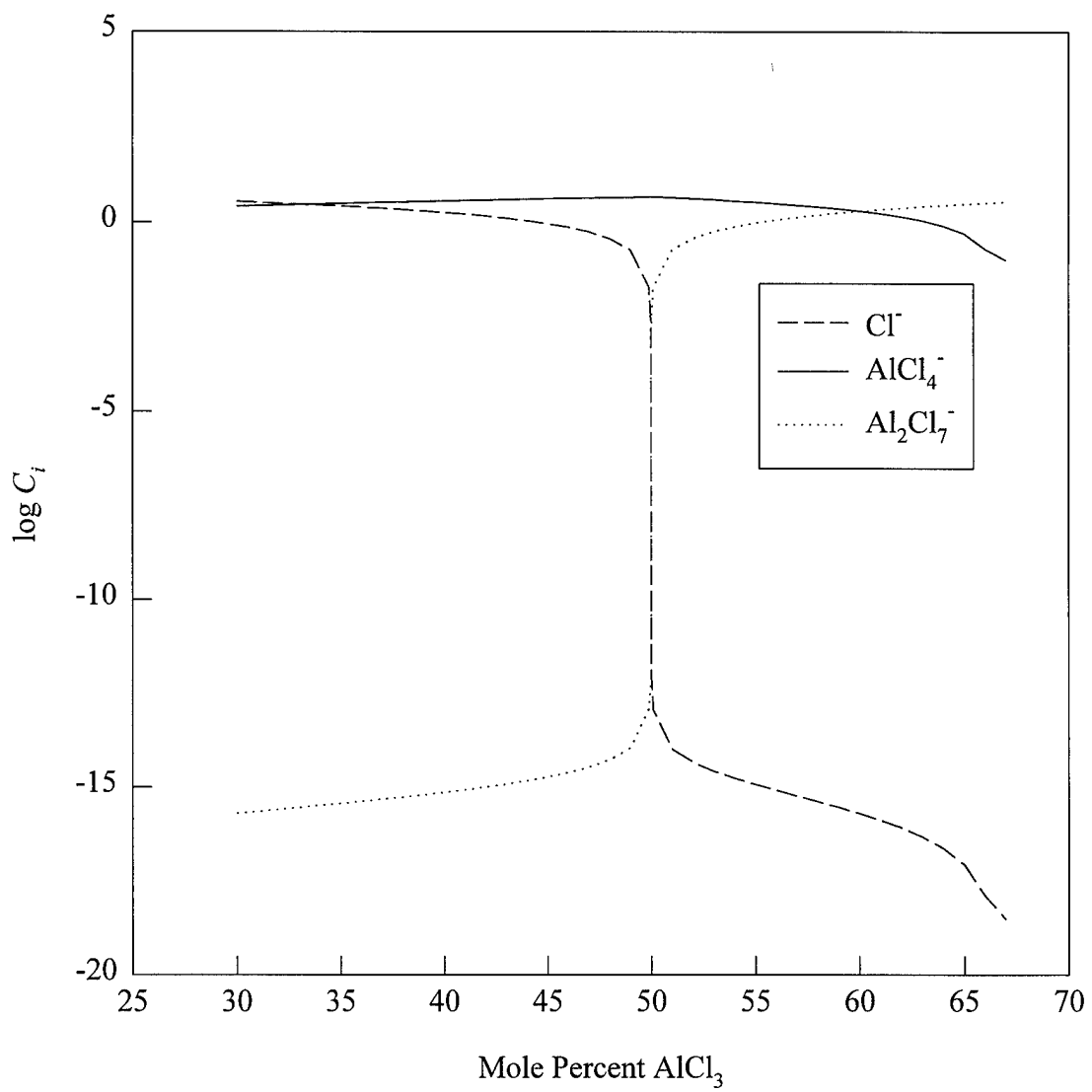


Figure 1.2 Concentration of the anionic species as a function of composition in the AlCl₃-MeEtimCl molten salt (15).



Melts having an aluminum chloride content of less than 50 mole percent (m/o) AlCl_3 are classified as basic because they contain chloride ions that are not covalently bound to aluminum. Melts prepared from equimolar amounts of AlCl_3 and MeEtimCl are designated as neutral because AlCl_4^- is the predominant anionic component of the melt. Melts prepared with a molar excess of AlCl_3 are classified as acidic due to the presence of the chloride acceptor, Al_2Cl_7^- . All of the research presented herein was carried out in acidic melts because the metals and alloys studied cannot be deposited from basic melts; chloride ions complex and stabilize most metal ions, making them difficult if not impossible to reduce ~~to~~ the corresponding metals.

1.1.3 Physical and Electrochemical Properties of AlCl_3 -MeEtimCl Molten Salts

The physical properties of the AlCl_3 -MeEtimCl molten salt vary considerably with the ratio of aluminum chloride to organic salt. The AlCl_3 -MeEtimCl molten salt system has a large potential window, wide thermal stability, and broad liquid range, making it a very practical solvent system for a variety of electrochemical applications. A phase diagram of the AlCl_3 -MeEtimCl system is shown in Figure 1.3; it can be seen that the AlCl_3 -MeEtimCl molten salt is liquid at room temperature in the interval between 30.0 and 68.0 m/o AlCl_3 . The range of potentials over which a solvent is electrochemically inert is called the potential window of the solvent, and a solvent is considered inert when its background current does not interfere with the electrochemical system being studied. The amount of background

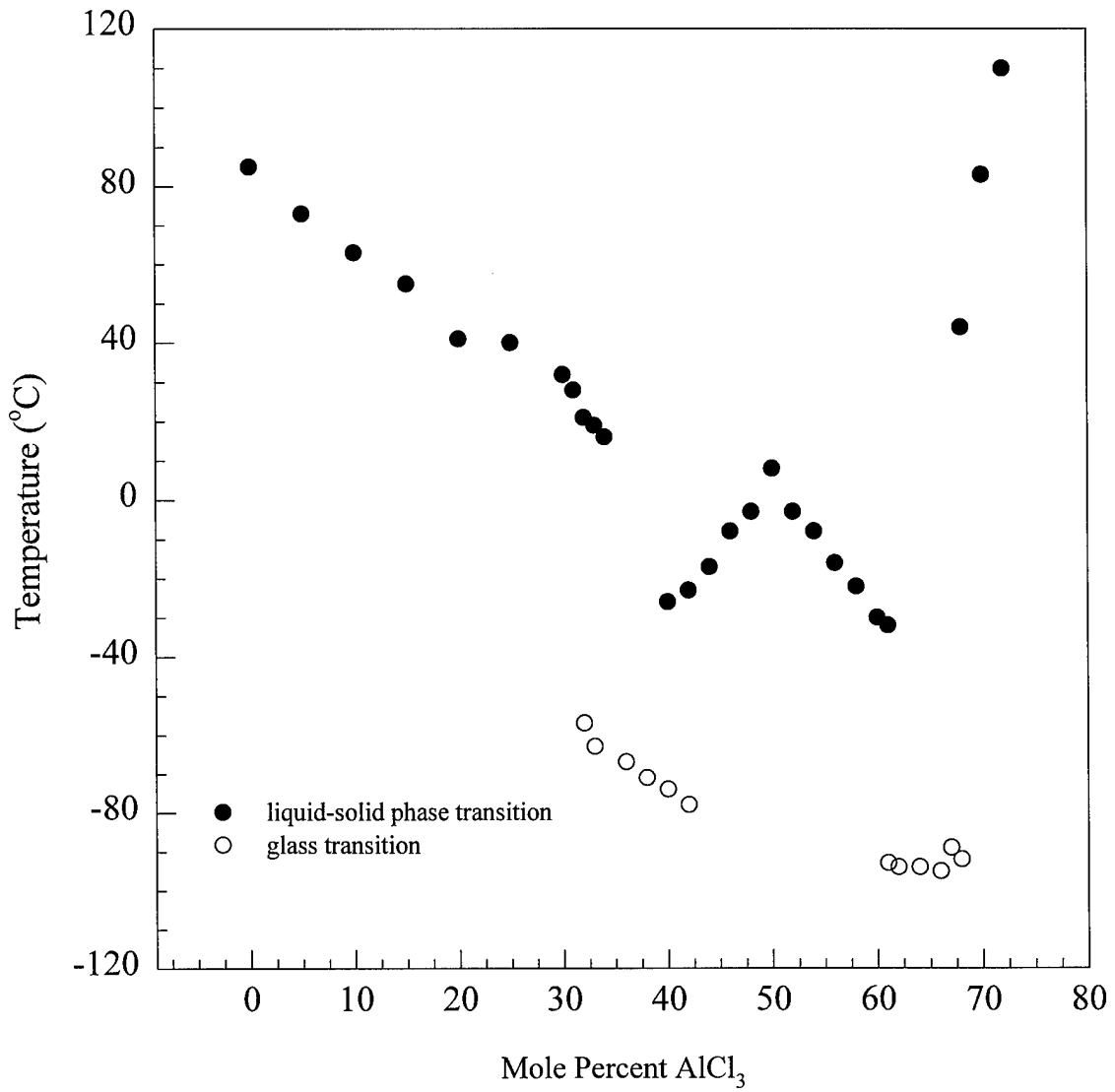
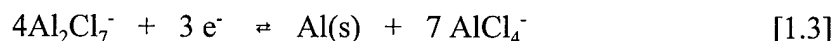
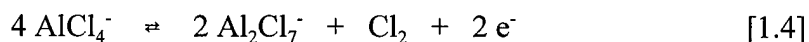


Figure 1.3 Phase diagram of the AlCl₃-MeEtimCl system (13).

current that can be tolerated is a matter of individual preference. Figure 1.4 shows the electrochemical potential window of the AlCl_3 -MeEtimCl molten salt (15). The acidic AlCl_3 -MeEtimCl melts are generally considered to have a potential window of approximately 2.2 V. The negative potential limit of acidic AlCl_3 -MeEtimCl melt (0 V) is reached when Al_2Cl_7^- is reduced, resulting in the electrodeposition of aluminum metal.



The positive potential limit (2.2 V) corresponds to the oxidation of AlCl_4^- to produce chlorine and Al_2Cl_7^- .



Acidic melts with ≥ 65 m/o AlCl_3 contain very little AlCl_4^- ; the positive potential window of these melts results from the oxidation of some other chloroaluminate species (e. g., Al_2Cl_7^- or $\text{Al}_3\text{Cl}_{10}^-$).

The electrode reaction at the positive limit of basic melt is the oxidation of chloride ion. The reaction at the negative limit in basic melt is the reduction of the MeEtim^+ ion. In melts containing equimolar amounts of AlCl_3 and MeEtimCl, *i.e.*, neutral melts, the electrochemical window encompasses the positive limit of the acidic melt and the negative limit of the basic melt (14).

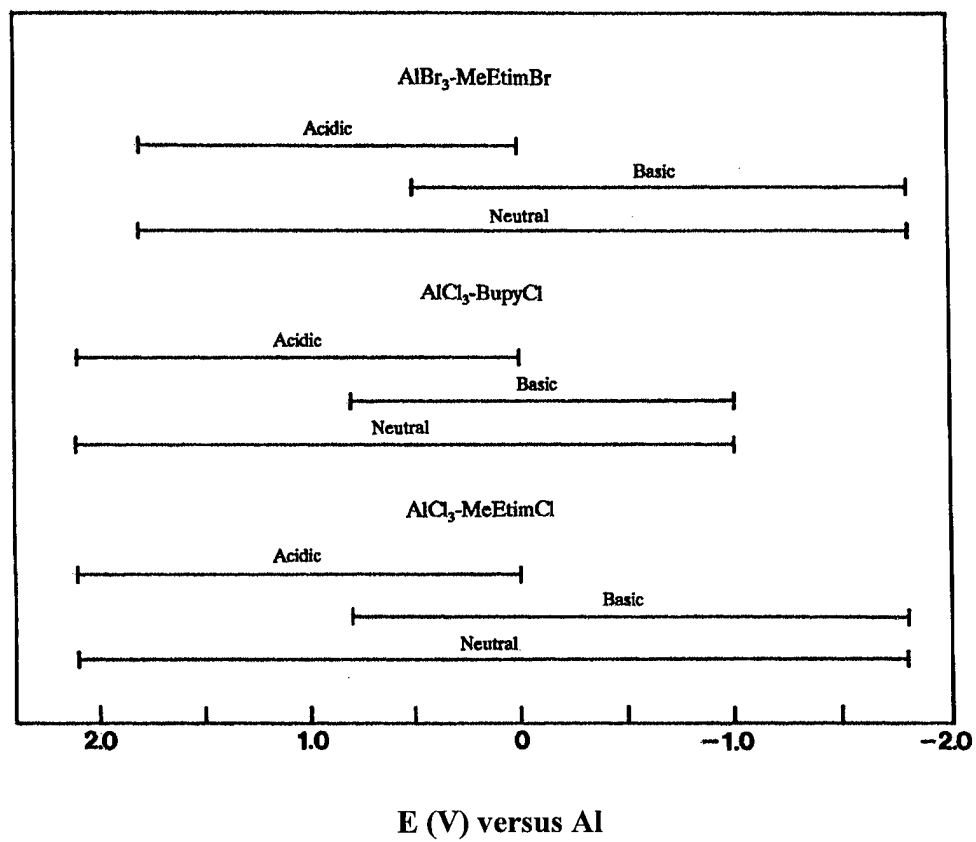


Figure 1.4 Electrochemical potential window of room-temperature molten salts (69).

1.1.4 Electrodeposition of Metals and Alloys from both High Temperature and Room-Temperature Chloroaluminate Melts

Electrodeposition can be a convenient method for creating thin films of metals and alloys. The control available during electrodeposition makes it a useful technique for the electroplating of structures as simple as truck bumpers and as complex as printed circuit boards and nanostructured devices (16, 17). In many cases, the composition of the deposit including alloy formation can be strictly controlled during the electroplating process (18, 19, 20). Most commonly, electrodeposition is carried out in aqueous media. However, as discussed previously, the use of aqueous media is not practical for the electrodeposition of aluminum and its alloys. Also mentioned earlier, room-temperature haloaluminate molten salts were introduced by Hurley and Wier in 1951 for the express purpose of plating aluminum (7-11). The deposition of aluminum from room-temperature molten salts has remained a point of interest, and in 1979 Osteryoung (21) electrodeposited aluminum from acidic AlCl_3 -BupyCl.

The studies that have been carried out on the electrodeposition of pure metals from acidic room-temperature melts include: aluminum (22), cobalt (23, 24), lead (25), mercury (26), nickel (27), silver (28), and tin (29). Lead, mercury, and silver were all studied in 66.7-33.3 m/o AlCl_3 -MeEtimCl (26, 28, 30). Electrochemical and spectral investigations of Co(II) (24) and Ni(II) (31, 32) were carried out in acidic AlCl_3 -BupyCl. Iron, copper, and nickel have been studied in buffered, acidic AlCl_3 -MeEtimCl (33). Zinc(II) chloride was perceived insoluble (34) in acidic AlCl_3 -MeEtimCl. Yet, by using controlled potential electrolysis, Zn(II) was easily introduced into the melt, and the electrodeposition of Zn was studied in this

melt (35). Studies of metal electrodeposition from basic melts were restricted to gold (36) palladium, tin, and mercury (37, 38). The limited work done in basic melt reflects the fact that most metal ions are complexed by chloride ion in this melt, making them very resistant to reduction.

The studies listed above cover the time period from 1979 to the present, and it should be remembered that alloys were not generally the focus of this early work. Thus, during some of this previous work, it was not obvious that many of the deposits were not pure metals, but actually aluminum-containing alloys. For example, it is now known that the electrodeposition of chromium (17, 39), cobalt (18), and nickel (19, 20, 40) from acidic room-temperature chloroaluminate melts involves the co-deposition of aluminum. However, comprehensive investigations of the fundamental aspects of the electrodeposition of these transition metal-aluminum alloys are lacking. Ni-Al alloy was electrodeposited using dc and pulsed current electrolysis from room-temperature acidic AlCl_3 -BupyCl molten salt containing Ni(II) (42). The co-deposition of nickel and aluminum at potentials positive of the bulk deposition of aluminum has recently been demonstrated in acidic AlCl_3 -MeEtimCl (35). Recent work by Carlin *et al.* (41) was concerned with the electrodeposition of Co-Al alloys from acidic AlCl_3 -MeEtimCl containing Co(II). Cu-Al alloys were deposited from solutions of Cu(I) in AlCl_3 -MeEtimCl (36, 42). Cr-Al alloys have been electrodeposited from acidic AlCl_3 -MeEtimCl (43) and from acidic AlCl_3 -BupyCl (44). The chromium content of the AlCl_3 -BupyCl electrodeposits reached a maximum of 94 a/o and were found to be independent of deposition parameters such as concentration and applied potential.

The electrodeposition of transition metals and their aluminum alloys has also been studied from high-temperature chloroaluminates such as $\text{AlCl}_3\text{-NaCl}$ and from conventional organic solvent-electrolyte combinations such as alkylbenzene-hydrogen bromide. The $\text{AlCl}_3\text{-NaCl}$ melt has an adjustable acidity similar to $\text{AlCl}_3\text{-MeEtimCl}$, but its temperature range is ca. 150 to 250 °C. However, the melt has proven practical for routine use. The main drawbacks for the $\text{AlCl}_3\text{-NaCl}$ system are the significant vapor pressure of AlCl_3 and the high operating temperatures required to work with this melt. The disposal of waste solvent, the low conductivity, and the high vapor pressure of organic solvents such as the alkylbenzenes makes this an unattractive medium for electrodeposition, and so it will not be discussed further here.

The electrodeposition of titanium from the 66.7-33.3 m/o $\text{AlCl}_3\text{-NaCl}$ molten salt at 150 °C containing Ti(IV) (45) revealed a metastable Al-Ti alloy containing up to 28 atomic percent (a/o) Ti. Mn-Al alloys containing between 5 and 22 a/o Mn (46,47) were obtained from solutions of Mn(II) in this same melt. The addition of manganese to the aluminum had a remarkable effect in that the single phase Mn-Al alloy displayed a 400 mV increase in pitting potential relative to pure aluminum. Cr-Al alloys have been electrodeposited from 66.7-33.3 m/o $\text{AlCl}_3\text{-NaCl}$ at 175 °C (48). The chromium content of these deposits reached a maximum of 94 a/o and were found to be independent of deposition parameters such as concentration and applied potential. Iron, copper, and nickel have also been studied in acidic $\text{AlCl}_3\text{-NaCl}$ at 220 °C (49). The electrodeposition of Ni-Al alloys has been investigated in the 66.7-33.3 m/o $\text{AlCl}_3\text{-NaCl}$ melt at 150 °C (50). The nickel composition of these electrodeposits was shown to be a function of potential, but not the Ni(II) concentration in

the melt. The co-deposition of aluminum was described as an underpotential process occurring simultaneously with nickel deposition.

1.1.5 Fundamentals of the Electrodeposition of Metals

The process of electrodeposition, more commonly known as electroplating, is a simple electrolysis experiment in which an oxidized species is reduced to a solid on the surface of a cathode. This surface can be as small as a sub-millimeter wire and as large as a truck bumper. The process of electrodeposition can be broken down into three basic steps: (i) formation of stable metal (M) adatoms on a substrate (S), (ii) nucleation of a new metal phase, and (iii) growth of crystals in the metallic bulk phase. In terms of the potentials required to initiate the electrodeposition process, there are two limiting pathways defined as underpotential deposition (UPD) and overpotential deposition (OPD) (20). Which of these limiting cases predominates is determined by the relative magnitudes of the interaction energy between the metal adatoms and the substrate, Ψ_{M-S} , and between individual metal adatoms, Ψ_{M-M} .

In UPD, deposits form at potentials more positive than the equilibrium potential, E_{eq} , of the M^{n+}/M couple. Simply put, the interaction between the metal and the substrate is stronger than the attraction between metal adatoms. This causes the metal to deposit positive of its equilibrium potential. The underpotential is defined as

$$\Delta E = E - E_{eq} > 0 \quad [1.5]$$

There are two UPD models: (i) the “Frank-Van der Merwe” mechanism characterized by two-dimensional growth of monolayers (Figure 1.5b); and (ii) the “Stranski-Krastanov” mechanism, which involves two-dimensional monolayer growth followed by three-dimensional crystal growth (Figure 1.5c). Experimentally, UPD is usually seen on metal substrates more noble than the depositing metal.

If Ψ_{M-S} is significantly less than Ψ_{M-M} , then OPD may occur. The overpotential is defined as

$$\eta = E - E_{eq} < 0 \quad [1.6]$$

where E represents the potential at which nucleation is actually observed. OPD is embodied by the “Volmer-Weber” mechanism of three-dimensional nucleation and crystal growth and is depicted in Figure 1.5a (20). The nucleation of a new phase begins by the potential-induced supersaturation of the active sites, most likely surface defects, on the substrate surface. This is followed by the formation of stable clusters of adatoms. The number of adatoms required to form a stable metal cluster, known as the critical number, n_c , is dependent on both the metal and substrate. The rate of formation of nuclei is dependent on the magnitude of the overpotential.

The current $i(t)$ associated with the nucleation process is considered to be the convolution of the number density of nuclei as a function of time, $N(t)$, and the number density of growing centers as a function of time, $g(t)$, for an isolated nucleus (51, 52)

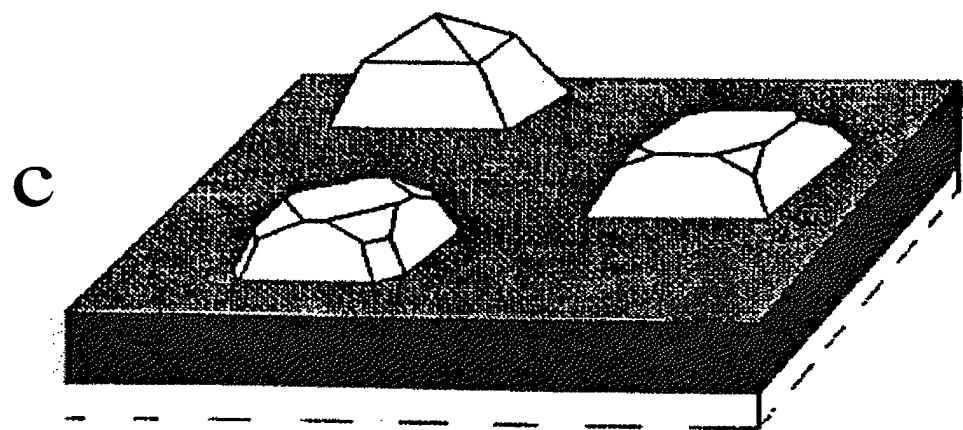
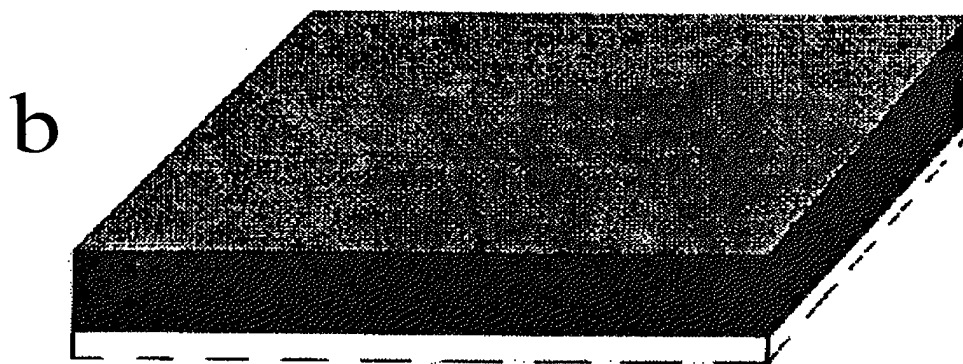
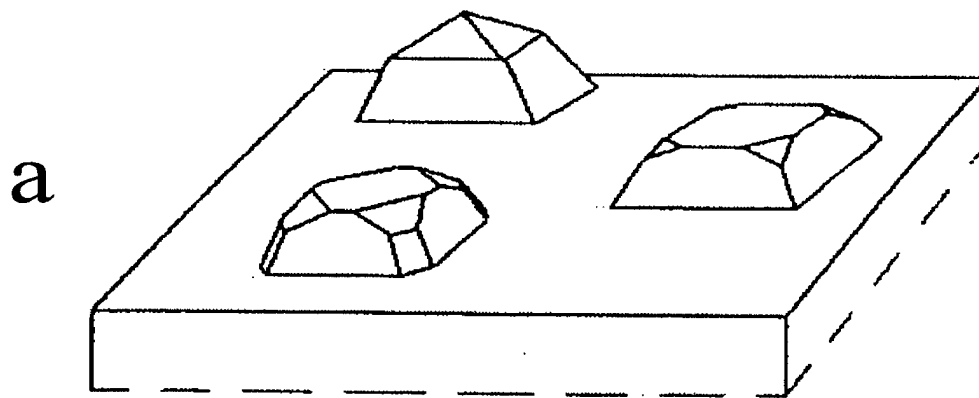


Figure 1.5. Crystal growth mechanisms for overpotential and underpotential deposition. (a, top) Volmer-Weber. (b, middle) Frank-Van der Merwe. (c, bottom) Stranski-Krastanov.

$$i(t) = \int_0^t g(u) (\partial N(t)/\partial t)_{t=t-u} du \quad [1.7]$$

$N(t)$ is usually assumed to follow a Poissonian type law. In other words, all active sites have the same probability for the formation of nuclei. If the total number of possible active sites under a particular experimental condition is defined as N_0 (cm^{-2}), then the rate of appearance of stable growth centers can be assumed to follow first-order kinetics. In this event, the number density of nuclei is given by the following equation (53).

$$N(t) = N_0 \{ 1 - \exp(-A_1 t) \} \quad [1.8]$$

Where A_1 (s^{-1}) is the nucleation rate constant per active site. In the limiting case where $A_1 t \gg 1$, Equation 1.8 becomes

$$N(t) = N_0 \quad [1.9]$$

On the other hand, for small values of $A_1 t$ the number density of nuclei is given by

$$N(t) = N_0 A_1 t \quad [1.10]$$

The limiting cases described by Equations 1.9 and 1.10 are referred to as instantaneous and progressive nucleation, respectively (53,54). These models have been used extensively to describe nucleation on foreign substrates. In instantaneous nucleation, all of the nuclei form

simultaneously and grow at the same rate. In progressive nucleation, nuclei form sequentially and at different rates (55). These models are differentiated by kinetic or diffusion control, by the shape of the nuclei, and by whether the diffusion of metal ions to the growing nuclei is a two-dimensional (planar) or three-dimensional (hemispherical) process (53). The diffusion-limited three-dimensional instantaneous and progressive models have been found to be applicable to most metal deposition reactions in the AlCl_3 -MeEtimCl molten salt system (56). If it is assumed that the nuclei that form are hemispherical or cylindrical in shape and that the deposition is under either pure kinetic or diffusion control, then by using Faraday's law and Fick's equations with the appropriate boundary conditions, Equation 1.7 reduces to (51-53)

$$i(t) = \alpha t^n \quad [1.11]$$

where α is a dimensionless parameter containing information about the nucleation rate and n takes values between 1 and 3, depending on the electrodeposition mechanism. The values of α and n corresponding to several different mechanisms are collected in Table 1.1.

1.1.6 Three-dimensional Nucleation

The growth of stable nuclei can be described by semi-infinite radial diffusion of the depositing species to the growing nucleus (57). It is infelicitous that the kinetics of metal nucleation cannot be linked to the growth of a single nucleus multiplied by the total number of nuclei. As a nucleus begins to form, a diffusion field forms about its center of activity. This field may be a two- or three-dimensional field and can affect the formation of other

Table 1.1 Mathematical models describing kinetic and diffusion controlled three dimensional nucleation.

Kinetically controlled growth		Progressive nucleation $\alpha =$		Instantaneous nucleation $\alpha =$	
Shape of nuclei Cylinder	$n = 1$	$\frac{2zF\pi MhN_o k^2}{\rho}$	$n = 2$	$\frac{zF\pi MhA_t N_o k^2}{\rho}$	
Shape of nuclei Hemisphere	$n = 2$	$\frac{2zF\pi M^2 N_o k^3}{\rho^2}$	$n = 3$	$\frac{2zF\pi M^2 A_t N_o k^3}{3\rho^2}$	
Diffusion limited growth		Progressive nucleation $\alpha =$		Instantaneous nucleation $\alpha =$	
Hemisphere and planar diffusion	$n = 1/2$	$\frac{8zFM^2 C^3 D^{3/2} N_o}{\rho^2 \pi^{1/2}}$	$n = 3/2$	$\frac{16zFM^2 C^3 D^{3/2} A_t N_o}{3\rho^2 \pi^{1/2}}$	
Hemisphere and spherical diffusion	$n = 1/2$	$\frac{zF\pi M^{1/2} (2CD)^{3/2} N_o}{\rho^{1/2}}$	$n = 3/2$	$\frac{4zF\pi M^{1/2} (CD)^{3/2} A_t N_o}{3\rho^{1/2}}$	

nuclei in its vicinity. Therefore, the current for the actual growth of n number of nuclei will be less than the combined currents for growth of n individual nuclei (58). A second consequence of radial growth is the depletion of the deposition species in the direct vicinity of the forming nuclei, resulting in inhibition of the formation of new nuclei. This “exclusion zone” reduces the probability of finding another nucleus in close proximity and therefore reduces to a finite number the nuclei in a given area (59, 60).

Nucleation processes are typically investigated by using potential-step chronoamperometry. A detailed discussion of this technique is found in Chapter Two. A typical nucleation transient for such a potential-step experiment is seen in Figure 1.6. When the potential pulse is initiated, a current appears due to the charging of the electrode-solution double layer. After this current decays, another rise in current is seen due to the formation and growth of metal nuclei. The current reaches a maximum, i_m , when the diffusion zones of the individual nuclei begin to overlap. The time corresponding to the current maximum is designated as t_m . As the current falls, it begins to approach the value expected for linear diffusion to a planar surface (61). Often, the nucleation mechanism can be determined by examining the rising current in the chronoamperometric transient. To do this, the rising current is plotted versus t according to Equation 1.11. The value of n that yields a linear plot is then compared to those in Table 1.1 in order to deduce the mechanism.

A better method to determine the applicability of nucleation models is to compare current-time transients derived from potential-step experiments to the theoretical transients for different mechanisms. The dimensionless current for three-dimensional instantaneous and progressive nucleation is described by Equations 1.12 and 1.13, respectively.

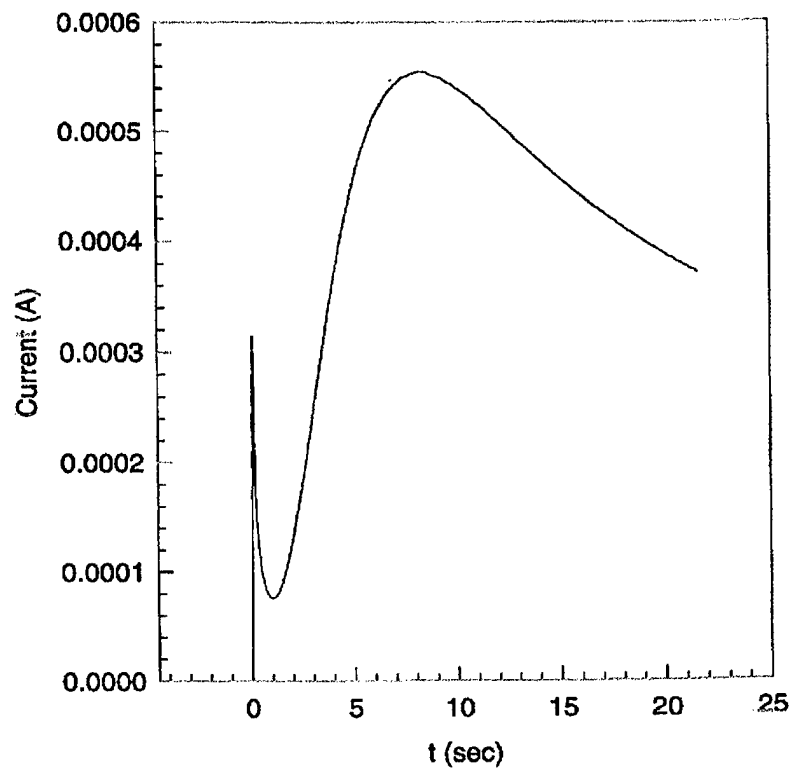


Figure 1.6 Current-time transient showing the effects of nucleation.

$$i(t)^2/i_m^2 = 1.9542/(t/t_m) \{1-\exp [-1.2564(t/t_m)]\}^2 \quad [1.12]$$

$$i(t)^2/i_m^2 = 1.2254/(t/t_m) \{1-\exp [-2.3367(t/t_m)^2]\}^2 \quad [1.13]$$

Nucleation that falls between these two extreme cases is considered to be progressive nucleation, but at a finite number of active sites. The dimensionless current-time transients for this type of nucleation are given by the following (62):

$$(i(t)/i_m)^2 = (t/t_m)\{1-\exp[-x(t/t_m)+\alpha(1-\exp(-x/\alpha(t/t_m)))]\}^2/\{1-\exp[-x+\alpha(1-\exp(-x/\alpha))]\}^2 \quad [1.14]$$

Equation 1.14 contains the adjustable parameters α and x that provide information about A_t and N_0 . For the limiting cases of instantaneous and progressive nucleation, x approaches 1.2564 and 2.3367, while α approaches zero and infinity respectively. In the limiting case of progressive nucleation, the ratio $A_t/N_0 \rightarrow 0$ (63). In this case, A_t and N_0 can not be determined separately, and the nucleation kinetics must be analyzed in terms of the steady-state nucleation rate, $A_t N_0$ ($s^{-1} \text{ cm}^{-2}$). A convenient relationship for calculating $A_t N_0$, which uses information from both i_m and t_m , is the following (64):

$$A_t N_0 = 0.3864(nFC_{\text{sb(III)}}^* A)^2/(i_m^2 t_m^3 k') \quad [1.15]$$

$$k' = 4/3[(8\pi C_{\text{sb(III)}}^* M)/\rho]^{1/2} \quad [1.16]$$

where A represents the electrode area and t_m' is a delay time corrected form of t_m explained below, and M and ρ are the molecular weight and density of the metal deposit, respectively. The saturation nuclear number density, N_s , is the nuclear number density observed at long times after the development of new nuclei and the arrest of their growth by the formation of nucleation exclusion zones around the growing nuclei. N_s is calculated from $A_t N_0$ according to Equation 1.17 (65).

$$N_s = (A_t N_0 / 2k'D_{sb(III)})^{1/2} \quad [1.17]$$

According to the atomistic theory of nucleation, the slope of a plot of $\log(A_t)$ versus η gives information about the critical number of atoms required for the formation of stable clusters, n_c (66). n_c is related to this slope by Equation 1.18, where k is the Boltzmann constant, e_0 is the elementary charge, and α is the cathodic transfer coefficient (67).

$$n_c \approx (2.303kT/ne_0)[d\log(A_t)/d\eta] - \alpha \quad [1.18]$$

An optimal method for the elucidation of potential-time transient data is to compare the experimental dimensionless curve $(i(t)/i_m)$ versus (t/t_m) with that predicted by theory. A non-linear algorithm is used to determine the values of α and x that provide the best fit. A correction factor for the delay time preceding nucleation, t_0 , is also necessary. This correction factor accounts for the time lapse between the start of the transient and the beginning of the nucleation process. The term, t_0 , is estimated from the x-intercepts of graphs of $(i(t)/i_m)^2$ or

$(i(t)/i_m)^{2/3}$ versus t for instantaneous or progressive nucleation, respectively. Alternatively, t_0 can be a fitted parameter along with α and x in Equation 1.14. In the work described herein, the best values of α , x , and t_0 were found by using a Marquardt-Levenberg non-linear algorithm based curve fitting program. The correction factor, t_0 , is then subtracted from all of the t values, including t_m . The result is t' , and t_m' where $t' = t - t_0$ and $t_m' = t_m - t_0$. Once α , x , and t_0 have been established, it is possible to determine N_0 and A_t from the following relationships (68):

$$N_0 = (x / \pi D_0 (8 \pi C_0 M / \rho))^{1/2} \quad [1.19]$$

$$A_t = (N_0 \pi D_0 (8 \pi C_0 M / \rho))^{1/2} / \alpha \quad [1.20]$$

The information obtained about the nucleation mechanisms gives information about the initial phases of nucleation and crystal growth during the electrodeposition of metals and their alloys.

1.2 Objectives

The objectives of this research project were to exploit the aprotic nature and other properties of the AlCl_3 -MeEtimCl molten salt for the electrodeposition of transition metal and transition metal-aluminum alloys. Specifically, the objectives were: *i*) to probe the electrochemistry of antimony, cobalt, and iron; *ii*) to determine if the electrodeposition of Sb-Al, Co-Al, and Fe-Al alloys from acidic AlCl_3 -MeEtimCl molten salts is possible; *iii*) to

determine the effects of applied potential, current density, and the AlCl_3 -MeEtimCl ratio on the composition and morphology of the alloy deposits; *iv*) to elucidate the electrodeposition mechanism(s) leading to the formation of these alloys; *v*) to demonstrate that metal-aluminum alloy deposition can occur by co-deposition of aluminum at potentials positive of the bulk deposition of aluminum; *vi*) to obtain thermodynamic data about the M^{n+}/M couples and transport data about the M^{n+} species.

CHAPTER II EXPERIMENTAL

2.1 Chemicals.

Aluminum chloride, AlCl_3 (Fluka, puriss), was purified by sublimation three times in a special apparatus inside a dry nitrogen filled glove box (70). The resulting purified AlCl_3 was crushed and stored in the glove box in an air-tight container.

1-Methyl-3-ethylimidazolium chloride was prepared according to the method described by Wilkes *et al.* (13) All steps in this procedure were carried out under vacuum or dry nitrogen on a Schlenk line. 1-Methylimidazole (Aldrich, 99%) was purified by vacuum distillation from NaH then combined with an excess of ethyl chloride in a Pyrex glass pressure vessel. Once the addition was complete, the reaction flask was sealed and placed in a 60 °C water bath for approximately seven days. Any unreacted ethyl chloride was removed under vacuum once the reaction was complete. The crude salt was purified by carrying out three successive recrystallizations from solutions of acetonitrile and ethyl acetate. The pure MeEtimCl was melted at ca. 80 °C and evacuated to remove any remaining solvent. It was then poured into an aluminum tray to solidify. The solid was then broken into chunks and stored in the glove box in an air-tight container.

The preparation of the AlCl_3 -MeEtimCl molten salt was accomplished by combining the proper weights of the two components in a sealed jar. Due to the highly exothermic nature of the reaction between MeEtimCl and AlCl_3 , the AlCl_3 was added slowly to the

MeEtimCl with vigorous stirring. The resultant melt was a colorless or nearly colorless liquid, depending on the purity of the reactants and the acidity of the melt.

The melt was purified by electrolysis between two 3 mm diameter aluminum rods (*Æsar*, 99.995%) at a current density of ca. 0.1 mA cm⁻². The melt was then filtered through a medium porosity sintered glass filter and transferred to a high vacuum round bottom flask. The filtered solution was evacuated with a diffusion pump to < 5 x 10⁻⁵ torr for 24 hours in order to remove any protons as HCl. After this treatment was completed, the melt was stored over aluminum wire in a screw top Erlenmeyer flask in the glove box.

2.2 Equipment

The preparation of the AlCl₃-MeEtimCl molten salt and all experiments were carried out in a nitrogen-filled Kewauee Scientific Equipment Corporation (KSE) glove box. The glove box was equipped with a KSE Model 2C2500/30 ft³ min⁻¹ inert gas purifier. The atmospheric quality was continuously monitored with a 25 W light bulb whose filament was exposed to the glove box atmosphere (71). The glove box columns contain both molecular sieves and a BASF proprietary copper catalyst for the removal of water and oxygen, respectively. The columns were regenerated as needed by passing a nitrogen-hydrogen mixture through the heated purification columns.

All of the electrochemical experiments were carried out using an EG & G Princeton Applied Research Corporation (PARC) Models 173 or 273 potentiostat equipped with a Model 179 digital coulometer plug-in-module and a PARC Model 175 universal programmer. The Model 273 potentiostat was interfaced to a 386x computer. A Pine RDE3 bipotentiostat

was used for RRDE voltammetry. Analog data were recorded with a Linseis Model 1600 X-Y/Y-t recorder, this recorder was coupled to a Hewlett Packard Model 3393A digital integrator. Electronic resistance compensation was utilized during all electrochemical experiments. Controlled electrode rotation was carried out with a Pine Instruments Model AFMSR rotator.

2.2.1 Electrochemical Cells and Electrodes

Several different metals served as the working electrode during this project, and the preparation of each is listed below. Aluminum wire (Alfa *Aesar* Puratronic, 1.0 mm diameter, 99.999 %) was used in the construction of reference and counter electrodes and was added to storage flasks containing acidic melt. The surface of this wire was cleaned by scraping it with a stainless steel spatula inside the oxygen-free, nitrogen-filled glove box to remove as much of the oxide film on the aluminum surface as possible.

Cobalt wire (Alfa *Aesar* Puratronic, 1.0 mm diameter, 99.997 %) was sanded with emery paper, rinsed with acetone, and dried under vacuum prior to use. Cobalt(II) was introduced into the melt through the controlled-potential anodization of this wire at an applied potential of 1.4 V.

Iron wire (Johnson Matthey Electronics, 2.0 mm diameter, 99+ %) was sanded with emery paper, rinsed with acetone, and dried under vacuum prior to use. Iron(II) was introduced into the melt through controlled-potential anodization of an iron wire electrode at an applied potential of 1.2 V.

Antimony rod (Alfa *Aesar* Puratronic, 12.5 mm diameter, 99.9 %) was cut to a size that fit the electrochemical cell, dipped into concentrated hydrochloric acid, rinsed with acetone, and dried under vacuum prior to use. Antimony was introduced into the melt through the controlled-potential anodization of an antimony rod at an applied potential of 1.3 V.

Several different working electrodes were used during this research project. Teflon-sheathed platinum (0.126 cm² and 0.196 cm²), tungsten (0.196 cm²), gold (0.126 cm²), and glassy carbon (0.196 cm²) rotating disk electrodes and a platinum rotating ring-disk electrode ($r_1 = 2.29$, $r_2 = 2.46$, and $r_3 = 2.69$ mm) were obtained from Pine Instrument Company. All working electrodes were polished to a mirror finish prior to each use with 0.3 μm and 0.05 μm alumina slurries on a Buhler Metaserv grinder/polisher. The electrodes were washed with deionized water and dried under vacuum in the antechamber of the glove box prior to use.

The primary electrochemical cell used for this research was a Pyrex glass cup with a Teflon lid; both were constructed in this laboratory. The lid accommodated four holes for the insertion of electrodes and allowed the insertion of a small Pyrex-sheathed thermocouple. The reference electrode was an aluminum wire immersed in 60.0-40.0 m/o melt isolated from the analyte solution by a fine porosity glass frit. All potentials given in this dissertation are reported against the Al(III)/Al couple in the 60.0-40.0 m/o AlCl₃-MeEtimCl melt. Two types of counter electrodes were used, depending on the type of experiment to be undertaken. The first was identical to the reference electrode; the second was one of the wire electrodes described above.

2.2.2 Analysis of Bulk deposits

Compositional analyses of the electrodeposits were carried out with scanning electron microscopy (SEM) and energy dispersive x-ray spectroscopy (EDS). Samples were electrodeposited on 1 mm diameter copper or nickel wire substrates. SEM and EDS analyses were carried out on either the as-deposited surface or the powder resulting from a non-adherent deposit. For quantitative analysis, the EDS results were referenced to pure metal (aluminum, cobalt, iron, and antimony) standards. SEM was also used to investigate the as-deposited surface morphology of the electrodeposits. Bulk deposits were also analyzed by atomic absorption spectroscopy (AAS) using a Perkin-Elmer Model 2380 Atomic Absorption Spectrophotometer.

2.3 Electrochemical Techniques

The electrochemical techniques employed in this study included controlled-potential electrolysis, chronoamperometry, cyclic voltammetry, rotating-disk and ring-disk electrode voltammetry, and anodic linear sweep voltammetry (ALSV). In controlled-potential electrolysis experiments, the working electrode is held at a fixed potential either positive or negative of the equilibrium potential, E_{eq} , to effect the electrodisolution or electrodeposition of the metal(s) in or from solution, respectively. For electrodisolution, the metal is the working electrode and is anodized into solution to generate a melt solvated reducible metal ion. The valence of the cation, n , can be determined using the following relationship;

$$n = Q_{exp} M / F \Delta w \quad [2.1]$$

where Q_{exp} is the total charge passed during the electrolysis and Δw is the weight lost by the working electrode. It is possible to prepare solutions of precisely known concentrations using this technique.

Bulk electrodeposition is the converse of bulk electrodisolution. In bulk electrodeposition, the potential is held negative of E_{eq} and depending on the potential either the metal of interest or a metal-aluminum alloy can be reduced onto the working electrode. The substrate on which the metal is deposited was most often a copper wire. However, gold coated glass slides, nickel wire, and platinum flags ca. 0.1 mm thick and 5 mm wide cut from a platinum sheet were also used. Chronoamperometry, one of the simplest of the electrochemical techniques, utilizes a stationary working electrode in an unstirred solution held at an initial potential, E_1 , where no electrochemical reactions occur. The potential of the working electrode is then stepped to a second potential, E_2 , and the resulting current-time transient is recorded. In a chronoamperometric experiment involving a diffusion-controlled reaction, once the potential step is initiated and the Faradaic process begins, the absolute value of the current increases sharply due to an instantaneous reduction or oxidation of the electroactive species in the vicinity of the electrode surface. The current will decay with $t^{-1/2}$ as the diffusion layer around the electrode grows outward from the electrode surface. The Cottrell equation gives the relationship between the current and the elapsed time (72):

$$i(t) = nFAD_0^{1/2}C_0^* \pi^{-1/2} t^{-1/2} \quad [2.2]$$

where n , F , and A have their usual meaning and D_0 and C_0^* are the diffusion coefficient and the bulk concentration of the solute undergoing oxidation or reduction, respectively. Because much of this research involves the comparison of results from electrodes with different areas, the units of current density (j) are often used in place of the current (i). The current density is obtained by dividing the current by the area of the electrode.

Chronoamperometric data were taken at different values of E_2 and used to construct a sampled-current voltammogram, *i.e.*, a plot of $i(t)$ versus E_2 for a fixed t . As is seen for other forms of polarography, the current eventually reaches a maximum value called the limiting current, i_l , as a result of diffusion-control. The diffusion coefficient of the analyte ions can be determined from i_l and Equation 2.1. This technique also gives information about details of the electrode process. For example, if the electrode process is diffusion controlled, then the Cottrell equation can be applied and a plot of $t^{-1/2}$ should be linear and pass through the origin. The potential-step technique is also useful for the elucidation of nucleation mechanisms as discussed in Chapter One.

In linear-sweep voltammetry, the potential of the working electrode is changed linearly between selected potentials E_1 and E_2 while the electrode sits at rest in an unstirred solution. The rate of potential change is called the scan rate, v ($V s^{-1}$). As the potential is changed, the current response is recorded with the sweep being halted when the final potential, E_2 , is reached. The current response is due to the reduction or oxidation of the electroactive species in solution.

Cyclic voltammetry is simply an extension of linear-sweep voltammetry. In cyclic voltammetry, the voltage scan of the working electrode in the unstirred solution is the same

as that of linear sweep voltammetry, except that at the end of the forward sweep the scan is reversed at some switching potential, E_λ , at which point the potential is scanned back to the initial potential. Often, the range between E_1 and E_λ is chosen to span the entire electrochemical window of the solution to ensure that all possible electrochemical reactions are detected. The current observed in cyclic voltammetry is due to the oxidation or reduction of the electrochemical species in solution at the electrode surface. This current is proportional to the concentration gradient of the electrochemical species, $(\partial C/\partial x)$, where ∂C represents the concentration difference between the bulk solution and the electrode surface and ∂x represents the diffusion layer thickness. As the potential is scanned toward the switching potential E_λ , the function $(\partial C/\partial x)_{x=0}$, where $\partial C = C_o^* - C_o(E)$, will increase because ∂C increases faster than ∂x increases; consequently, the current will increase. After the peak current is reached, the current will decrease because $(\partial C/\partial x)_{x=0}$ decreases as ∂x increases, ∂C having reached its maximum possible value, C_o^* . The peak current is described by the Randels-Sevcik equation.(72)

$$i_p = 2.69 \times 10^5 n^{3/2} A D_o^{1/2} C_o^* v^{1/2} \quad \text{at } 25 \text{ }^\circ\text{C} \quad [2.3]$$

Figure 2.1a illustrates the typical shape of a cyclic voltammogram for a freely diffusing reversible electrode couple, $\text{Ox} + n\text{e}^- \rightleftharpoons \text{Red}$. This voltammogram has a number of typical features: a peak reduction current, i_p^c , located at the peak potential, E_p^c , and on the reverse scan, a peak cathodic current, i_p^a , located at the anodic peak potential, E_p^a . The shapes of the cyclic voltammograms for the deposition and stripping of metals (see Chapters 3-5) are rather

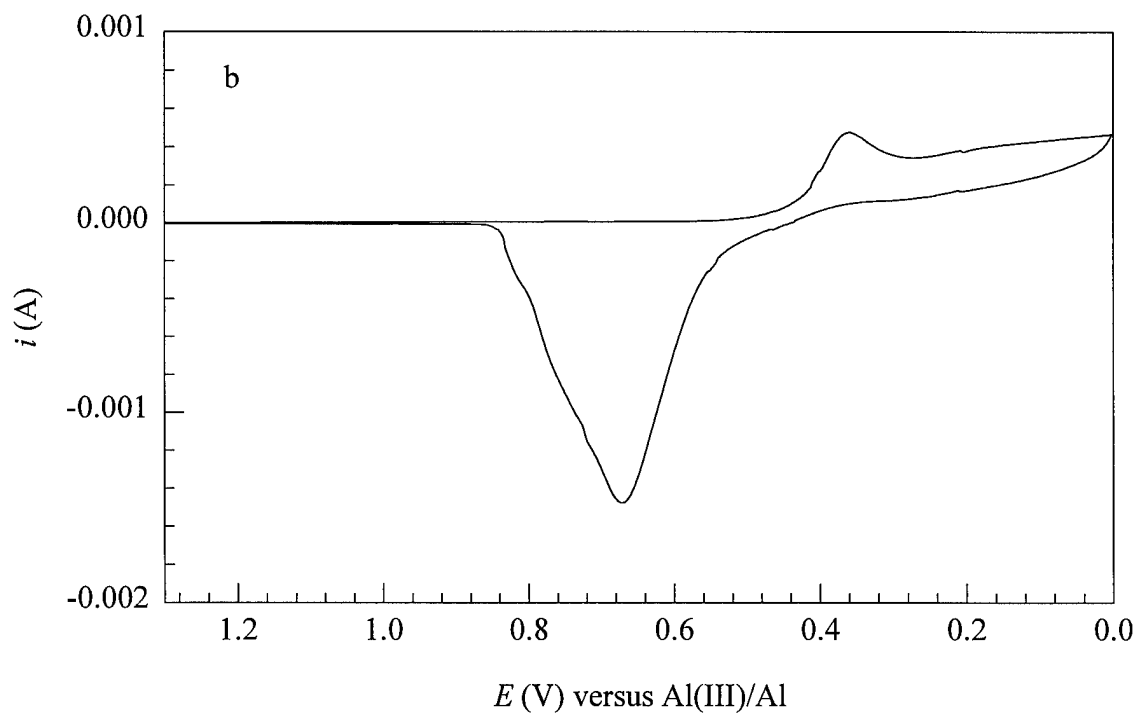
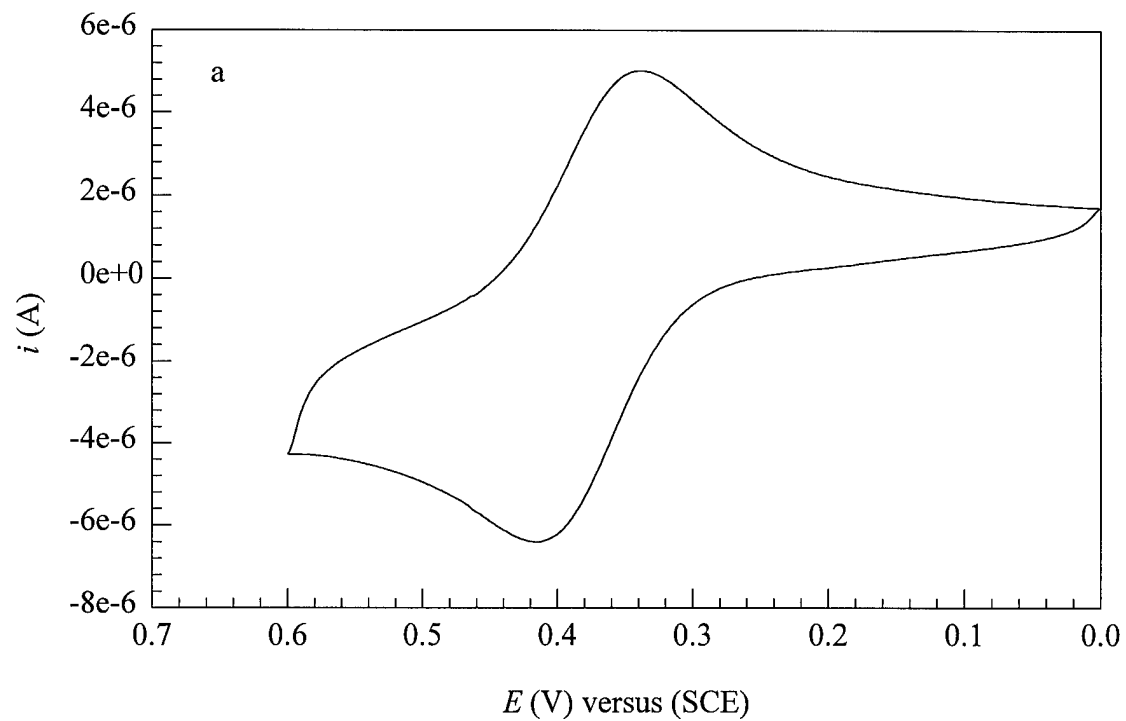


Figure 2.1 (a) Typical cyclic voltammogram for a freely diffusing reversible electrode couple. (b) Cyclic voltammogram for the reduction and oxidation of a metal film on an electrode surface.

different from those for an electrode reaction in which both the oxidized and reduced species are soluble. Whereas the reduction or electrodeposition wave may seem typical of the latter, the oxidation or stripping wave is more narrow and symmetrical. This result is representative of the oxidation of a surface-bound material.

Rotating-disk electrode voltammetry uses the same potential sweep as used for cyclic or linear sweep voltammetry, but here the electrode is rotated at a fixed rate, and the scan rate is slower. By rotating the electrode at a fixed rotation rate, ω (s^{-1}), electroactive species are brought to the electrode surface by forced convection, and the current does not decay with time as seen in stationary electrode voltammetry. The result of rotating the electrode is that the diffusion layer thickness at the electrode surface remains constant at a given rotation rate, and thus the diffusion layer thickness is constant. A comparison between stationary and rotating electrodes is shown in Figure 2.2. The magnitude of the limiting current is given by the Levich equation(72)

$$i_l = 0.62 nFAD_o^{2/3} C_o^* \omega^{1/2} \nu^{-1/6} \quad [2.4]$$

where ω is the angular velocity of the electrode with units of s^{-1} , ($\omega = 2\pi$ rps, where rps is the number of revolutions per second), ν ($cm^2 s^{-1}$) is the kinematic viscosity, and the other quantities have their usual meaning. Rotating-disk electrode voltammetry can be used as a tool to identify surface deposits. For example, if the electroactive species is not deposited on the electrode surface, then the return scan will simply retrace the forward scan because the reduced product is swept away from the rotating electrode. Rotating-disk voltammetry is the

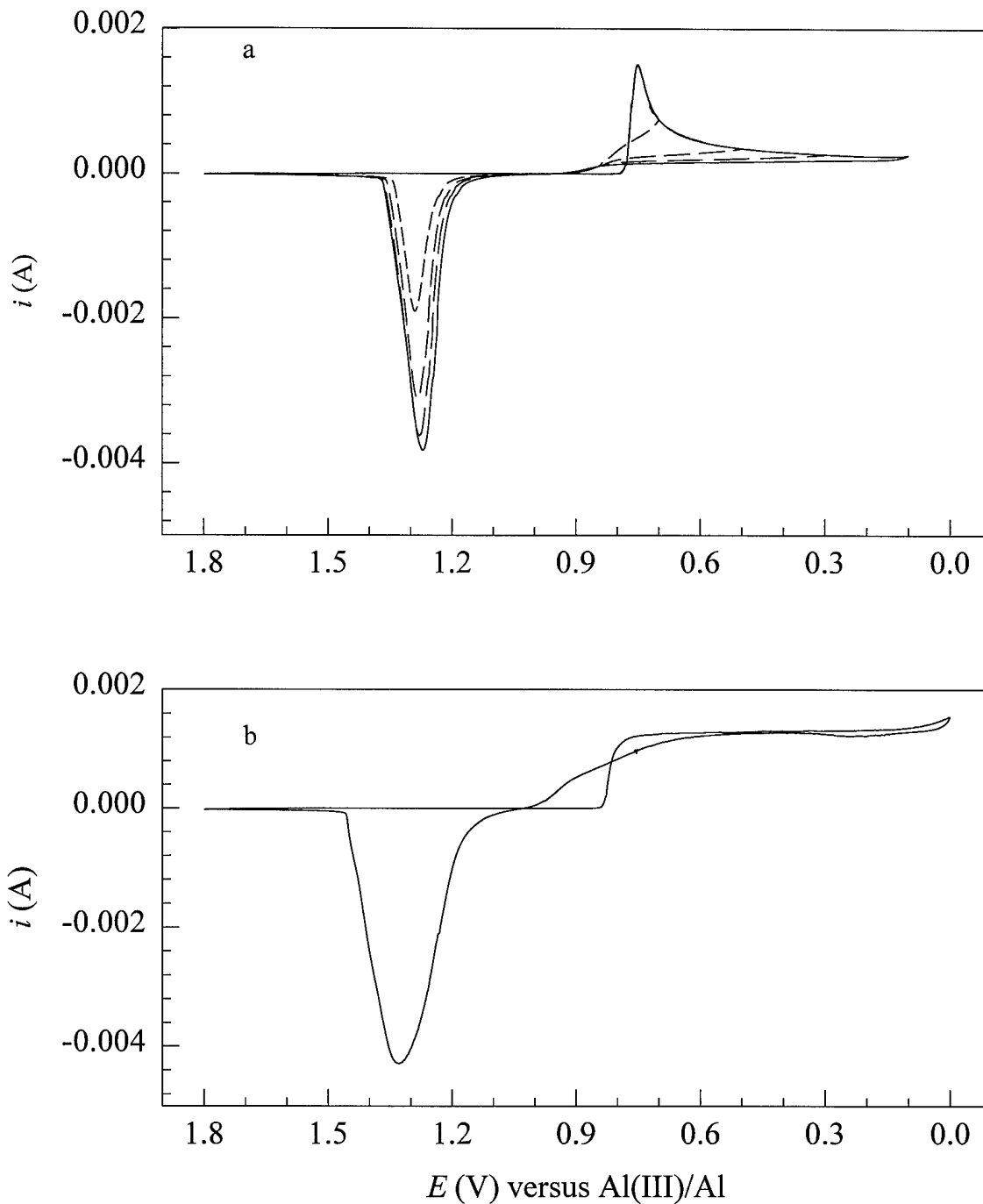


Figure 2.2. Comparison between stationary and rotating electrode voltammetry: (a, top) stationary glassy carbon electrode, (b, bottom) rotating glassy carbon electrode.

preferred technique for the precise, quantitative determination of diffusion coefficients, heterogeneous electron transfer rate constants, and some homogeneous rate constants.

Anodic linear sweep voltammetry (ALS_V) is a special case of rotating-disk electrode voltammetry. ALS_V entails two steps: *i*) the deposition of a thin layer onto the surface of a rotating-disk electrode by controlled-potential electrolysis and *ii*) a slow scan, (0.002 V s⁻¹) from E_{eq} in which the deposit is stripped from the electrode surface. As the potential is scanned from E_{eq} toward more positive potentials, different components of the electrodeposited film will be oxidized at their respective reversible potentials, revealing thermodynamically distinct phases in the deposit. ALS_V affords a quantitative look at each phase of an alloy because the quantity of each phase is proportional to the total charge of its representative stripping waves.(66,73)

Rotating ring-disk electrode (RRDE) voltammetry experiments are another method for gaining quantitative insight (74-76) into each phase of an alloy film. An RRDE consists of an electrode disk surrounded by a ring (usually of the same material) separated by a thin insulating gap. RRDE voltammetry typically utilizes a bipotentiostat that enables both the disk and ring to be held or swept at different potentials using the same reference and counter electrodes. The current at the disk is described by Equation 2.3 whereas the current at the ring is given by Equation 2.5

$$i_{\text{R}} = i_{\text{D}} (r_3^3 - r_2^3)^{2/3} / r_1^2 \quad [2.5]$$

where r_1 is the radius of the disk, r_2 is the distance from the center of the disk to the inner edge of the ring, and r_3 is the distance from the center of the ring to the outer edge of the ring. The most common type of experiment performed with the RRDE is a collection experiment. Here the disk is held at a cathodic potential sufficient to generate the reduced species at the disk at the mass-transport limited rate while the ring is held at a more positive potential.

The RRDE thin-layer deposition-stripping experiments conducted during this investigation are similar in principle to those described by Andricacos *et al.* (72, 77, 78) and Bruckenstein (74-76). In these ALSV-RRDE experiments, a thin film is first deposited onto the disk electrode by holding the potential at the desired potential as determined from the sampled-current voltammograms, while the ring electrode is held at a potential high enough so that no reduction of the metal ions of interest occurs. During the anodic dissolution step, the ring electrode potential, E_r , is held at a value that results in the oxidation of the metal ions of one of the alloy components produced at the disk. For example, during the anodic dissolution of Ni-Fe alloys, both iron(II) and nickel(II) are produced at the disk electrode, and E_r is set to a value where iron(II) is oxidized to iron(III). Because nickel(II) cannot be oxidized within the potential window of the solvent, the oxidation waves that correspond to the dissolution of iron from the alloy deposit can be identified by observing the ring current as a function of the disk potential (77). The alloy composition can be calculated from the ring and disk charges, Q_r and Q_d , respectively, and knowledge of the experimental collection efficiency, N_{exp} , of the RRDE electrode.

CHAPTER III. ELECTRODEPOSITION OF COBALT

3.1 Anodization of cobalt

Solutions of cobalt(II) in the 60.0-40.0 m/o AlCl_3 -MeEtimCl melt were prepared by the controlled-potential coulometric anodization of a coiled cobalt wire working electrode at an applied potential of 1.4 V versus Al(III)/Al . To ensure that cobalt(II) was the anodization product, the change in weight of the cobalt electrode was determined after the passage of a given charge, Q_{exp} . The data produced during several such controlled-potential coulometry experiments are given in Table 3.1. In this table, Δw_{Co} is the change in the weight of the cobalt electrode, m_{Co} is the number of moles of cobalt corresponding to this weight change, and $Q_{\text{theory}}(n = 1)$ is the theoretical charge based on m_{Co} for $n = 1$. These calculations confirm that cobalt(II) was the anodization product.

Nernst plots were constructed from data obtained during the coulometry experiments described above in order to determine the formal potential, $E^{\circ'}$, of the Co(II)/Co couple. These data were obtained by periodically interrupting these experiments after the passage of various fractions of Q_{exp} and then measuring the equilibrium cell potential, E_{eq} , under open circuit conditions. The average intercepts of four Nernst plots yielded $E^{\circ'} = 0.86 \pm 0.02$ V. The slopes of these plots gave $n = 2.0 \pm 0.2$ in good agreement with the anodic dissolution results.

Table 3.1 Results for the anodization of cobalt.

Δw_{Co} (g)	$10^4 m_{\text{Co}}$ (mol)	$Q_{\text{theory}}(n = 1)$ (C)	Q_{exp} (C)	n
0.1177	19.97	192.95	385.9	2.00
0.0179	3.04	28.78	59.14	2.02
0.0452	7.67	74.35	148.69	2.01
0.0258	4.38	38.36	76.72	1.82
0.0489	8.29	85.00	170.00	2.12

avg: 2.0 ± 0.2

3.2 Cyclic and rotating disk electrode voltammetry of cobalt(II)

Figures 3.1 to 3.4 show voltammograms for the reduction of cobalt(II) at platinum, gold, tungsten, and glassy carbon electrodes, respectively, in an unstirred 0.043 M solution of cobalt(II) at 25 °C. The results seen with each of these electrodes are very similar; thus, only the results at platinum will be described in detail. The cyclic voltammograms in Figure 3.1a exhibit broad reduction waves on the forward scan with a peak potential, E_p^c , ca. 0.65 V. This wave is due to the electrodeposition of pure cobalt.



As the potential was scanned below about 0.4 V, the current begins to rise again, indicating the presence of yet another reduction process.

On the reverse scan, multiple oxidation waves are observed. The number of waves and their peak potentials are highly dependent upon E_λ . For an E_λ of 0.4 V or higher, there is a single oxidation wave at ca. 1.0 V. This wave is attributed to the stripping of pure cobalt as the potential is not sufficiently cathodic to cause the co-deposition of aluminum. As E_λ is made more cathodic than 0.4 V, a second wave with a peak potential ca. 0.75 V begins to grow, shifting anodically as E_λ is lowered. The presence of the second wave is associated with the onset of the second reduction process during the forward scan. These two waves never appear as two distinct entities, but instead, they always seem to overlap. At $E_\lambda = 0.2$ V, a shoulder begins to develop, and it becomes a distinct, third stripping wave when $E_\lambda = 0$ V. The peak potential of this wave shifts cathodically as the wave becomes more distinct.

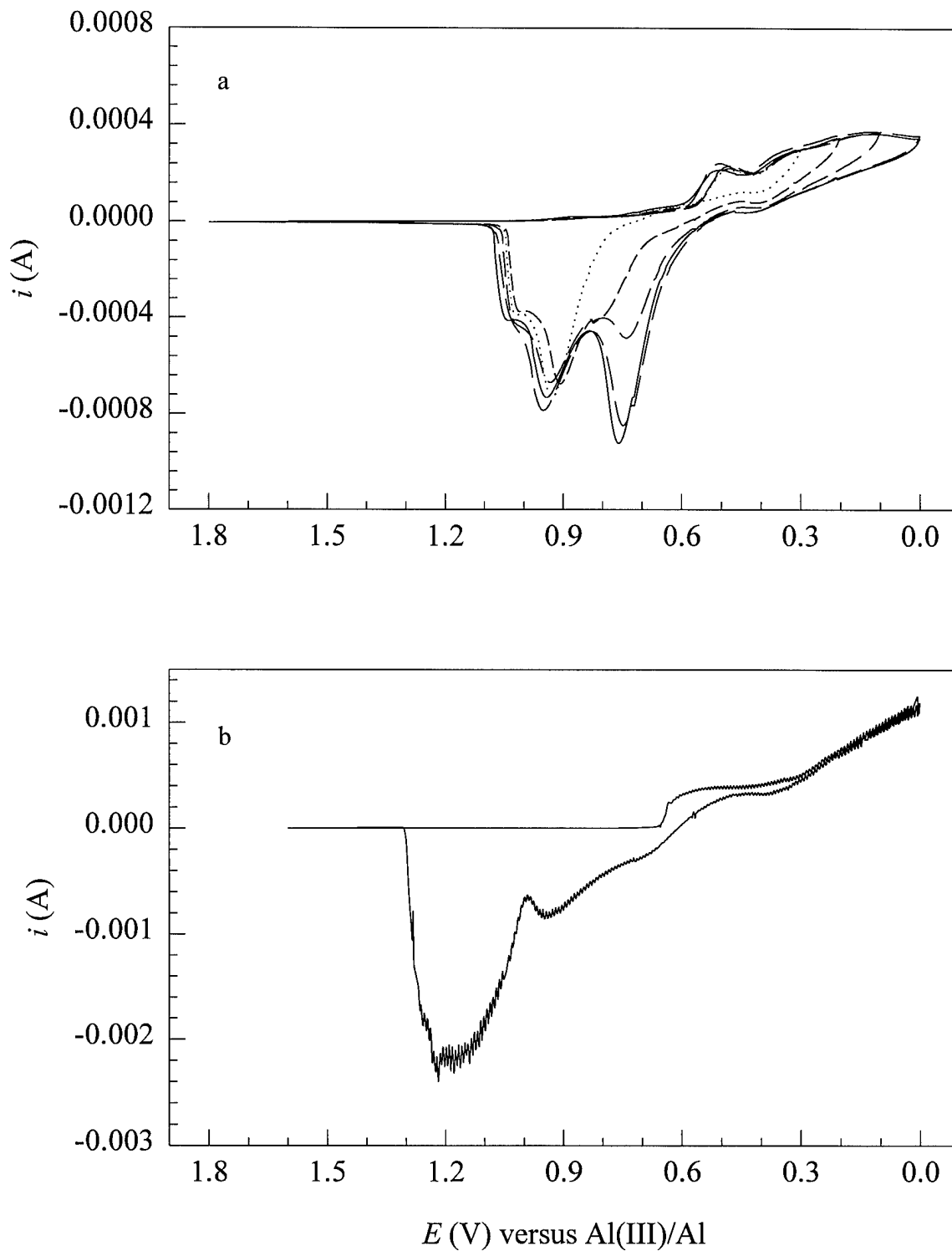


Figure 3.1 Voltammograms recorded at a platinum electrode in a 0.043 M solution of Co(II) in 60.0-40.0 m/o AlCl_3 -MeEtimCl at 25 °C: (a) stationary electrode (scan rate = 0.050 V s^{-1}), (b) RDE (rotation rate = 104.7 s^{-1}).

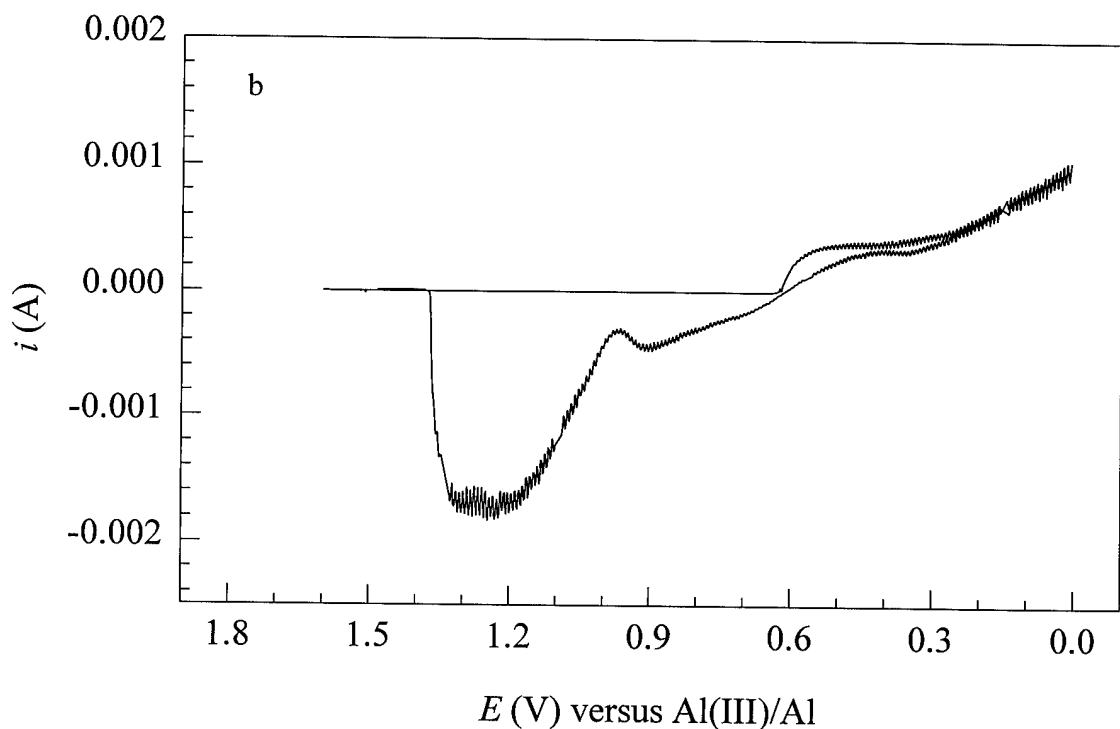
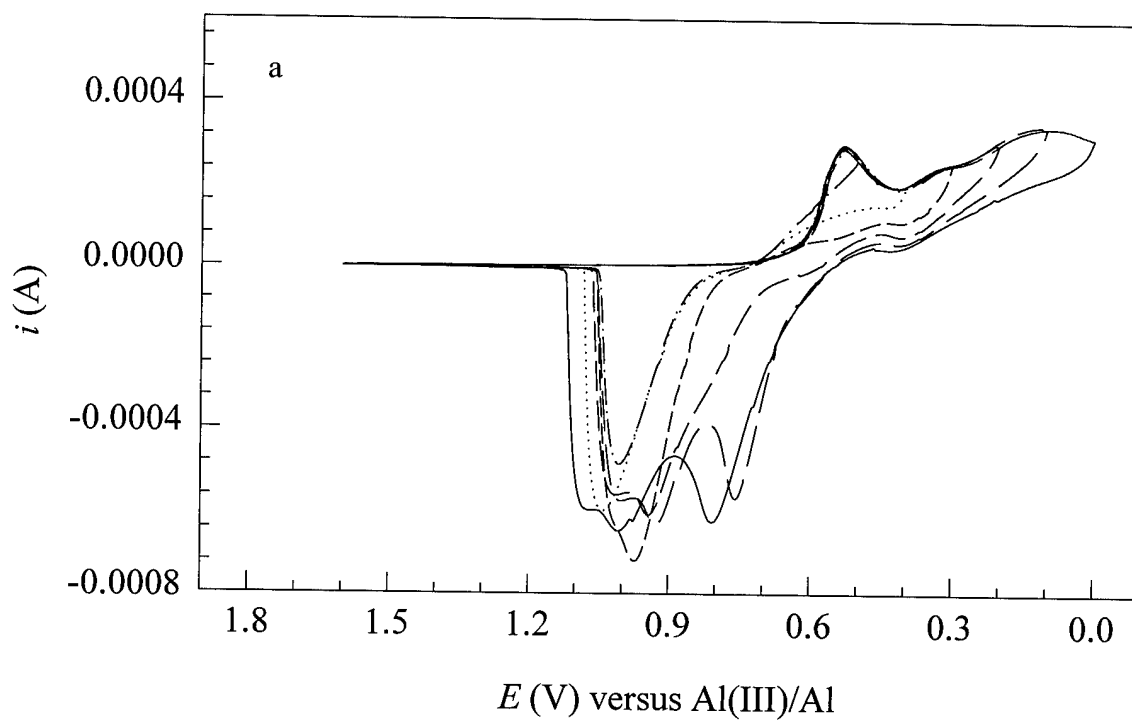


Figure 3.2 Voltammograms recorded at a gold electrode in a 0.043 M solution of Co(II) in 60.0-40.0 m/o AlCl_3 -MeEtimCl at 25 °C: (a) stationary electrode (scan rate = 0.050 V s^{-1}), (b) RDE (rotation rate = 104.7 s^{-1}).

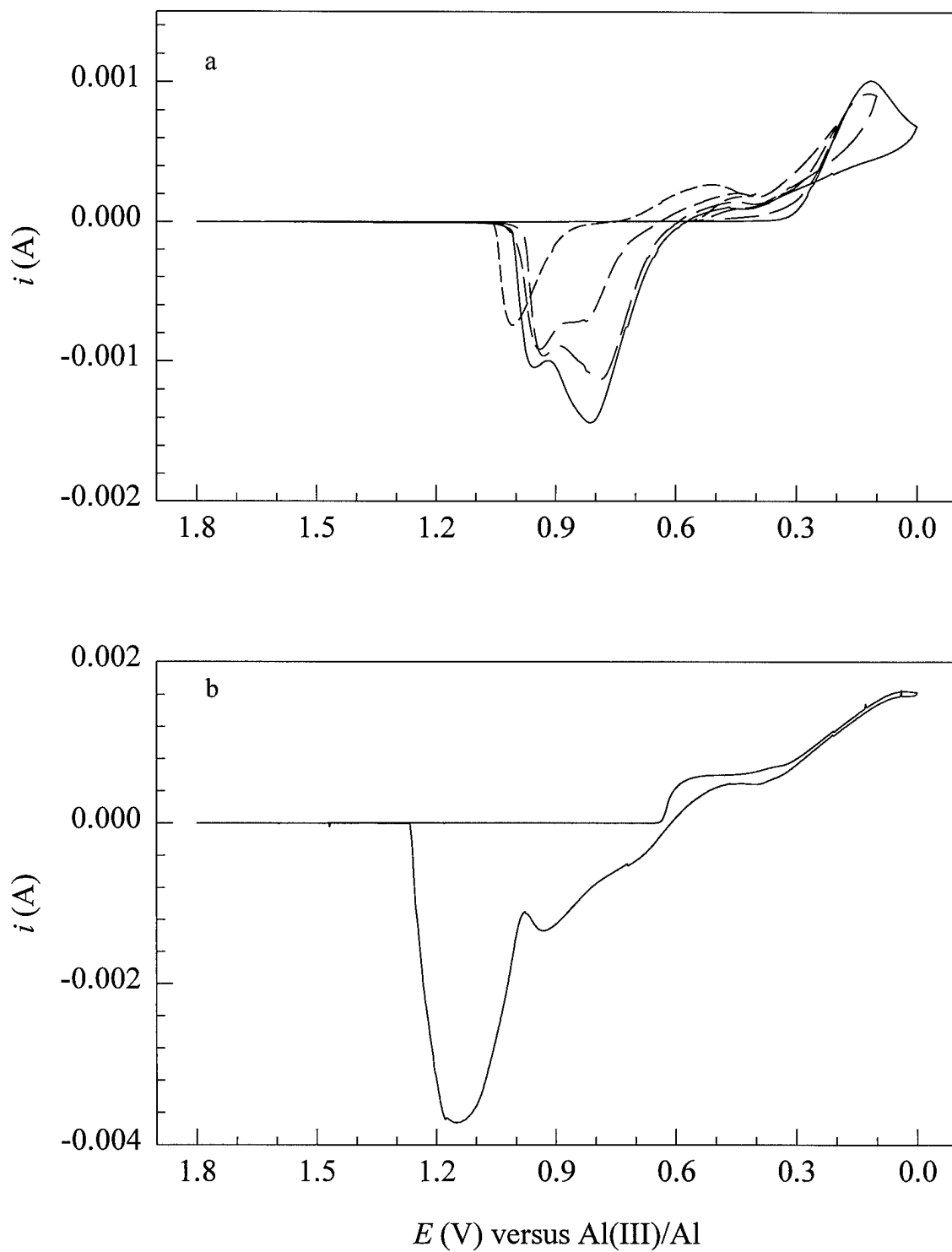


Figure 3.3 Voltammograms recorded at a tungsten electrode in a 0.043 M solution of Co(II) in 60.0-40.0 m/o AlCl₃-MeEtimCl at 25 °C: (a) stationary electrode (scan rate = 0.050 V s⁻¹), (b) RDE (rotation rate = 104.7 s⁻¹).

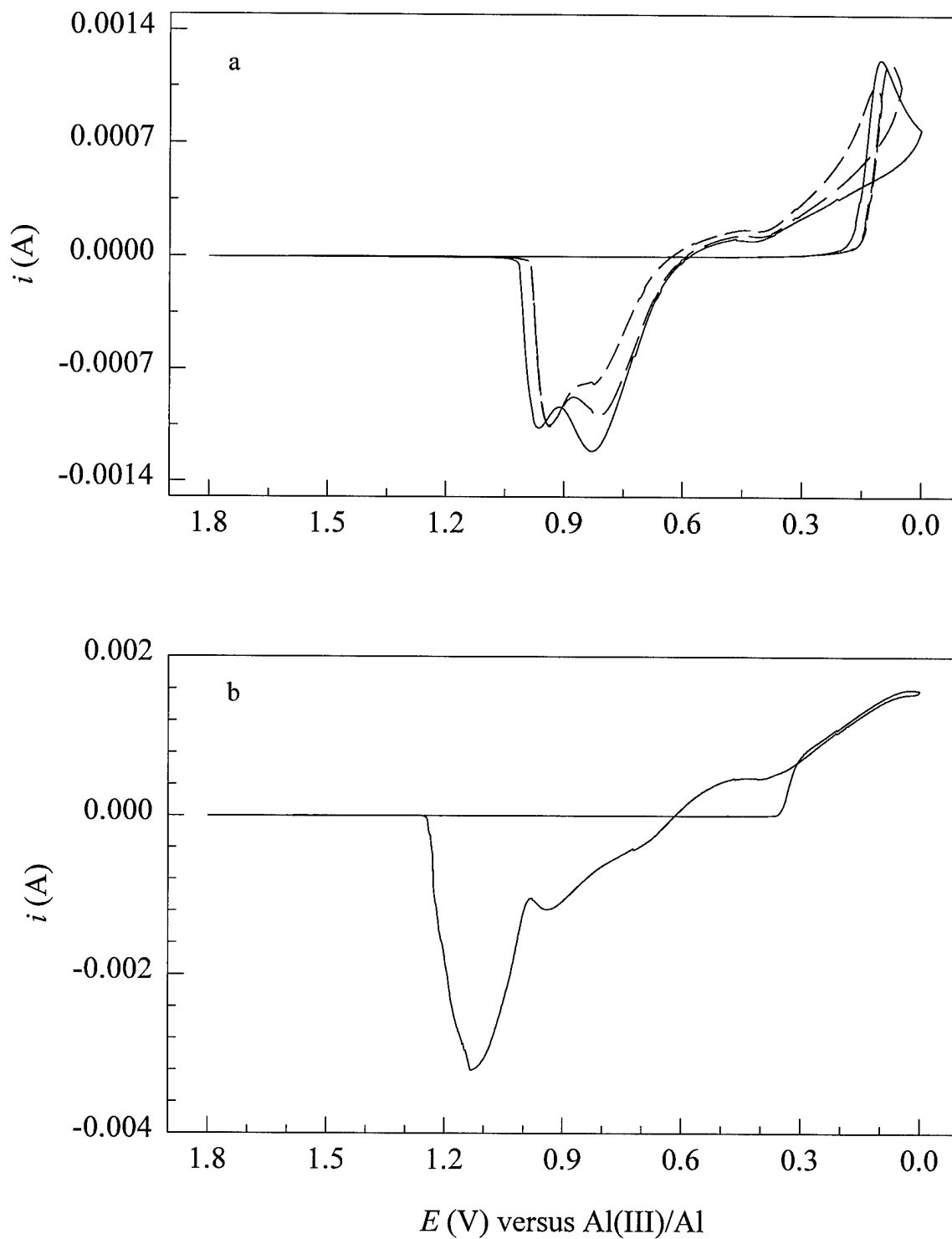


Figure 3.4 Voltammograms recorded at a glassy carbon electrode in a 0.043 M solution of Co(II) in 60.0-40.0 m/o AlCl_3 -MeEtimCl at 25 °C: (a) stationary electrode (scan rate = 0.050 V s^{-1}), (b) RDE (rotation rate= 104.7 s^{-1}).

Figures 3.1 to 3.4 show RDE voltammograms for the reduction of cobalt(II) at the same electrodes that were used to acquire the stationary electrode cyclic voltammograms. During the forward scan, the current reaches a well-defined limiting-current plateau as the potential is scanned between 0.6 and 0.3 V. At about 0.3 V, the current begins to rise in an almost linear fashion. The current in excess of the limiting current is attributed to a second reduction process or to the formation of a dendritic deposit. Sampled-current voltammograms were collected in order to determine whether the rise in current seen at and below 0.3 V is due to the formation of dendrites or to the co-deposition of aluminum with cobalt.

3.3 Sampled-current voltammetry for the reduction of cobalt(II)

Sampled-current voltammograms were constructed from chronoamperometric current-time transients resulting from experiments at polycrystalline platinum in unstirred solutions of cobalt(II). In these experiments, the potential was stepped from an initial value of 1.5 V, where no Faradaic process occurs, to potentials ranging from 0.8 to 0 V; the solution was stirred and then allowed to rest before the application of each potential pulse. The current was sampled at the same elapsed time for each current-time transient and plotted as a function of potential. In order to insure a reproducible response, the electrode surface was cleaned by stepping the rotating electrode to 1.8 V for 60 s before each potential step experiment. Unlike the usual cyclic and rotating disk voltammetry experiments, these experiments do not involve the deposition of large amounts of material, and hence, they do not foster the formation of dendritic growths. The sampled-current voltammograms that resulted from these experiments are shown in Figure 3.5. These voltammograms exhibit a

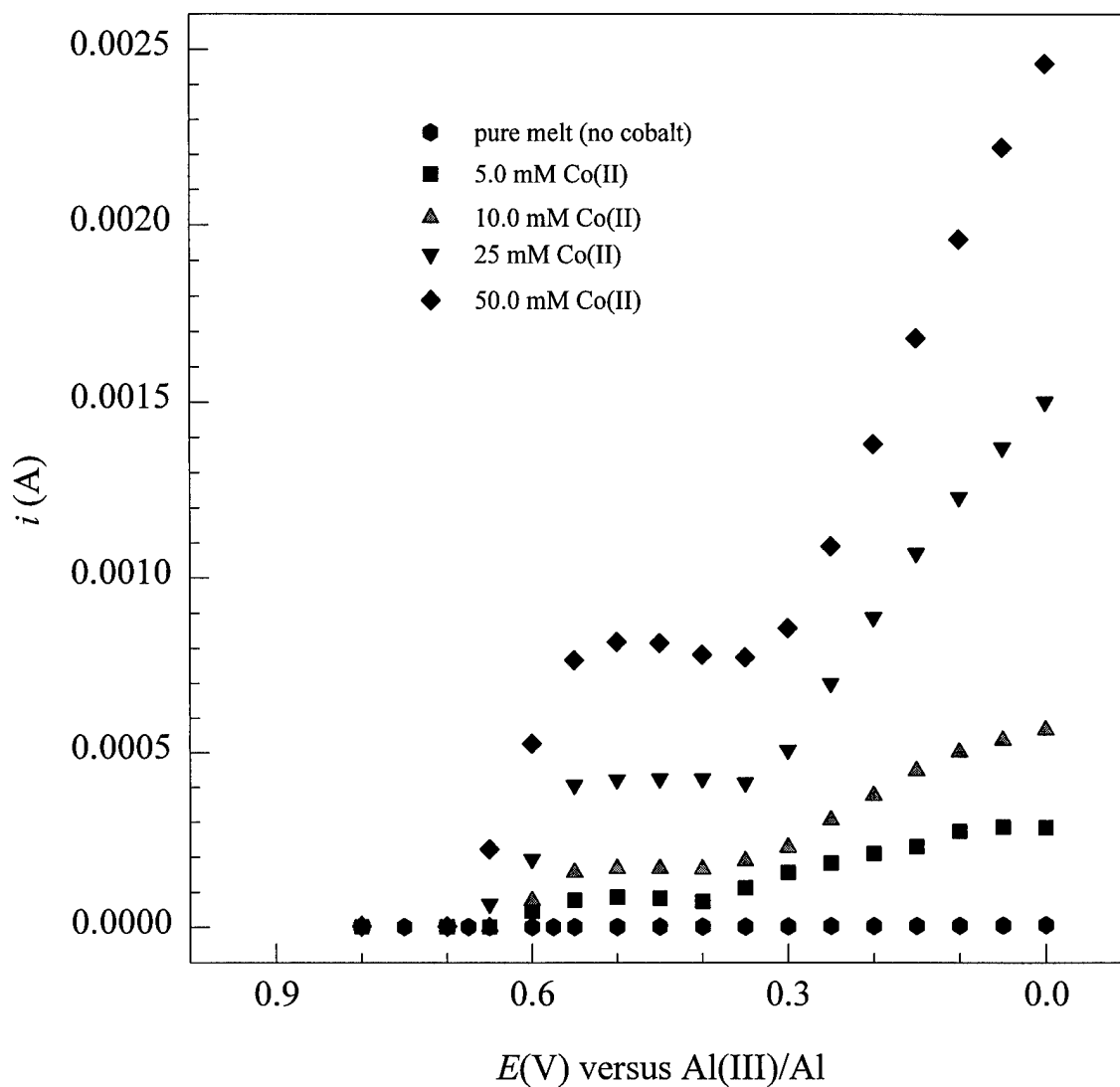


Figure 3.5 Sampled-current voltammograms of cobalt for the reduction of cobalt (II) at a platinum rotating disk electrode in the 60.0-40.0 m/o AlCl₃-MeEtimCl melt at 25 °C.

limiting current when the potential is stepped to values slightly more cathodic than 0.6 V. The current begins to increase above the limiting current at potentials more cathodic than 0.3 V. Plots of the limiting current density, j_1 , versus the inverse square root of the sampling time, $t^{-1/2}$, are linear as predicted by Equation 2.4. The average value of the diffusion coefficient of cobalt(II), $D_{\text{Co(II)}}$, calculated from the slope of j_1 versus $t^{-1/2}$ plots using Equation 2.1, and the Stokes-Einstein product, $D_{\text{Co(II)}}\eta/T$, where η is the absolute viscosity and T is the absolute temperature, were determined to be $(3.4 \pm 0.1) \times 10^{-7} \text{ cm}^2 \text{ s}^{-1}$ and $(1.8 \pm 0.1) \times 10^{-10} \text{ g cm s}^{-2} \text{ K}^{-1}$, respectively.

The rise in current seen in Figure 3.5 at potentials lower than 0.3 V is attributed to the co-deposition of aluminum. This was verified by EDS analysis of cobalt deposits produced at potentials between 0.4 and 0 V. The formation of this alloy deposit is represented by the following general reaction



where x is the mole fraction of cobalt, $1-x$ is the mole fraction of aluminum, and $0 < x < 1$. Because the limiting current at potentials between 0.6 and 0.4 V is due to the electrodeposition of pure cobalt

$$i_{\text{Co}} = i_1 \quad [3.3]$$

it is possible to separate the partial current for the electrodeposition of aluminum from the total current.

$$i_{Al} = i_T - i_1 \quad [3.4]$$

The composition of the Co_xAl_{1-x} alloy can be calculated from the partial currents by using the following equation.

$$x = (i_{Co}/2)/[(i_{Co}/2) + (i_{Al}/3)] = (i_1/2)/\{(i_1/2) + [(i_T - i_1)/3]\} \quad [3.5]$$

Figure 3.6 shows the alloy composition as calculated from the partial currents in Figure 3.5 using Equation 3.5. The co-deposition of aluminum begins at ca. 0.4 V and increases as the potential is made more cathodic. The mole fraction of aluminum reaches about 0.56 at 0 V prior to the bulk deposition of aluminum.

3.4 Underpotential deposition of cobalt

If the current in the potential region immediately preceding the bulk deposition of cobalt is greatly magnified, then a broad poorly-defined reduction wave with a peak potential of ca. 0.84 V is observed (Figure 3.7). The equilibrium potential of the Co(II)/Co couple in this solution is ca. 0.61 V; thus, these small surface waves must arise from the underpotential deposition of cobalt on platinum. Integration of the reduction current in the potential envelope extending from 1.00 to 0.75 V gives a charge of ca. 4.53×10^{-5} C. (The choice of

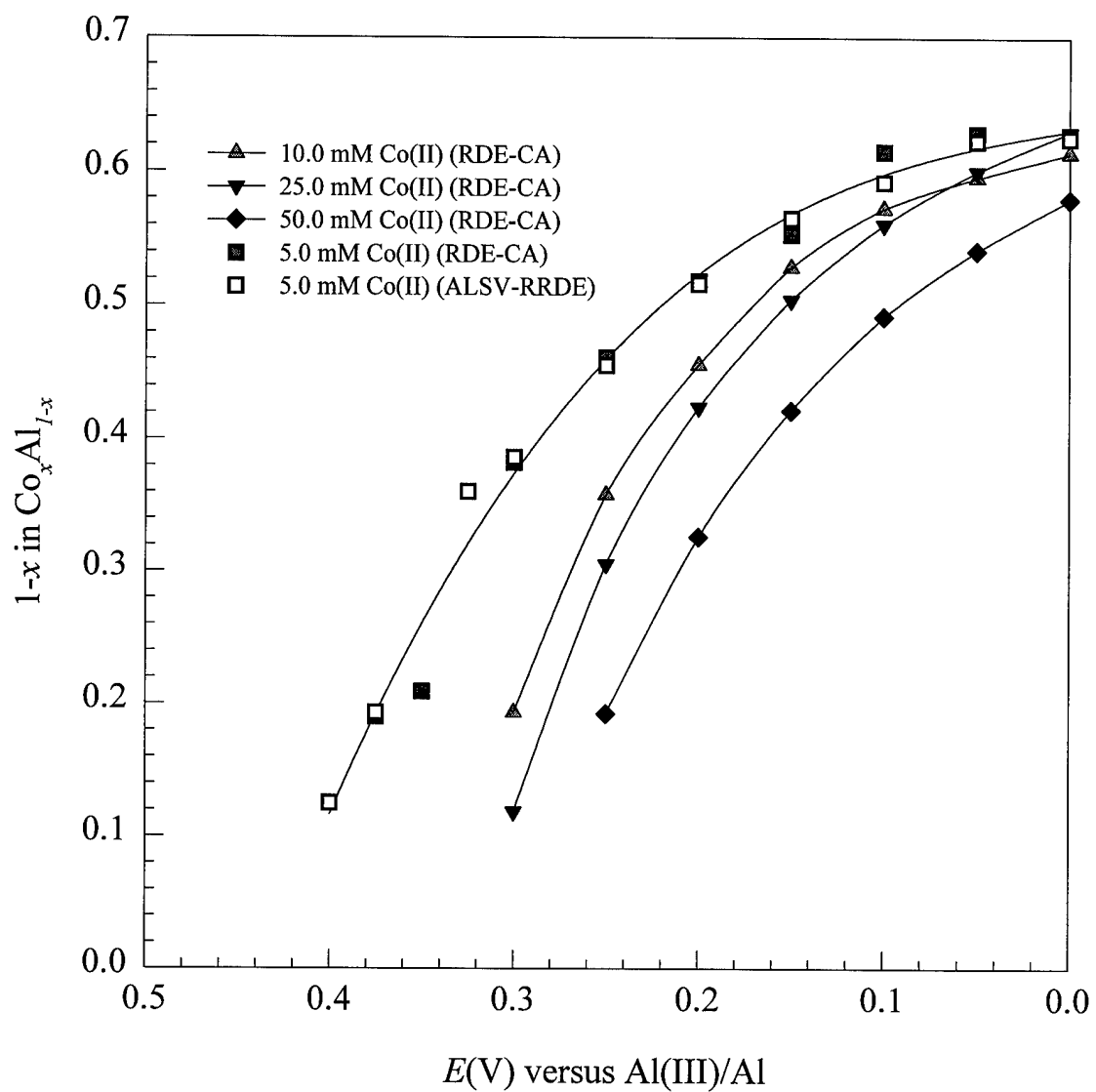


Figure 3.6 Composition of $\text{Co}_x\text{Al}_{1-x}$ as a function of the applied potential.

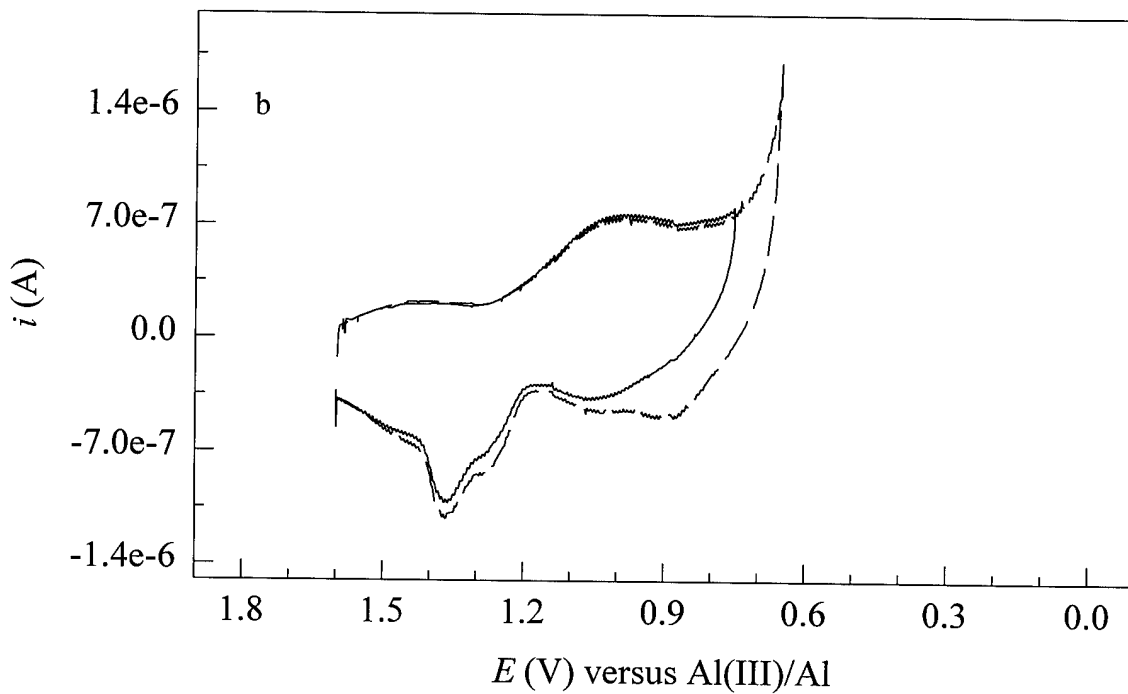
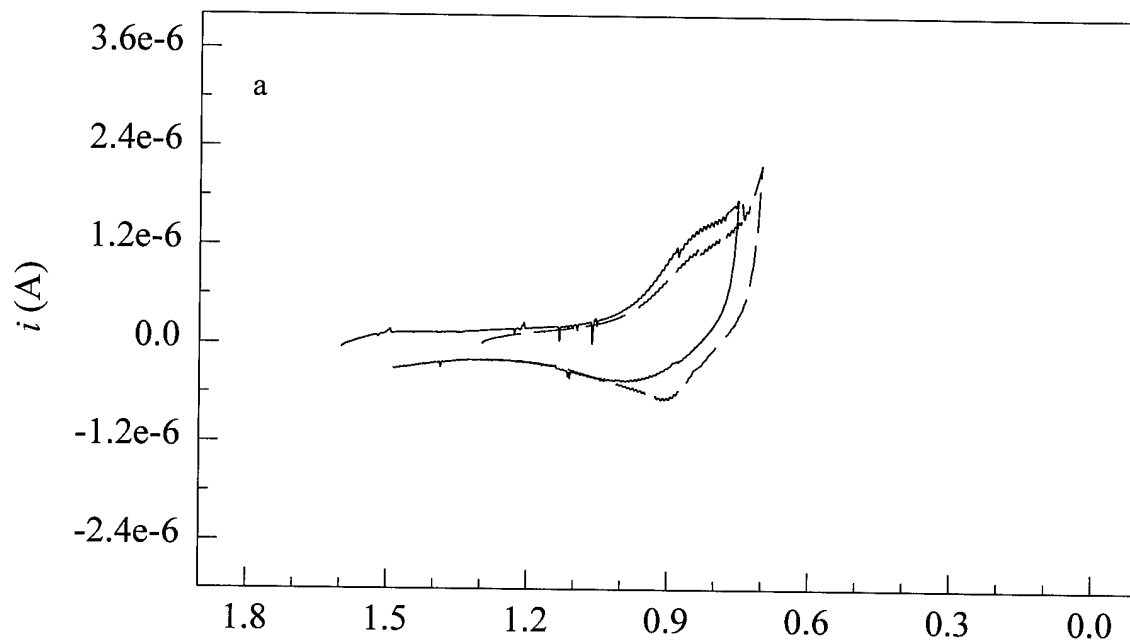


Figure 3.7 Underpotential deposition of cobalt in 60.0-40.0 m/o melt: (a) platinum RDE. (b) gold RDE.

the potential envelope over which the current is integrated is subjective; therefore, only approximate UPD charges are given for each of the polycrystalline metal electrodes.) Assuming a roughness factor of 1.1, the charge corresponding to the electrodeposition of a monolayer of cobalt on the platinum RDE used in these experiments is estimated to be about 4.6×10^{-5} C. Thus, the reduction current in the potential envelope described above represents the deposition of approximately one monolayer of cobalt on the platinum substrate. The underpotential deposition of cobalt can also be seen at the gold RDE (Figure 3.7b). The prominent features in the voltammogram are the symmetrical reduction wave with a peak potential at ca. 1.0 V and an associated stripping wave centered at 1.35 V. Integration of the reduction current in the potential envelope extending from 1.25 to 0.80 V yields a charge of 5.4×10^{-5} C. This charge is about the size of that expected for the deposition of a cobalt monolayer on this electrode (4.6×10^{-5} C), again assuming a surface roughness factor of 1.1.

In order for a cobalt-aluminum alloy to form at potentials more positive than the equilibrium potential of the Al(III)/Al couple, there must be a free energy advantage gained through alloy formation. To demonstrate that the UPD of aluminum can occur on a cobalt surface, cyclic voltammetric experiments were conducted at a polycrystalline cobalt disk electrode in blank 60.0-40.0 m/o melt (Figure 3.8). The cobalt working electrode was slowly scanned between 0.80 to 0 V. The only species available for reduction in pure melt at these potentials is Al_2Cl_7^- . The charge corresponding to the underpotential deposition of aluminum is about the size of that expected for the deposition of a monolayer on this electrode. The voltammogram is characterized by a reduction wave on the forward scan with $E_p^c = \text{ca. } 0.35$

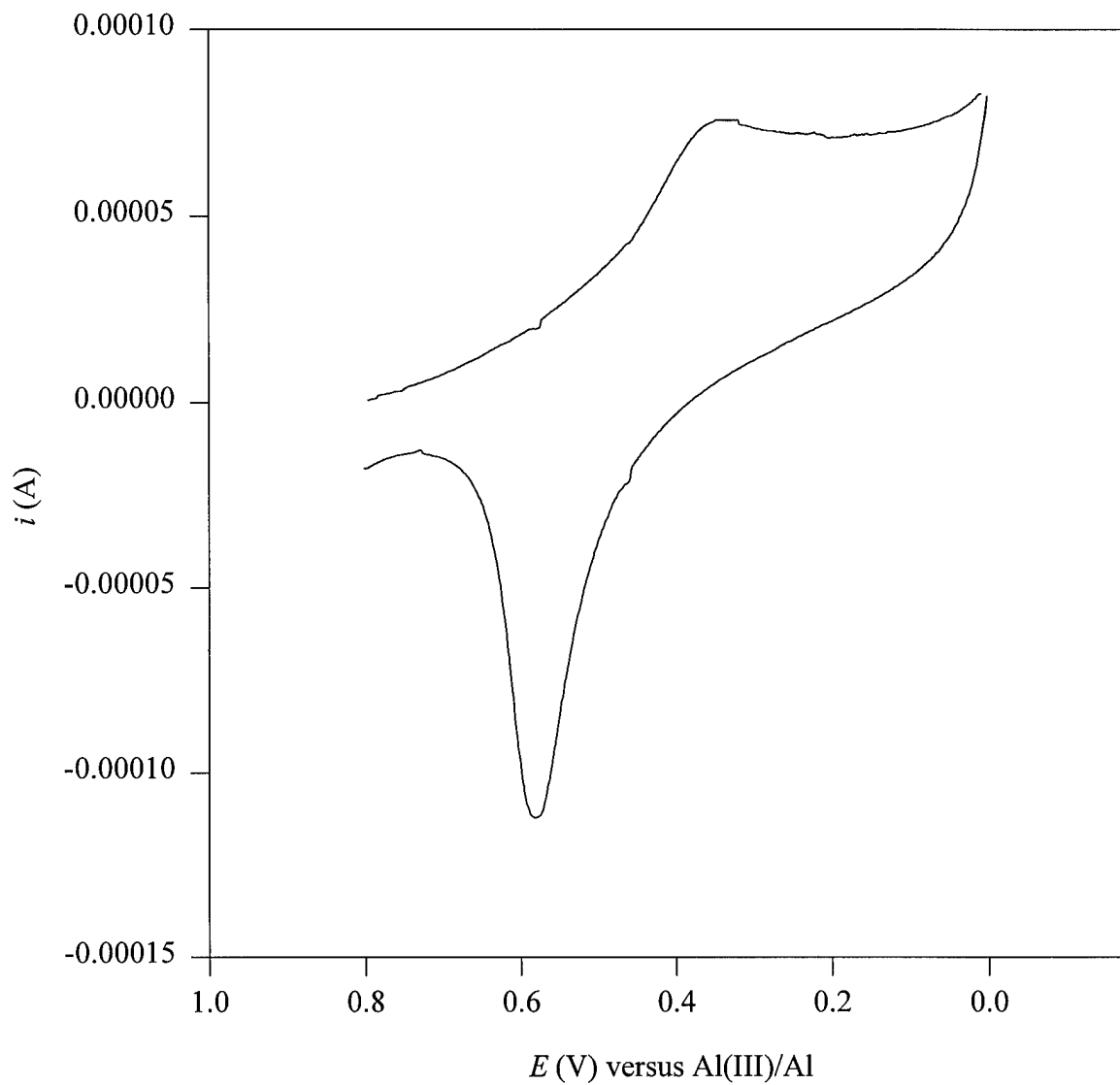


Figure 3.8 Underpotential deposition of aluminum onto a cobalt working electrode. This cyclic voltammogram was acquired in pure 60.0-40.0 m/o melt.

V and a well defined stripping wave on the reverse scan with $E_p^a = \text{ca. } 0.58 \text{ V}$. Thus, the UPD of aluminum onto cobalt is demonstrated, and it illustrates that there is an energetic driving force for the alloying of aluminum with cobalt at underpotentials.

3.5 Analysis of cobalt-aluminum thin films by anodic linear sweep voltammetry

In conjunction with previous work done in this laboratory, the composition of Co-Al alloy electrodeposits was examined by *in situ* anodic linear sweep voltammetry (ALSV) experiments at a platinum rotating disk electrode, ALSV-RDE. However, the ALSV-RDE method does not lead to an accurate alloy composition because it fails to account for all of the aluminum present.

The failure of the ALSV-RDE method led us to develop an alternative method based on ALSV at a rotating ring-disk electrode, which we denote as ALSV-RRDE. These thin-layer deposition-stripping experiments are similar in principle to those described by Andricacos et al. (77-78) and Swathirajan and Bruckenstein (74-76). In the ALSV-RRDE experiment, a thin film is first deposited onto the disk electrode by holding the electrode potential at the desired value as determined from the sampled-current voltammograms, while the ring electrode is held at open circuit. During the anodic dissolution step, the ring electrode potential, E_r , is normally held at a value that results in the oxidation of the metal ions of one of the alloy components produced at the disk. For example, during the anodic dissolution of Ni-Fe alloys, both iron(II) and nickel(II) are produced at the disk electrode, and E_r is set to a value where iron(II) is oxidized to iron(III). Because nickel(II) cannot be oxidized within the potential window of the solvent, the oxidation waves that correspond to

the dissolution of iron from the alloy deposit can be identified by observing the ring current as a function of the disk potential (77). The alloy composition can be calculated from the ring and disk charges, Q_r and Q_d , respectively, and knowledge of the experimental collection efficiency, N_{exp} , of the RRDE electrode.

In the present case, neither aluminum(III) or cobalt(II), the Co-Al alloy dissolution products, can be oxidized further within the potential window of the melt. However, by setting E_r to 0.5 V, it is possible to selectively reduce the cobalt(II) produced during the anodic dissolution of Co-Al alloy at the ring, permitting identification of those alloy stripping waves that have a current component that arises from the oxidation of cobalt. However, before this method can be employed, N_{exp} must be determined. Collection experiments were carried out by electrodepositing cobalt metal on the disk electrode at a potential of 0.5 V in a solution of cobalt(II) with the ring electrode inactive. The cobalt was then anodically dissolved from the disk in pure melt with slow scan (0.002 V s^{-1}) ALSV while the ring was held at 0.5 V. These experiments yielded a value of $N_{\text{exp}} = 0.221$; this is in excellent agreement with the theoretical collection efficiency of 0.220 for this ring-disk electrode, which was calculated from, r_1 , r_2 , and r_3 , respectively (72).

In view of these very favorable results, a series of ALSV experiments were carried out at the Pt-RRDE over the range of deposition potentials where the formation of Co-Al alloy is expected, *i.e.*, from 0.4 to 0 V. In these experiments, 425 mC cm^{-2} electrodeposits were produced on the disk electrode in a 0.005 M solution of cobalt(II). During a previous study of Ni-Al alloys, the deposit composition was found to depend on the charge density (40). This phenomenon is believed to arise from the thermodynamic instability of aluminum in the

alloy in solutions of nickel(II). The Co-Al alloy was found to display similar instability in cobalt(II) solutions, and a minimum charge density of ca. 325 mC cm^{-2} was needed to obtain Co-Al deposits whose compositions did not vary with the deposition charge. Figure 3.9 is a plot of the atomic fraction of aluminum versus the deposition charge. This plot illustrates the dependence of the composition on the latter. The electrode was then transferred to pure melt, and the Co-Al electrodeposit was slowly oxidized from the disk by ALSV while the ring was held at 0.5 V. The elapsed time that the plated electrode spent in the plating solution under open circuit conditions was kept to less than 15 seconds, the reason for this is depicted in Figure 3.10. A plot of the alloy composition versus immersion time of the deposit in the plating solution reveals that the deposit composition is highly sensitive to the time the unbiased deposit is exposed to the plating bath. This is a reflection of the ability of Co(II) to oxidize aluminum from the Co-Al alloy.

Typical voltammograms illustrating the disk and corrected ring currents that resulted from several of these experiments are shown in Figures 3.11 and 3.12. For deposits produced at 0.4 V, the major feature of the disk voltammogram is a wave with an anodic peak potential, E_p^a , of 0.93 V. The large ring current that was observed as the disk potential was scanned through this stripping wave indicates that a major component of the current arises from the oxidation of cobalt in the deposit. However, the charge corresponding to this wave was slightly larger than the corrected ring charge, Q_r/N_{exp} , indicating that some of the current must be due to the oxidation of aluminum. For the deposit prepared at 0.3 V, the disk voltammogram (Figure 3.10) revealed oxidation waves with $E_p^a = 0.83$ and 0.55 V,

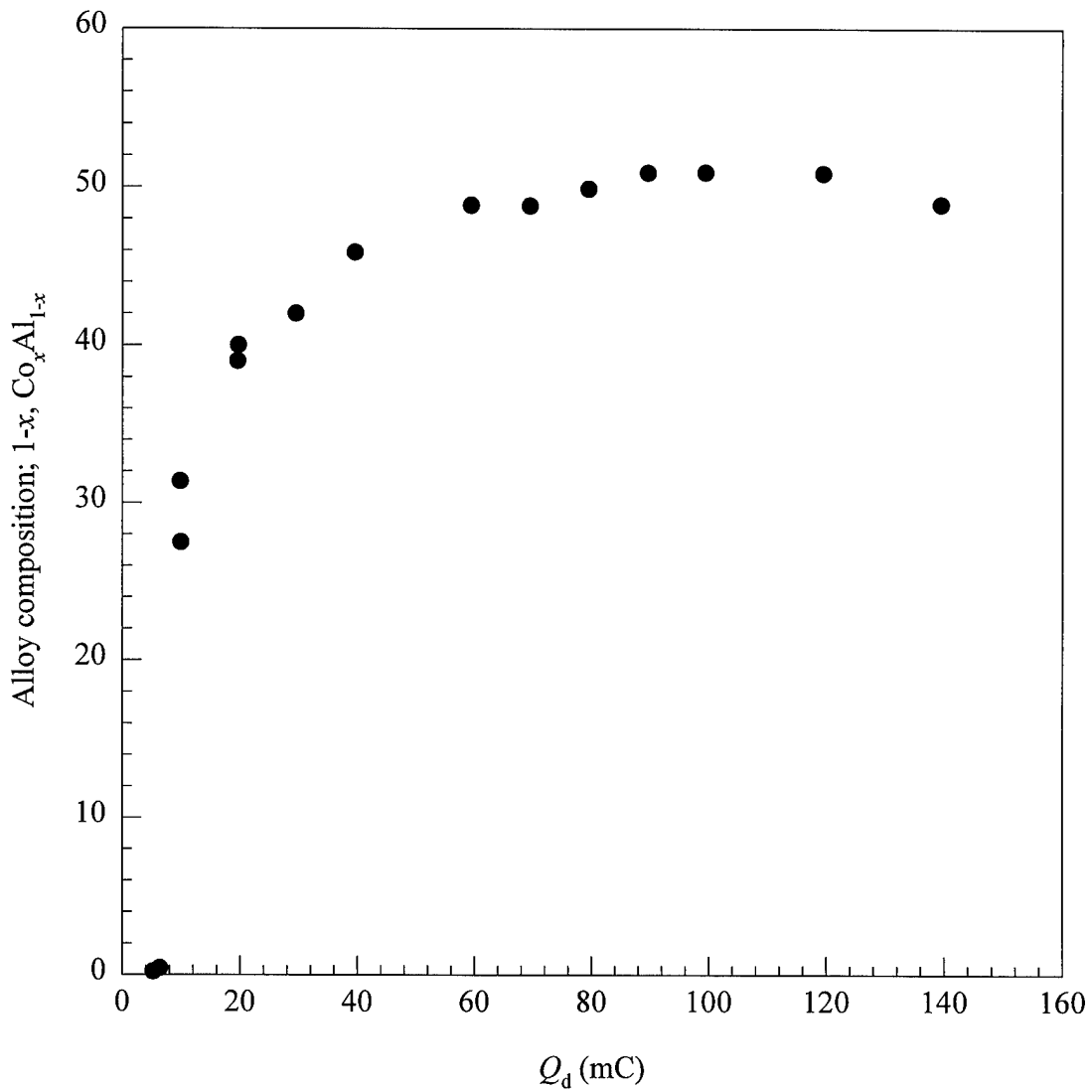


Figure 3.9 Dependence of the $\text{Co}_x\text{Al}_{1-x}$ electrodeposit composition on the deposition charge.

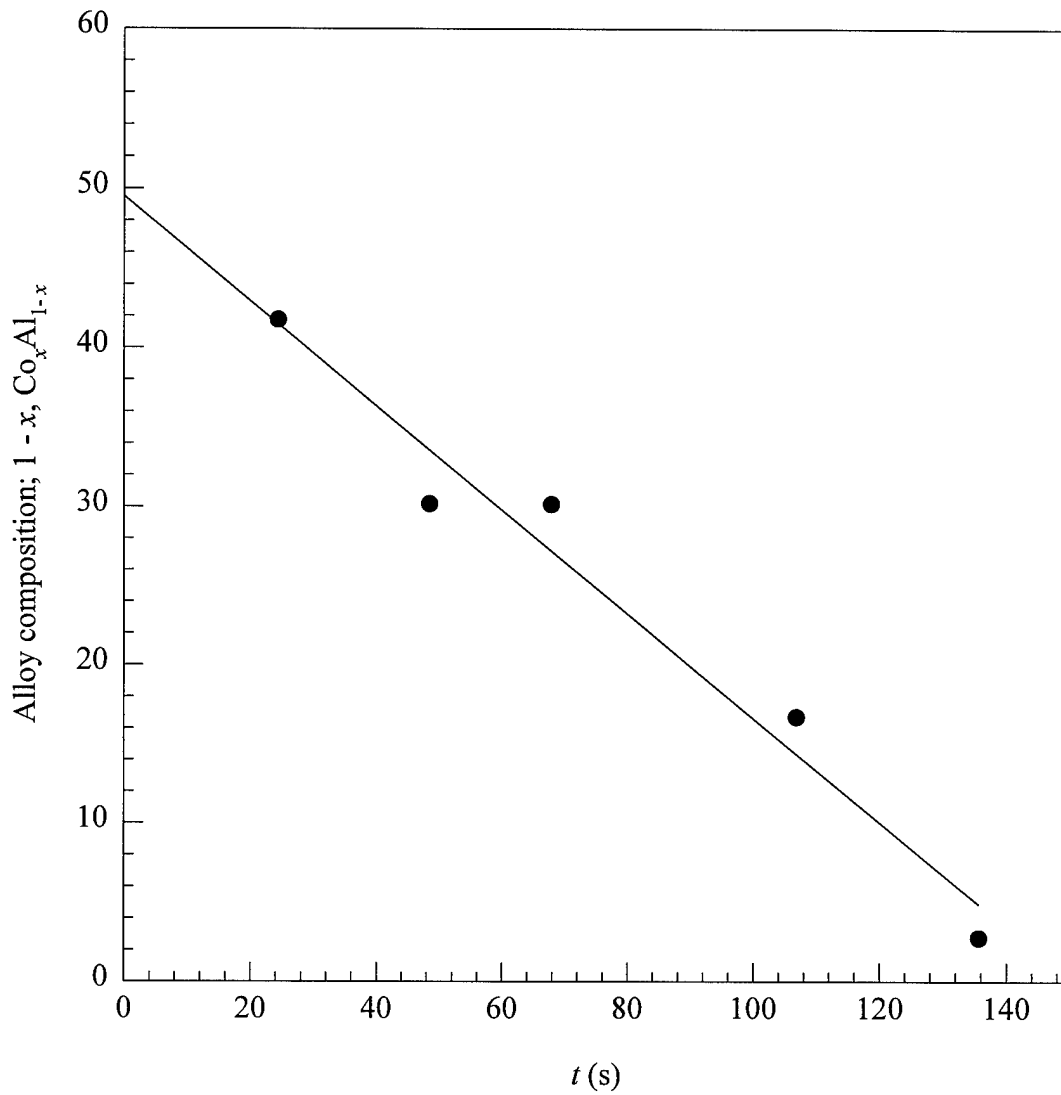


Figure 3.10 Variation of the $\text{Co}_x\text{Al}_{1-x}$ alloy composition with immersion time in a 0.025 M solution of Co(II) in 60.0-40.0 m/o melt.

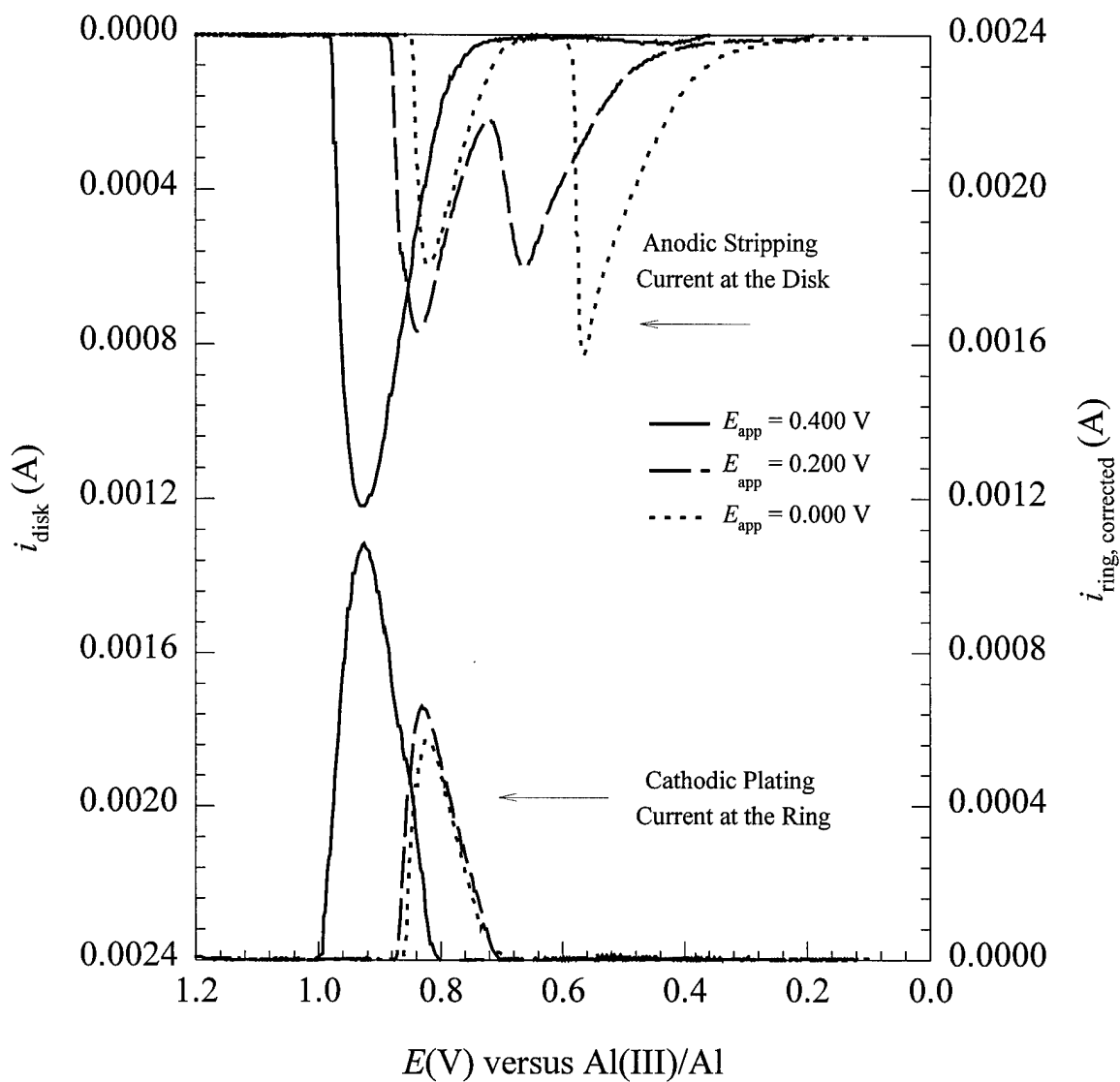


Figure 3.11 Disk and ring voltammograms recorded for the oxidation of thin layer Co-Al electrodeposits from a Pt-RRDE.

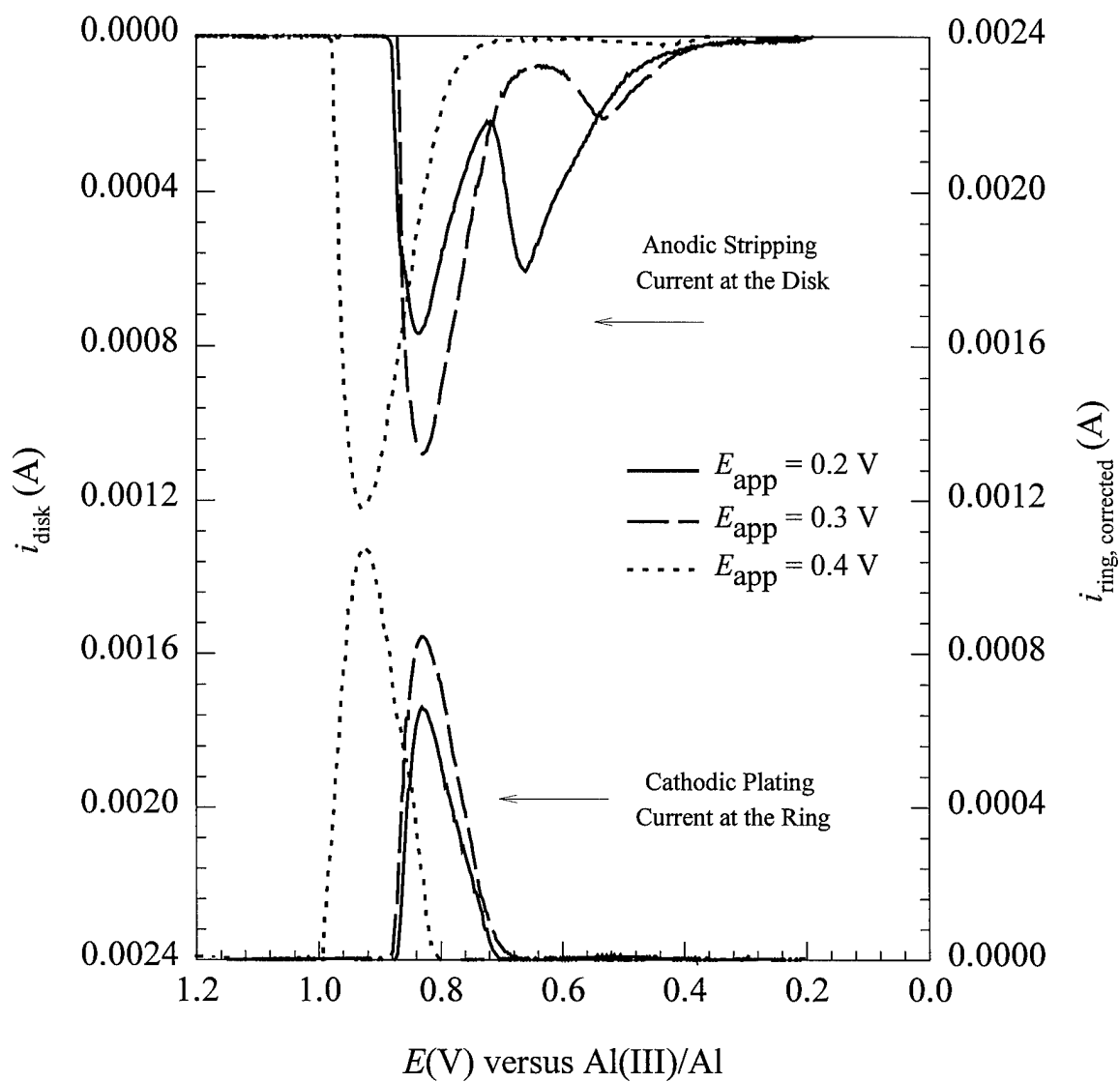


Figure 3.12 Disk and ring voltammograms recorded for the oxidation of thin layer Co-Al electrodeposits from a Pt-RRDE.

respectively. A ring current was associated with the former, but not the later, indicating that the wave at 0.55 V must arise from the selective removal of aluminum from the alloy. The disk voltammograms corresponding to the 0.20, 0.10, and 0 V deposits (Figure 3.12) were similar in appearance to that of the 0.30 V deposit, except that the aluminum stripping wave was shifted to $E_p^a = 0.67$ V in the case of the 0.20 V deposit and appeared at $E_p^a = 0.63$ and 0.56 V in the voltammograms of the 0.10 and 0 V deposits, respectively. However, most interestingly, a small amount of aluminum was also oxidized from each of these deposits at potentials proximate to the oxidation of cobalt, demonstrating that conventional ALSV methods are unsatisfactory for analyzing this alloy.

These shifts in the position of the aluminum stripping wave indicate that the activity of aluminum in the alloy is changing with the aluminum content of the alloy. However, it is unclear why aluminum dissolution occurs at two different potentials. Assuming that the deposit exists in two phases and that dissolution of the second phase is due to oxidation of the aluminum contained in a cobalt-rich phase, then the two phases cannot be in equilibrium because the aluminum activity must be different in each phase. Alternatively, the aluminum associated with the second dissolution process may simply be inaccessible to oxidation until some dissolution of cobalt occurs. The negative shift in the cobalt stripping wave that is associated with alloyed deposits may then be due to the more favorable dissolution kinetics of a porous cobalt layer over that of a pure, compact deposit (79). The characteristics of anodic linear sweep voltammograms for the dissolution of an alloy deposit are very sensitive to the composition and structure of the deposit. Theoretical and experimental studies have attempted to correlate peak shape and location with the type of alloy that is electrodeposited

(79,80). However, a detailed analysis of the voltammograms in Figures 3.11 and 3.12 beyond that given here would be purely speculative without reliable information about the phase distribution in Co-Al alloys containing up to 62 at/o aluminum. The alloy composition (1-x) as a function of deposition potential was calculated from N_{exp} and the values of Q_r and Q_d that resulted from numerous experiments similar to those described above by using the following expression:

$$1 - x = 1 / \{1 + 1.5 [Q_r / (N_{\text{exp}} Q_d - Q_r)]\} \quad [3.1]$$

The resulting values of 1 - x are plotted as a function of potential in Figure 3.6, and they are in very good agreement with the values of 1 - x derived from the sampled-current voltammetric plots observed in a 0.005 M cobalt(II) solution.

CHAPTER IV. ELECTRODEPOSITION OF IRON

4.1 Anodic dissolution of iron

Solutions of iron(II) in the 60.0-40.0 m/o AlCl_3 -MeEtimCl melt were prepared by the controlled-potential coulometric anodization of a coiled iron wire working electrode at an applied potential of 1.30 V versus Al(III)/Al . To ensure that iron(II) was the anodization product, the change in weight of the iron electrode was determined after the passage of a given charge, Q_{exp} . The results of several such controlled-potential coulometry experiments are given in Table 4.1. In this table, Δw_{Fe} is the change in the weight of the iron electrode, m_{Fe} is the number of moles of iron corresponding to this weight change, and $Q_{\text{theory}} (n = 1)$ is the theoretical charge based on m_{Fe} for $n = 1$. These calculations confirm that iron(II) was the anodization product.

RDE voltammetry was used to determine $E^{\circ'}$; E_{eq} was estimated from the zero current crossover point on the return sweep. The Nernst equation yielded $E^{\circ'} = 0.52 \pm 0.01$ V at the 95 % confidence level. Data from 20 RDE experiments were used in the calculation of $E^{\circ'}$.

4.2 Voltammetry of iron(II)

Stationary and RDE voltammograms for the electrodeposition and stripping of iron on platinum, tungsten, gold, and glassy carbon electrodes from an unstirred 0.050 M solution

Table 4.1 Results for the anodization of iron.

Δw_{Fe} (g)	$10^4 m_{\text{Fe}}$ (mol)	$Q_{\text{theory}}(n = 1)$ (C)	Q_{exp} (C)	n
0.0181	3.24	31.27	68.01	2.17
0.0276	4.49	47.68	99.1	2.07
0.0297	5.32	51.31	109.1	2.12
0.0273	4.89	47.16	96.25	2.04
0.0264	4.73	45.61	90.64	1.99
0.0292	5.23	50.45	108.7	2.15
0.0252	4.51	43.54	91.28	2.09
0.0276	4.94	47.68	88.75	1.86
0.0828	1.48	143.1	300.0	2.09

avg: 2.1 ± 0.2

of iron(II) in 60.0-40.0 m/o melt at 25 °C are shown in Figures 4.1 to 4.4 respectively. The stationary electrode voltammograms recorded at platinum, tungsten, and gold are very similar; therefore, only the results for platinum (Figure 4.1a) will be described in detail. This voltammogram exhibits a broad reduction wave with $E_p^c = 0.34$ V on the forward scan. The reverse scan exhibits an oxidation wave with $E_p^a = 0.70$ V. These reduction and oxidation waves are attributed to the reduction of iron(II) solvated by the melt to iron metal and to the oxidation of the iron surface deposit to freely diffusing iron(II), respectively.



Some typical data resulting from a series of voltammetric experiments at different scan rates are given in Table 4.2. Examination of the data in this table reveals that E_p^c shifts cathodically and that $i_p^c/v^{1/2}$ decreases as the scan rate is increased. For a reversible electrode reaction involving the deposition of an insoluble substance, $|E_p^c - E_{p/2}|$ should have a value of $0.77RT/nF$ or $0.0199/n$ V at 25 °C (63). However, $|E_p^c - E_{p/2}|$ in Table 4.2 clearly exceeds the value of 0.0100 V expected for the reaction given in Equation 4.1, even at the slowest scan rate. These results indicate that the iron electrode reaction is quasi-reversible at platinum. Additionally, experiments at different scan rates were carried out at gold, tungsten, and glassy carbon and gave analogous results. Similar quasi-reversible behavior was found for the Ag(I)/Ag (19) and Sn(II)/Sn (29) electrode reactions at platinum in acidic AlCl_3 -MeEtimCl melt.

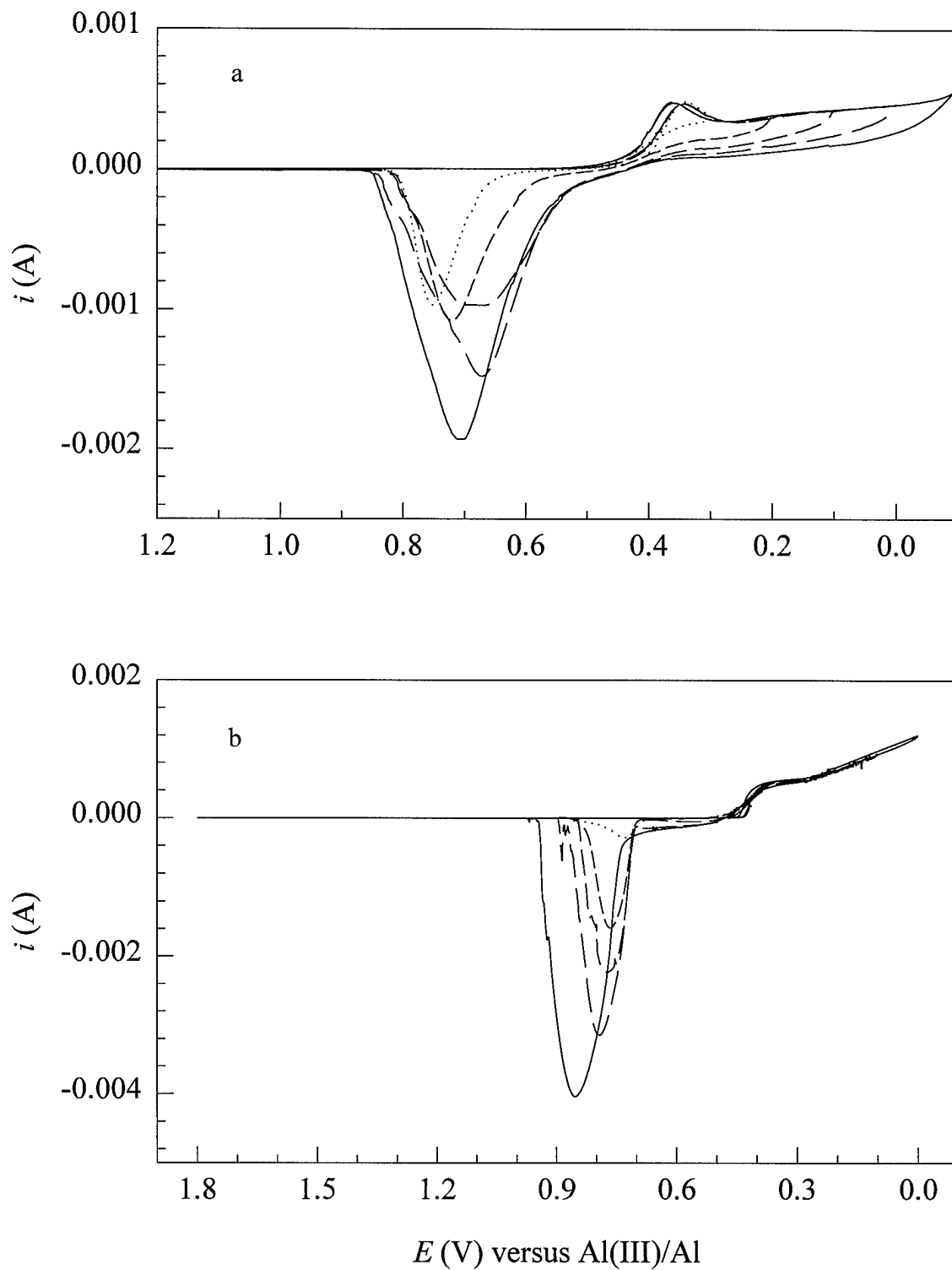


Figure 4.1 Voltammograms recorded at a platinum electrode in a 0.050 M solution of Fe(II) in 60.0-40.0 m/o AlCl₃-MeEtimCl at 25°C: (a) stationary electrode (scan rate = 0.050 V s⁻¹) and (b) RDE (rotation rate = 104.7 s⁻¹).

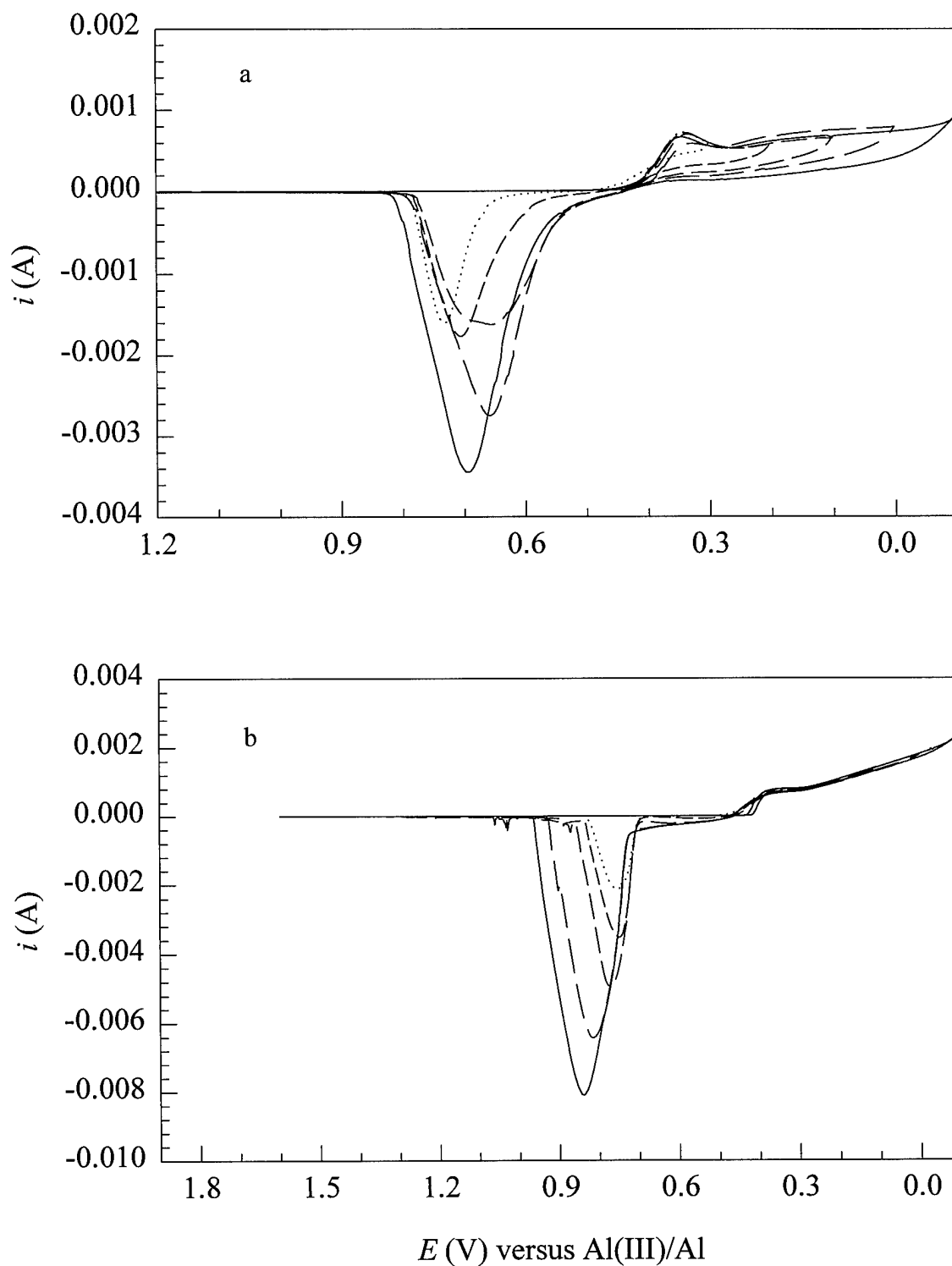


Figure 4.2 Voltammograms recorded at a tungsten electrode in a 0.050 M solution of Fe(II) in 60.0-40.0 m/o AlCl_3 -MeEtimCl at 25 °C: (a) stationary electrode (scan rate = 0.050 V s^{-1}) and (b) RDE (rotation rate = 104.7 s^{-1}).

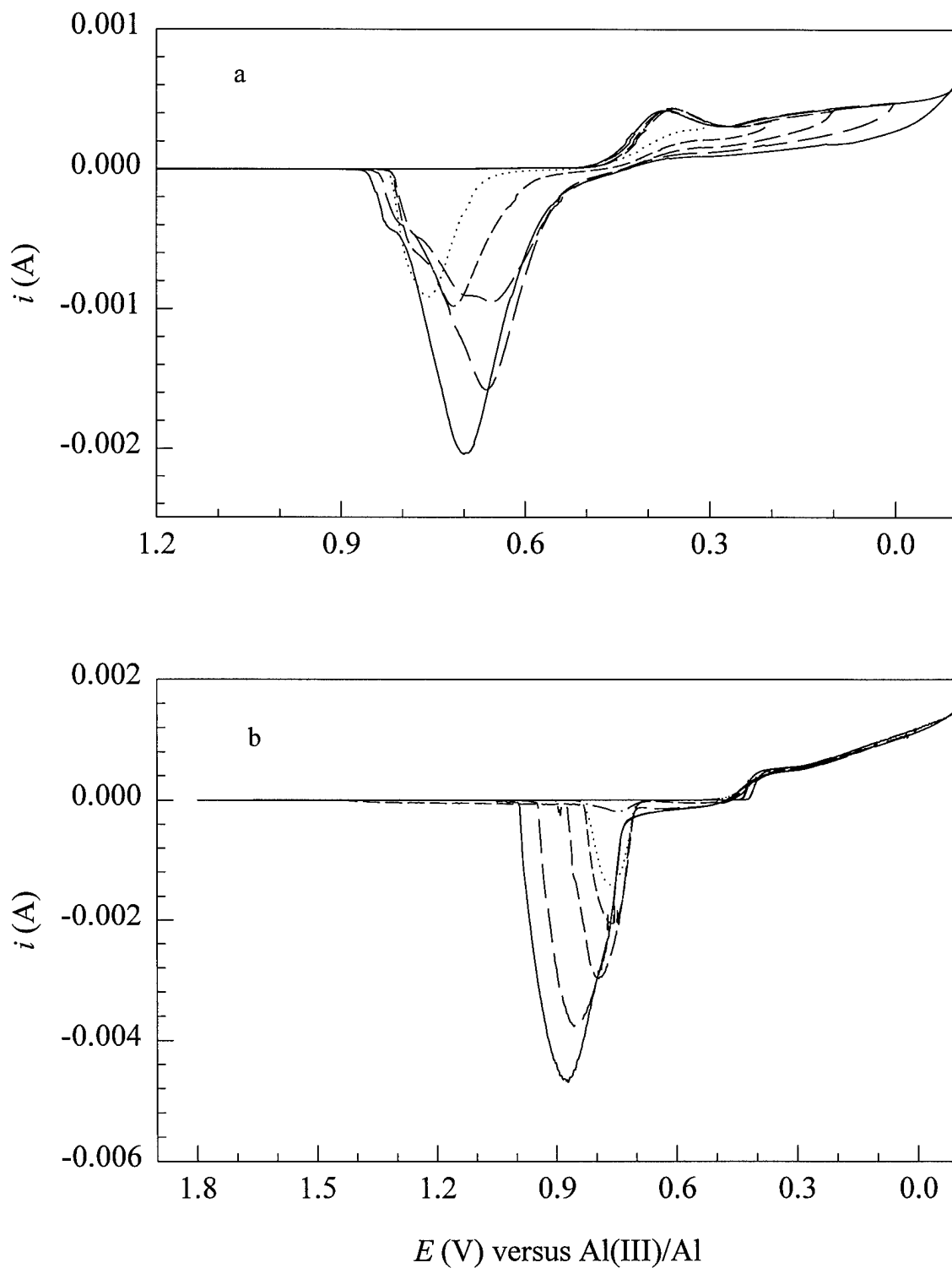
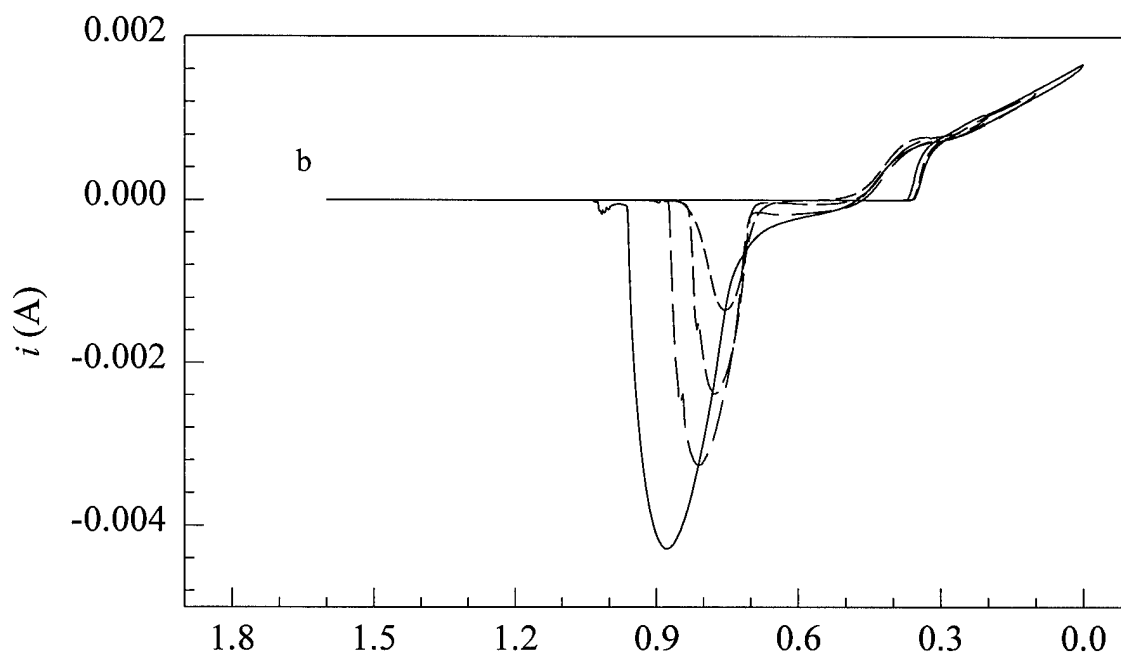
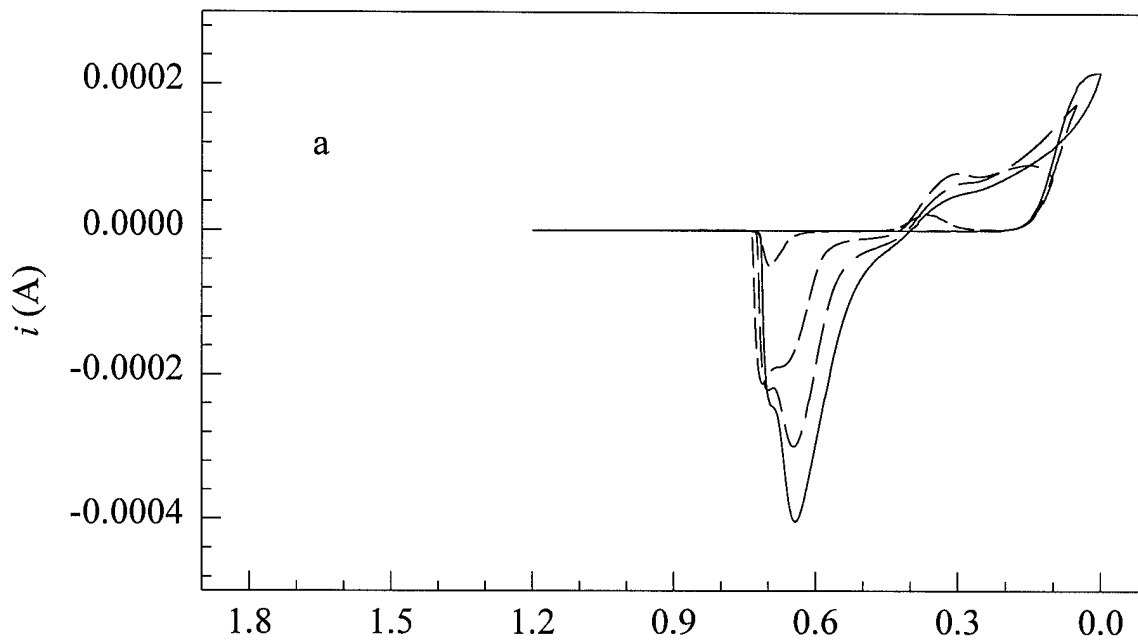


Figure 4.3 Voltammograms recorded at a gold electrode in a 0.050 M solution of Fe(II) in 60.0-40.0 m/o AlCl_3 -MeEtimCl at 25 °C: (a) stationary electrode (scan rate = 0.050 Vs^{-1}) and (b) RDE (rotation rate = 104.7 s^{-1}).



E (V) versus Al(III)/Al

Figure 4.4 Voltammograms recorded at a glassy carbon electrode in a 0.050 M solution of Fe(II) in 60.0-40.0 m/o AlCl₃-MeEtimCl at 25 °C: (a) stationary electrode (scan rate = 0.050 V s⁻¹) and (b) RDE (rotation rate = 104.7 s⁻¹).

Table 4.2. Cyclic voltammetric data for the reduction of Fe(II) at tungsten ($A = 0.196 \text{ cm}^2$), platinum ($A = 0.126 \text{ cm}^2$), and gold ($A = 0.126 \text{ cm}^2$) electrodes.

v (V s^{-1})	$10^4 i_p^c$ (A)	$10^3 i_p^c / v^{1/2}$ ($\text{A s}^{1/2} \text{ V}^{-1/2}$)	E_p^c (V)	E_p^a (V)	$ E_p^c - E_{p/2} $ (V)
platinum electrode					
0.010	2.96	2.96	0.406	0.618	0.023
0.030	4.54	2.62	0.374	0.649	0.051
0.050	4.75	2.12	0.358	0.672	0.068
0.070	5.18	1.93	0.336	0.689	0.139
0.090	5.06	1.69	0.322	0.704	0.131
gold electrode					
0.010	2.30	2.3	0.424	0.616	0.045
0.030	3.69	2.13	0.396	0.647	0.049
0.050	4.21	1.85	0.368	0.664	0.060
0.070	4.95	1.87	0.362	0.682	0.065
0.090	5.25	1.75	0.354	0.696	0.061
tungsten electrode					
0.010	4.00	4.00	0.414	0.614	0.027
0.030	6.26	3.61	0.380	0.639	0.040
0.050	7.26	3.25	0.362	0.658	0.044
0.070	7.76	2.93	0.346	0.676	0.049
0.090	7.91	2.64	0.330	0.684	0.057

Figure 4.1b illustrates a typical RDE voltammogram for the deposition and stripping of iron at the same polycrystalline platinum electrode that was used to acquire the stationary electrode voltammograms. A limiting current is evident as the electrode potential is scanned below 0.35 V, and a prominent, symmetrical oxidation wave is observed on the reverse scan at $E_p^a = 0.85$ V. If E_λ is made more negative than 0 V, which is the thermodynamic reversible potential for the Al(III)/Al couple in this melt, then another reduction and associated oxidation wave due to the bulk deposition and stripping of aluminum, respectively is observed. RDE voltammograms for the electrodeposition and stripping of bulk iron at a polycrystalline tungsten and gold are shown in Figures 4.2 and 4.3, respectively. The major features of these voltammograms are similar to those appearing in the voltammograms recorded at platinum, i.e., a limiting reduction current between 0.25 and 0.35 V on the forward scan and a large symmetrical bulk stripping wave on the reverse scan at approximately the same potential as that observed at platinum. However, there is an increase in the current beyond the limiting current as the electrode potential is scanned below 0.30 V. This could be due to an increase in the electrode surface area due to the formation of dendritic deposits or to the co-deposition of aluminum with iron.

The RDE voltammograms for the electrodeposition of iron on platinum, tungsten, and gold all exhibit well-defined limiting current plateaus. Plots of the limiting currents versus the square root of the rotation rate were linear and passed through the origin as seen in Figure 4.5. This is indicative of convective diffusion controlled reactions within the limiting current potential region. This allows determination of the diffusion coefficient of Fe(II) by application of the Levich equation. The average value of $D_{\text{Fe(II)}}$ and $D_{\text{Fe(II)}}\eta/T$ for iron(II)

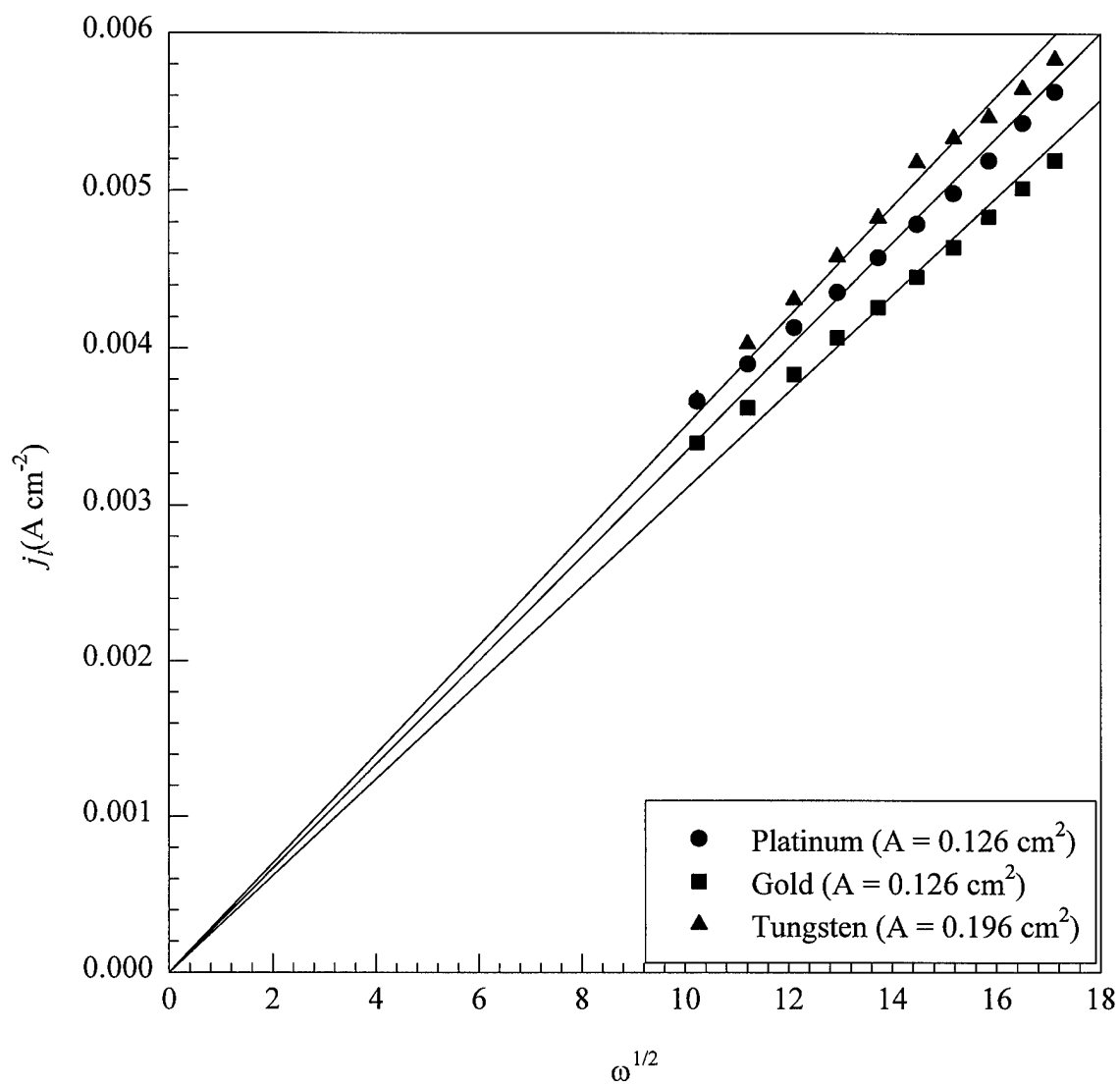


Figure 4.5 Levich plot for the reduction of Fe(II) in 60.0-40.0 m/o melt at 25 °C.

in the 60.0-40.0 m/o AlCl_3 -MeEtimCl melt at 25 °C were calculated from the limiting currents of the four voltammograms in Figures 4.1 to 4.4. The resulting values are $(2.6 \pm 0.3) \times 10^{-6} \text{ cm}^2 \text{ s}^{-1}$ and $1.39 \times 10^{-9} \text{ g cm s}^{-2} \text{ K}^{-1}$, respectively.

4.3 Sampled-current voltammetry of iron(II)

Sampled-current voltammograms are used to determine the partial currents for the depositing metal and any co-depositing aluminum if present, and thus the alloy composition as a function of potential. Sampled-current voltammograms were constructed from the chronoamperometric current-time transients resulting from experiments at each electrode in an unstirred solution containing electrogenerated iron(II). In these experiments, the potential was stepped from an initial value of 1.50 V, where no Faradaic process occurs, to potentials ranging from 0 to 0.80 V; the solution was stirred before the application of each potential pulse to assure a uniform solution and then allowed to rest for 60 seconds prior to the pulse. In order to insure a reproducible response, the electrode surface was cleaned by stepping the rotating electrode to 1.80 V for 60 seconds before each potential step experiment. The current was then sampled at the same elapsed time for each current-time transient and plotted as a function of potential. The sampled-current voltammograms that resulted from these experiments are shown in Figure 4.6. Like the RDE voltammograms, these sampled-current voltammograms exhibit well defined limiting currents and a linear increase in current prior to 0 V. Based on similar behavior observed for both cobalt (37) and nickel (40), it can be concluded from these waves that the co-deposition of aluminum occurs during the electrodeposition of iron and prior to the bulk deposition of aluminum.

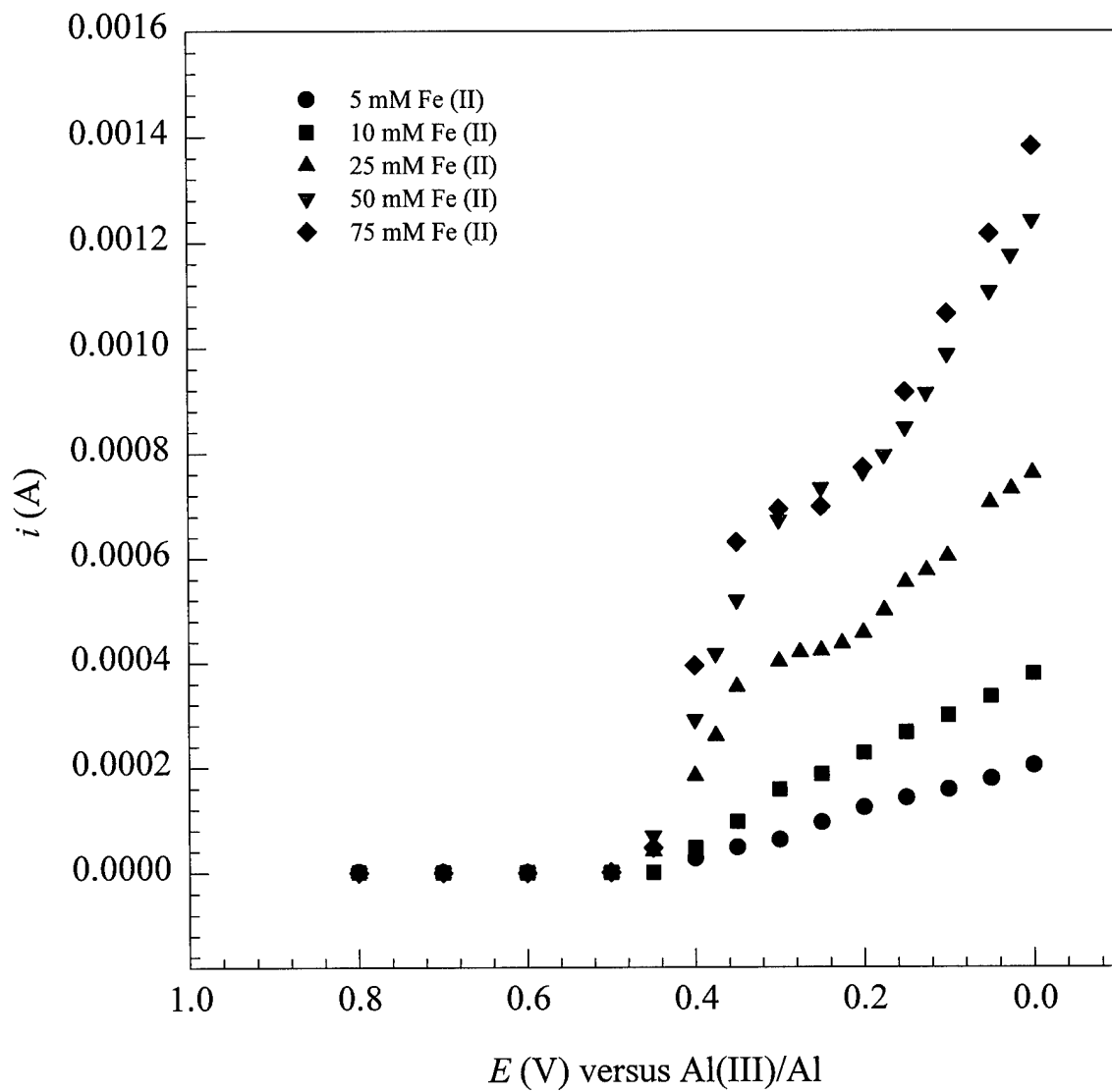
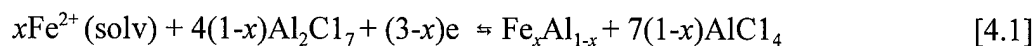


Figure 4.6 Sampled-current voltammograms for the reduction of Fe(II) in 60.0-40.0 m/o melt at 25 °C.

The co-deposition of aluminum with iron can be represented by the following equation:



where x and $1-x$ represent the mole fraction of Fe and Al in the Fe-Al alloy, *i.e.*, $\text{Fe}_x\text{Al}_{1-x}$. The value of the $1-x$ was estimated from each of the Pt-RDE sampled-current voltammograms in Figure 4.6 and calculated from the following equation:

$$1-x = 1/(1 + 1.5 i_l)/(i_{\text{total}} - i_l) \quad [4.2]$$

where i_{total} is the total current and i_l is the limiting current. Plots of $1-x$ versus potential that resulted from these calculations are presented in Figure 4.7. These graphs show that $1-x$ is dependent upon the applied potential, but there is no clear dependence of $1-x$ on the iron(II) concentration.

4.4 Analysis of iron-aluminum thin films by anodic linear sweep voltammetry

The composition of Fe-Al alloy electrodeposits was examined by carrying out RRDE-ALSV experiments similar to those described for Co-Al alloys. By setting E_r to 0.35 V, it was possible to reduce the iron(II) produced during the anodic dissolution of Fe-Al alloy at the ring, permitting identification of those alloy stripping waves that have a current component arising from the oxidation of iron. However, before this method could be

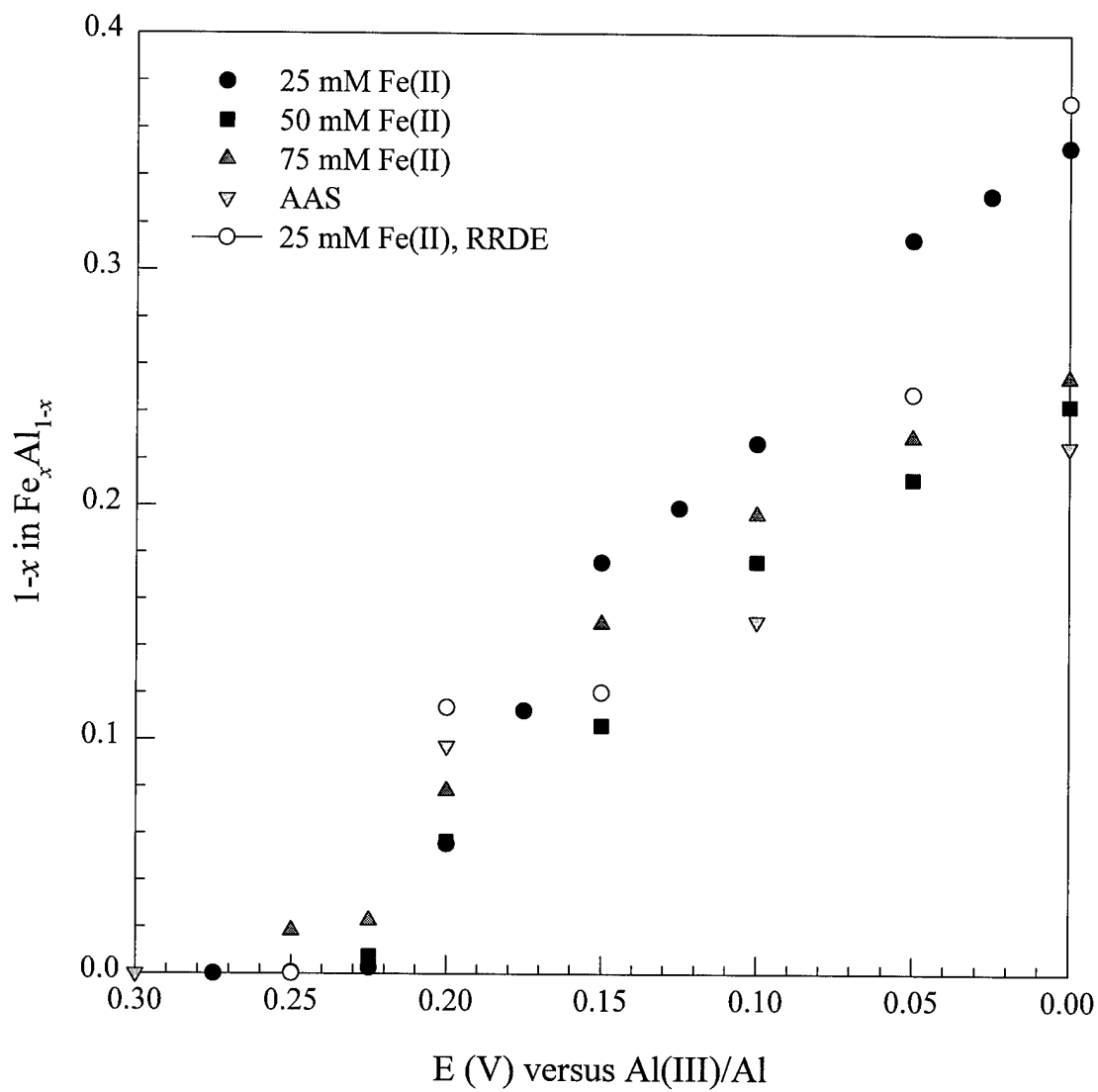


Figure 4.7 Composition of $\text{Fe}_x\text{Al}_{1-x}$ as a function of potential.

employed, N_{exp} was determined by electrodepositing iron metal on the disk electrode at a potential of 0.35 V in a solution of iron(II) with the ring electrode inactive. The iron was then anodically dissolved from the disk in pure melt while the ring was held at 0.25 V. These experiments yielded a value of $N_{\text{exp}} = 0.176$; this is in reasonable agreement with the theoretical collection efficiency of 0.220 for this ring-disk electrode, which was calculated from, r_1 , r_2 , and r_3 , respectively (63).

In view of these results, a series of ALSV experiments were carried out at the Pt-RRDE over the range of deposition potentials where the formation of Fe-Al alloy is expected, *i.e.*, from 0.25 to 0 V. In these experiments, 425 mC cm⁻² electrodeposits were produced on the disk electrode from a 0.025 M solution of iron(II). Once the deposit was made, the electrode was then transferred to pure melt, and the Fe-Al electrodeposit was oxidized from the disk by slow scan (0.002 V s⁻¹) ALSV while the ring was held at 0.25 V. The time spent in the plating solution was kept to less than 15 seconds. The reason for this is that a plot of the alloy composition versus the immersion time of the deposit in the plating solution reveals that the deposit composition is highly sensitive to the time the deposit remains in the plating bath. During a previous study of Ni-Al alloy, the deposit composition was found to depend on the charge density used to prepare the electrodeposit (83). This phenomenon is believed to arise from the thermodynamic instability of aluminum in the alloy when immersed in solutions of nickel(II). The Fe-Al alloy was found to display similar instability in iron(II) solutions, and a minimum charge density of ca. 325 mC cm⁻² was needed in order to obtain Fe-Al deposits of constant composition.

Typical voltammograms illustrating the disk and corrected ring currents that resulted from several of these experiments are shown in Figures 4.8 and 4.9. For deposits produced at 0.20 V, the major feature of the disk voltammogram was a wave with $E_p^a = 0.70$ V. The large ring current that was observed as the disk potential was scanned through this stripping wave indicates that a major component of the current arises from the oxidation of iron in the deposit. However, the charge corresponding to this wave was slightly larger than the corrected ring charge, Q_r/N_{exp} , indicating that some of the current must be due to the oxidation of aluminum. For the deposit prepared at 0.15 V, the disk voltammogram (Figure 4.8) revealed oxidation waves with $E_p^a = 0.72$ and 0.44 V, respectively. A ring current was associated with the former, but not the later, indicating that the wave at 0.44 V must arise from the selective removal of aluminum from the alloy. The disk voltammograms corresponding to the 0.05 and 0 V deposits (Figure 4.9) were similar in appearance to that of the 0.15 V deposit, except that the aluminum wave was shifted to $E_p^a = 0.46$ V in the case of the 0.05 V deposit. The disk voltammogram for the 0 V deposit gave waves with $E_p^a = 0.72$ and 0.48 V due to the oxidation of aluminum and iron, respectively from the deposit. A small amount of aluminum was also oxidized from each of these deposits at potentials proximate to the oxidation of iron.

These slight shifts in the position of the aluminum stripping wave indicate that the activity of aluminum in the alloy is changing with the aluminum content of the alloy. However, it is unclear why aluminum dissolution occurs at two different potentials. Assuming that the deposit is in two phases and that the second dissolution is due to aluminum

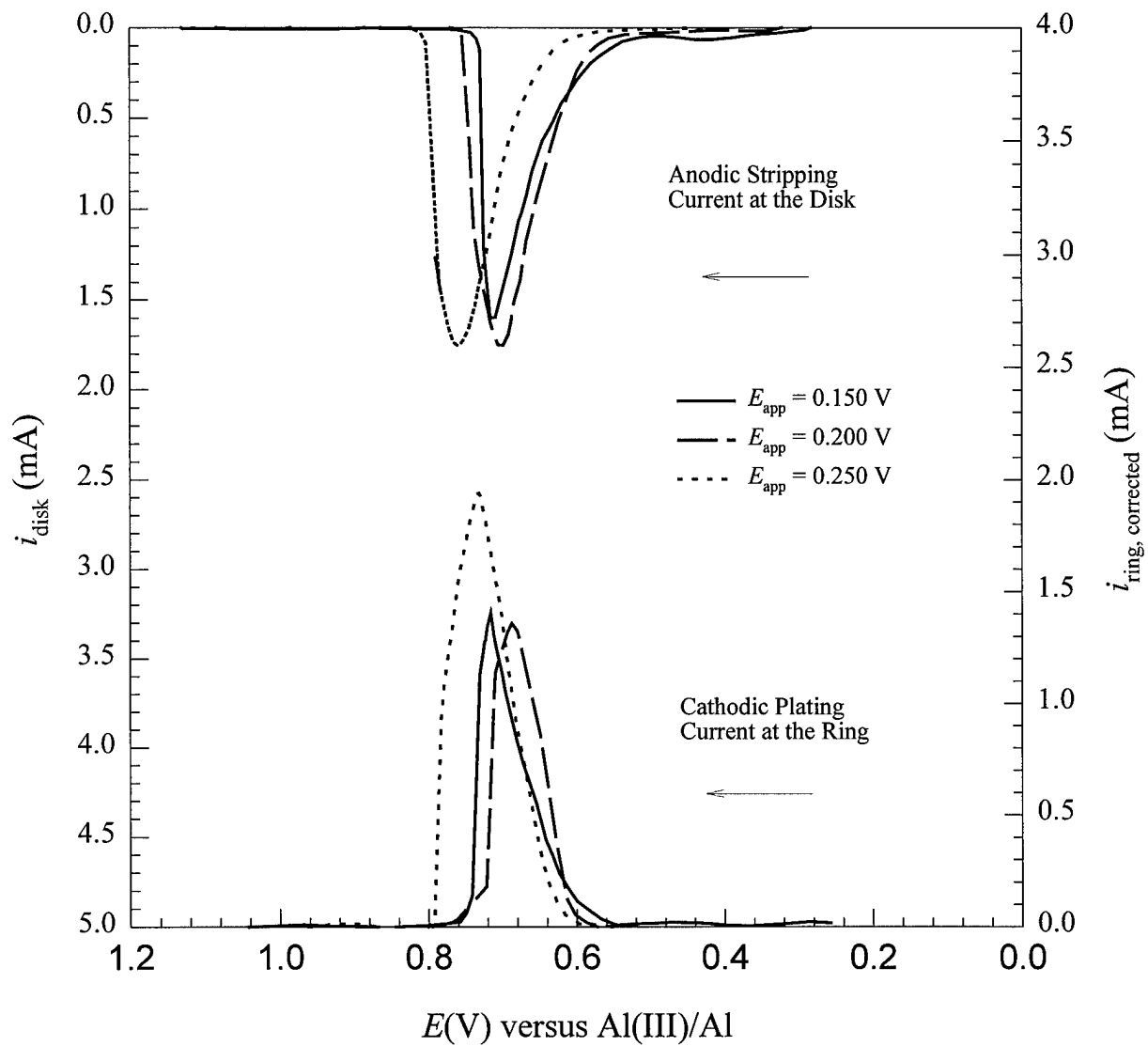


Figure 4.8 Disk and ring voltammograms for the oxidation of thin layer Fe-Al electrodeposits from a Pt-RRDE.

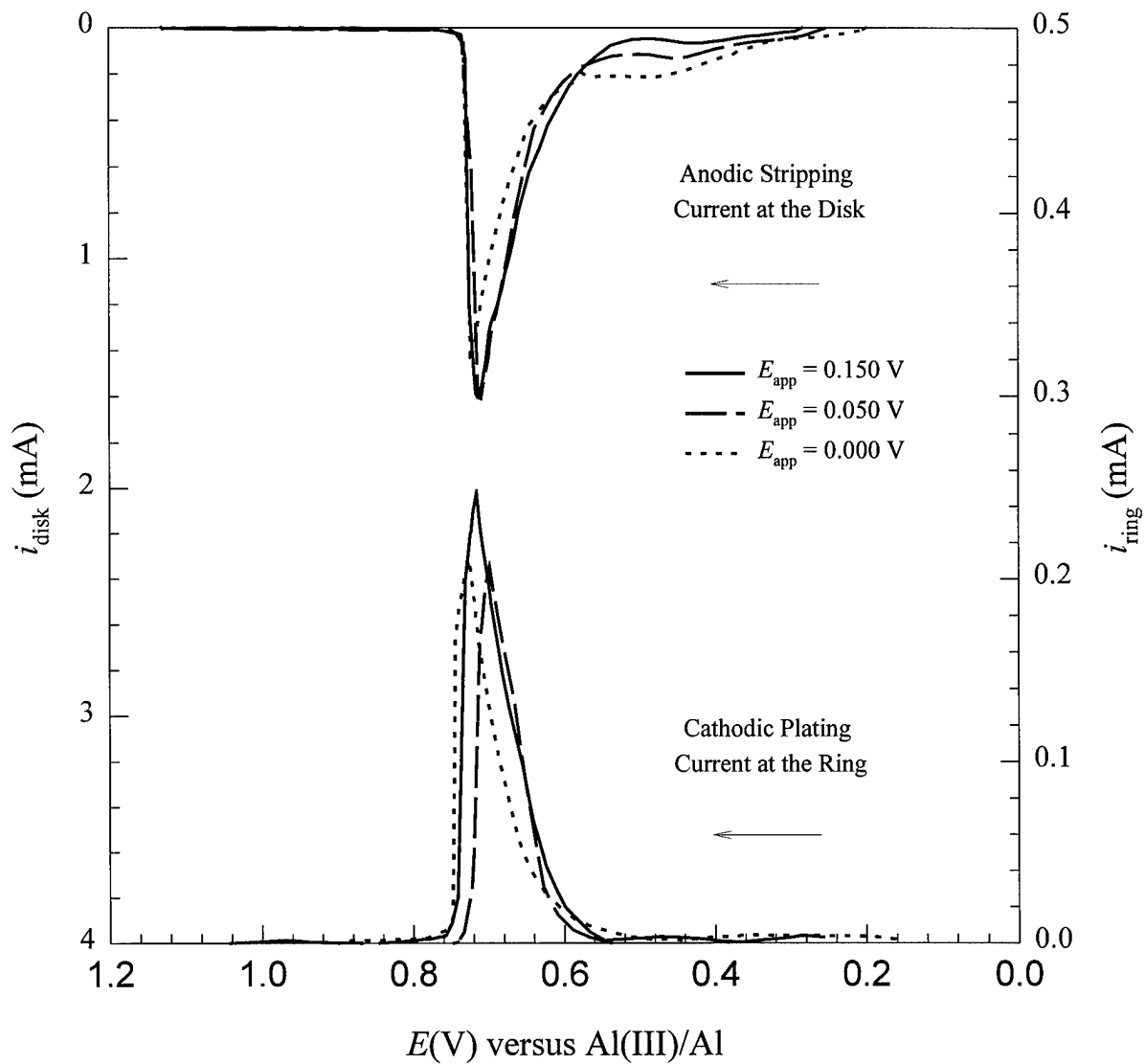


Figure 4.9 Disk and ring voltammograms for the oxidation of thin layer Fe-Al electrodeposits from a Pt-RRDE.

contained in a iron-rich phase, then the two phases cannot be in equilibrium because the aluminum activity is obviously different in each phase. Alternatively, the aluminum associated with the second dissolution process may simply be inaccessible to oxidation or "hidden" beneath the iron and can not be oxidized until some dissolution of the iron deposit occurs. The negative shift in the iron stripping wave that is associated with alloyed deposits may then be due to the more favorable dissolution kinetics of a porous iron layer over that of a pure, compact deposit (79). The characteristics of anodic linear sweep voltammograms for the dissolution of an alloy deposit are very sensitive to the composition and structure of the deposit. Theoretical and experimental studies have attempted to correlate wave shape and location on the potential scale with the type of alloy that is produced (79, 80). However, a detailed analysis of the voltammograms in Figures 4.8 and 4.9 beyond that given here would be purely speculative without reliable information about the phase distribution in the alloy. The alloy composition (1-x) as a function of deposition potential was calculated from N_{exp} and the values of Q_r and Q_d that resulted from numerous experiments similar to those described above by using the following expression:

$$1 - x = 1 / \{1 + 1.5 [Q_r / (N_{\text{exp}} Q_d - Q_r)]\} \quad [4.3]$$

The resulting values of 1 - x are plotted as a function of potential in Figure 4.7, and they are in reasonable agreement with the values of 1 - x derived from the sampled-current voltammetry experiments carried out in a 0.025 M iron(II) solution.

4.5 Underpotential deposition of aluminum on iron

In order for an iron-aluminum alloy to form at potentials more positive than the equilibrium potential of the Al(III)/Al couple, there must be a free energy advantage gained through alloy formation. To demonstrate that the UPD of aluminum can occur on an iron surface, cyclic voltammetric experiments were conducted at a polycrystalline iron electrode in blank 60.0-40.0 m/o melt. The iron working electrode was slowly scanned between 0.60 and 0.10 V. The only species available for reduction in pure melt at these potentials is Al_2Cl_7^- . Figure 4.10 shows the voltammogram recorded under those conditions. This voltammogram is characterized by a reduction wave on the forward scan with $E_p^c = 0.22$ V and a well defined stripping wave on the reverse scan with $E_p^a = 0.40$ V. The charges corresponding to these reduction and oxidation waves correspond to the deposition and stripping of a single monolayer. Thus, the UPD of aluminum onto iron demonstrates that there indeed is an energetic driving force for the underpotential alloying of aluminum with iron. This indicates that aluminum may co-deposit with iron at potentials positive of 0 V. These results are consistent with those reported in the previous section.

4.6 Nucleation of iron on glassy carbon

Stationary and RDE voltammograms for the electrodeposition and stripping of iron at a glassy carbon electrode are shown in Figure 4.4. The current loops seen in both voltammograms after reversal of the forward scan are typical of those associated with an overpotential-driven nucleation process. These current loops occur because the deposition of iron on glassy carbon during the forward scan requires an overpotential in order to initiate

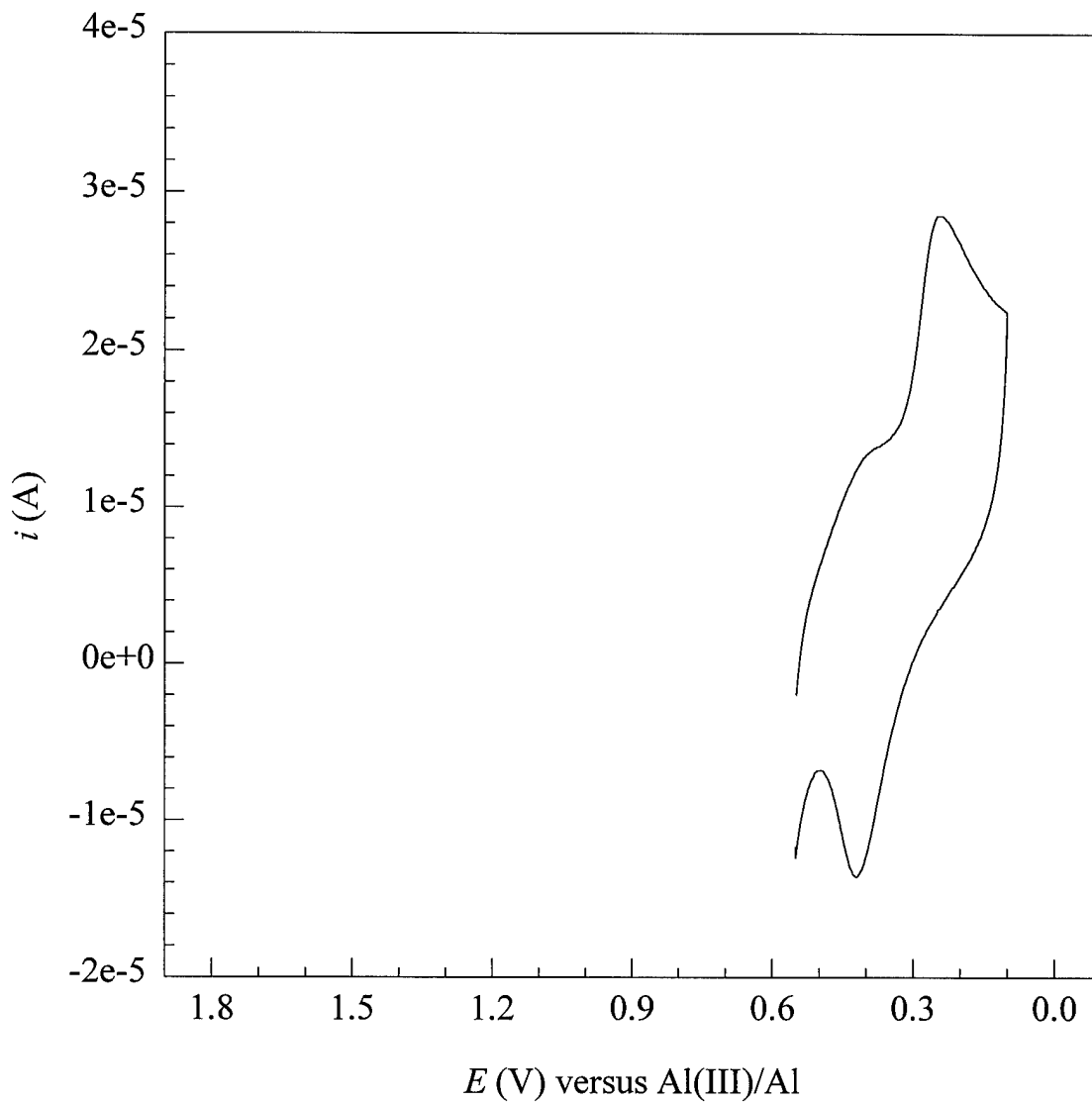


Figure 4.10 Underpotential deposition of aluminum onto an iron working electrode. This cyclic voltammogram was acquired in pure 60.0-40.0 m/o melt.

the nucleation and subsequent growth of an iron deposit; after the scan is reversed, the reduction of iron continues at more positive potentials because iron is deposited on an iron surface rather than on the hostile glassy carbon surface.

In view of the nucleation phenomena seen during the voltammetry of iron(II) at glassy carbon (Figure 4.4), chronoamperometry experiments were conducted in order to determine the nucleation mechanism. The current-time transients resulting from these experiments are shown in Figure 4.11a. The dimensionless current-time transients are compared to the limiting theoretical transients for instantaneous and progressive three dimensional nucleation with hemispherical growth of the nuclei in Figure 4.11b. The experimental transients are in excellent agreement with the limiting model for progressive nucleation. This result is consistent with the linear plots of $(i/i_M)^{2/3}$ versus t that were constructed from data taken from the rising portions of the experimental current-time transients in Figure 4.11. Therefore, the intercepts of these plots were used to obtain estimates of t_o , and the resulting values of t_o are shown in Table 4.3 along with the product $i_M^2 t_M'$. The growth process is considered to be diffusion controlled, *i.e.*, $C_{\text{Fe(II)}}(x=0) \approx 0$, if $i_M^2 t_M'$ does not vary with η (79); the data in Table 4.3 indicate that this is the case. In addition, the overpotentials that were applied during each chronoamperometry experiment correspond to the limiting currents in Figure 4.4.

The kinetics of the nucleation process are conveniently characterized by A_i (s^{-1}) and N_o (cm^{-2}). However, for the limiting case of progressive nucleation, the ratio $A_i/N_o \rightarrow 0$ (60). In this case, A_i and N_o can not be determined separately, and the nucleation kinetics must be analyzed in terms of the steady-state nucleation rate, $A_i N_o$. The results of this calculation are

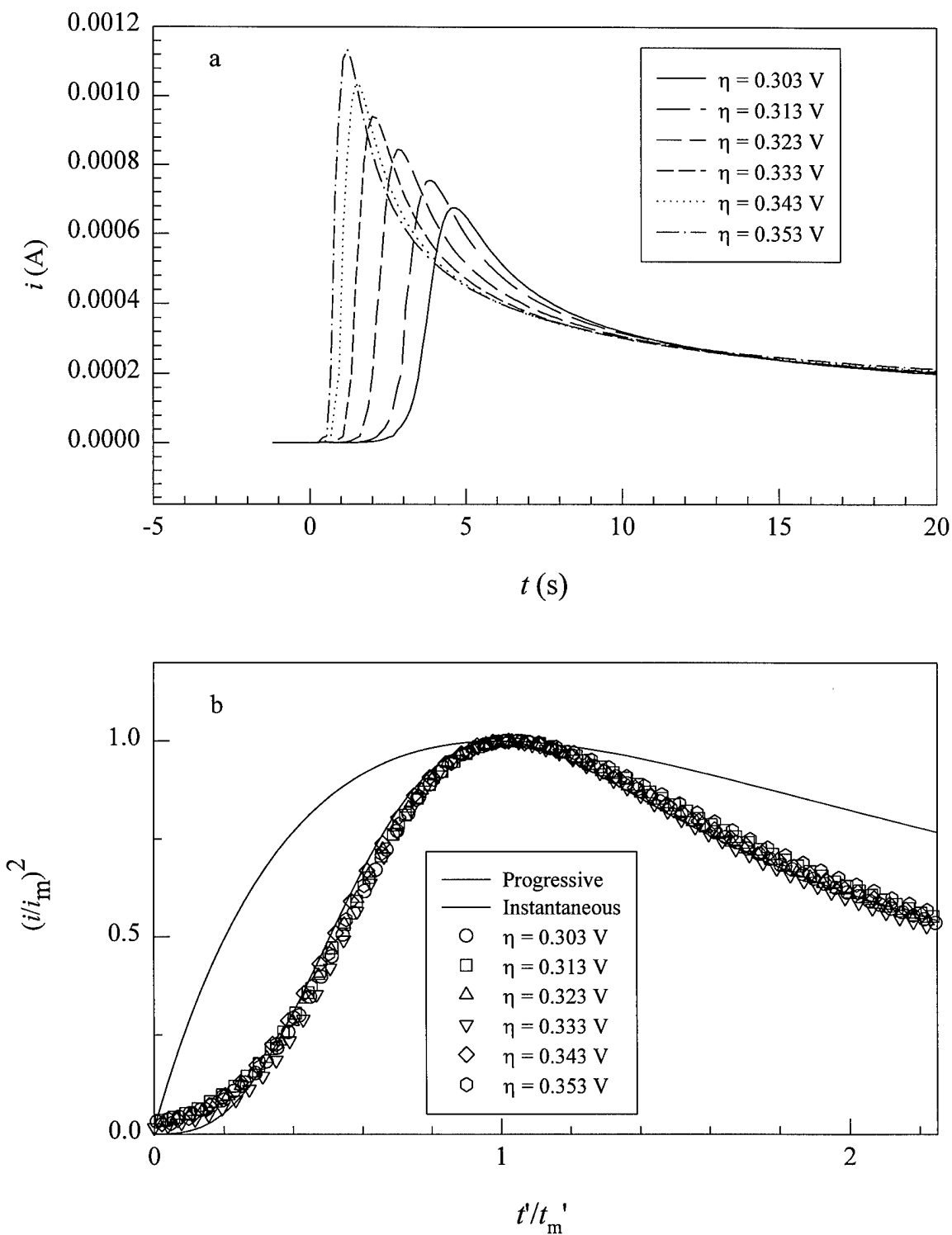


Figure 4.11 (a) Current-time transients for the reduction of Fe(II) at glassy carbon in 60.0-40.0 m/o melt. (b) Comparison of the experimental dimensionless current-time transients to the models for 3-D hemispherical diffusion-controlled growth.

Table 4.3. Nucleation data for the electrodeposition of iron on glassy carbon

η^a (V)	$10^4 i_m$ (A)	t_m (s)	t_0 (s)	$10^6 i_m^2 t_m'$ (A ² s)	$10^5 A_t N_0$ (s ⁻¹ cm ²)	$10^{-5} N_s$ (cm ²)
0.303	6.47	12.32	8.5	1.60	4.70	8.50
0.313	6.84	11.52	8.1	1.60	5.86	9.49
0.323	7.28	10.23	7.0	1.71	6.14	9.72
0.333	7.73	9.09	6.0	1.85	6.22	9.78
0.343	8.18	7.75	5.1	1.77	8.81	11.6
0.353	8.62	6.58	4.2	1.77	8.40	11.4

^a $E_{eq} = 0.483$ V

collected in Table 4.3 along with values of N_s , which were calculated from $A_t N_0$ using to Equation 1.23 (57).

According to the atomistic theory of nucleation, the slope of a plot of $\log(A_t N_0)$ versus η gives information about the critical number of atoms required for the formation of a stable nucleus, n_c (37). A plot of $\log(A_t N_0)$ versus η that was constructed from the data in Table 4.3 is shown in Figure 4.12. This plot is linear with a slope of $11.50 \text{ s}^{-1} \text{ cm}^{-2} \text{ V}^{-1}$ and a correlation coefficient of 0.961. n_c is related to this slope by Equation 1.24 (68). If α is assumed to have a value of 0.50, then Equation 1.18 gives $n_c \approx 0$. This indicates that active sites on the electrode surface probably act as the critical nucleus (69) during the electrodeposition of iron on glassy carbon in acidic AlCl_3 -MeEtimCl. Values of n_c ranging from 0 to 1 were reported for the electrodeposition of cadmium (70), copper (71), lead (72,73), and silver (74,75) on glassy carbon from aqueous solutions.

4.7 Bulk deposition experiments

In order to determine whether bulk deposits prepared at the same potentials as the thin-layer deposits mirror the composition of the latter, a series of experiments was performed to establish the aluminum content of bulk deposits made over a range of potentials. These experiments were carried out in a cell with an iron anode placed in the bulk solution. As iron(II) is reduced at a copper cathode, it is replaced in solution by dissolution of the iron anode. If the charge passed during the deposition process is applied solely toward the deposition of iron, then the iron(II) concentration in the solution should not change.

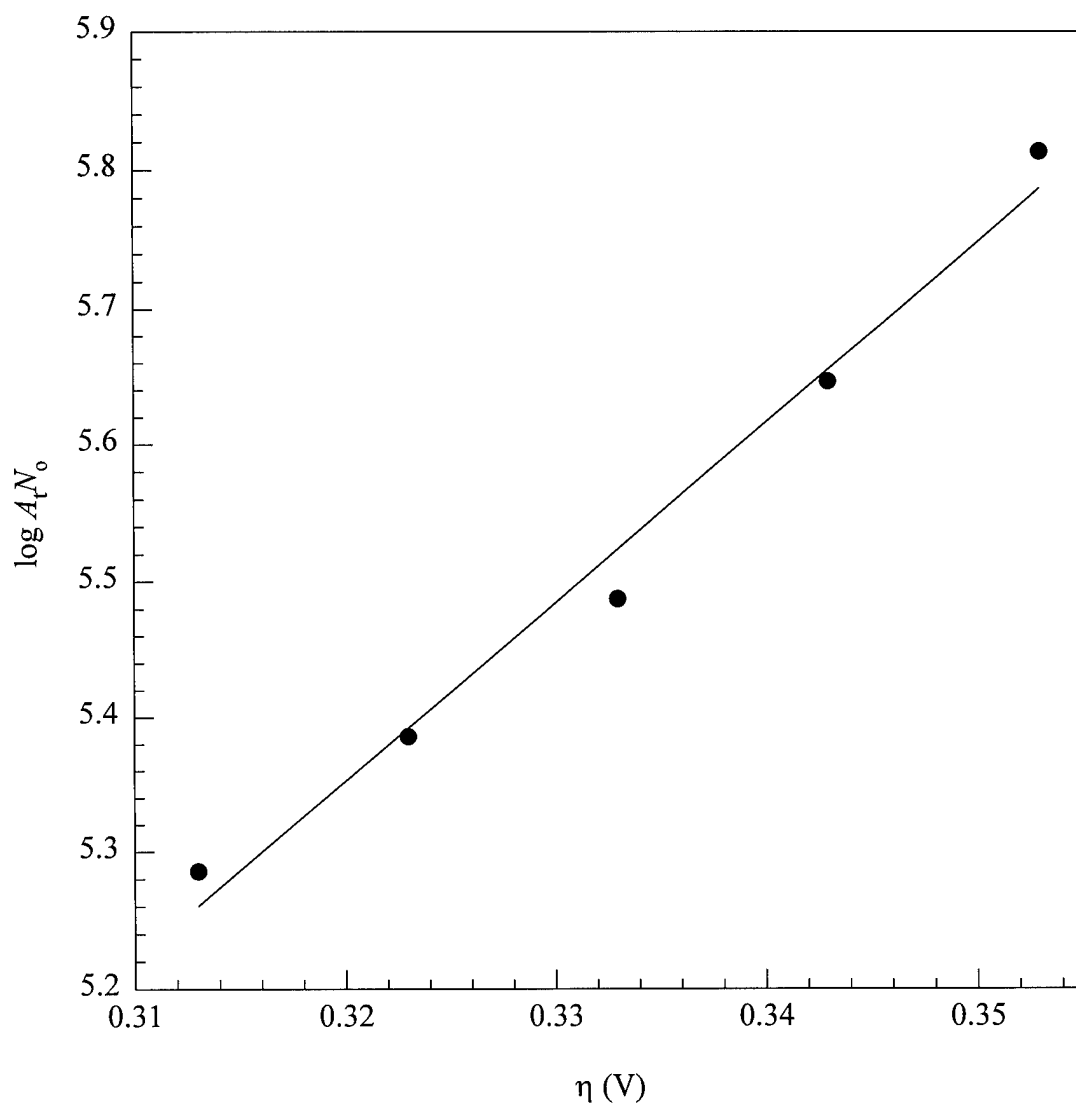


Figure 4.12 Plot of $\log A_t N_0$ versus the overpotential.

However, at potentials negative of 0.25 V, aluminum co-deposits with iron. In order for aluminum to co-deposit, some of the current that flows in the cell must be due to the reduction of Al_2Cl_7^- . However, dissolution of the iron electrode still takes place at the rate defined by the total current. Thus, the net result of the co-deposition of aluminum will be an increase in the iron(II) concentration in the solution used to carry out the experiment. The charge equivalent to the excess iron(II) concentration is directly proportional the amount of aluminum co-deposited with the iron.

In these experiments, a stock solution of 0.050 M iron(II) in 60.0-40.0 m/o melt was used to make deposits at $E_{\text{app}} = 0.30, 0.20, 0.10, 0$ and -0.10 V. Careful attention was directed to the amount of iron(II) solution used in each experiment and to the current passed to produce each deposit. Once the experiment was completed, the iron deposit was removed from the melt while still under cathodic protection to ensure that aluminum in the deposit was not reduced by the iron(II) in the plating bath, decreasing the concentration of the latter. A sample of the electrolysis melt was taken and analyzed for its iron content with AAS. The results of these experiments are given in Figure 4.7, and they are in good agreement with those from the sampled-current voltammetry experiments.

4.8 Characterization of bulk iron deposits by SEM-EDS

Bulk deposits for SEM-EDS analysis were prepared by two methods. The first used a 1 mm diameter fixed copper wire substrate and the second involved deposition on a rotating copper disk electrode. It was hoped that rotation of the electrode would lead to a better quality and more adherent deposit. The plating bath, which contained 0.025 M iron(II), was

gently stirred with a Teflon-coated stir bar during electrodeposition experiments. Following each experiment, the deposits were immediately taken from the plating bath while under cathodic protection and washed with dry benzene to remove any bath residue. They were then removed from the glove box and washed in succession with ethanol, acetone, and water.

Deposits were prepared on copper wire substrates at a charge density of approximately 50 C cm^{-2} at $E_{\text{app}} = 0.35, 0.25, 0.20, 0.10, 0$ and -0.05 V . Figures 4.13 and 4.14 show SEM pictures of constant potential deposits prepared at 0 and 0.35 V respectively. Deposits prepared at constant potentials contained only trace amounts of aluminum and were contaminated with chloride from the melt. As expected, no aluminum was found in deposits prepared at 0.35 V . This deposit was also free of chloride, indicating minimal melt contamination (Figure 4.13). Deposits prepared at $E_{\text{app}} = 0.20, 0.10$ and 0 V were too badly contaminated with melt to permit the accurate determination of their aluminum content. Deposits were also made at constant current on a rotating copper disk substrate with an approximate charge density of 50 C cm^{-2} (Figures 4.15 and 4.16). The electrodes were rotated at 1500 rpm during the deposition process. The result was a much more adherent deposit with a much smoother surface. In addition, those deposits were more metallic in appearance than those deposited on copper wire. However, within 24 hours after exposure to the atmosphere, these deposits also detached from the electrode surface as a result of the hydrolysis of entrapped melt. Current densities ranging from 15.1 to 60.3 mA cm^{-2} were also used to prepare deposits. All of these currents resulted in negative potentials that ranged from -0.05 to -0.49 V respectively. EDS analysis indicated that these deposits contained

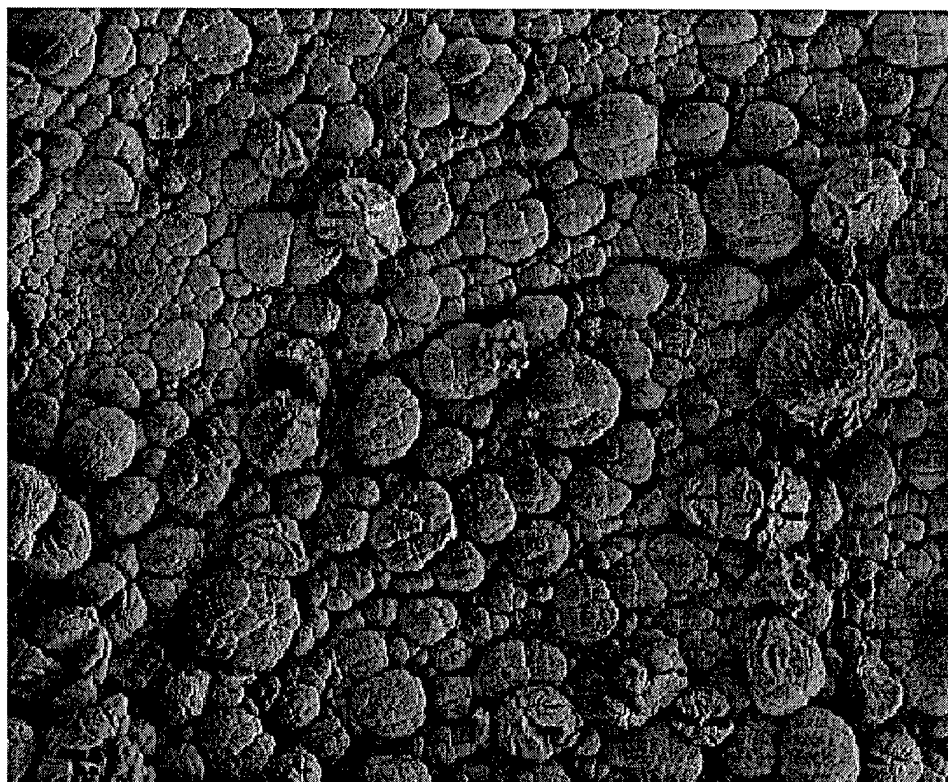


Figure 4.13 SEM secondary image of an iron electrodeposit. This deposit was prepared on a fixed copper wire from a 0.025 M solution of iron(II) in 60.0-40.0 m/o melt at $E_{app} = 0V$.

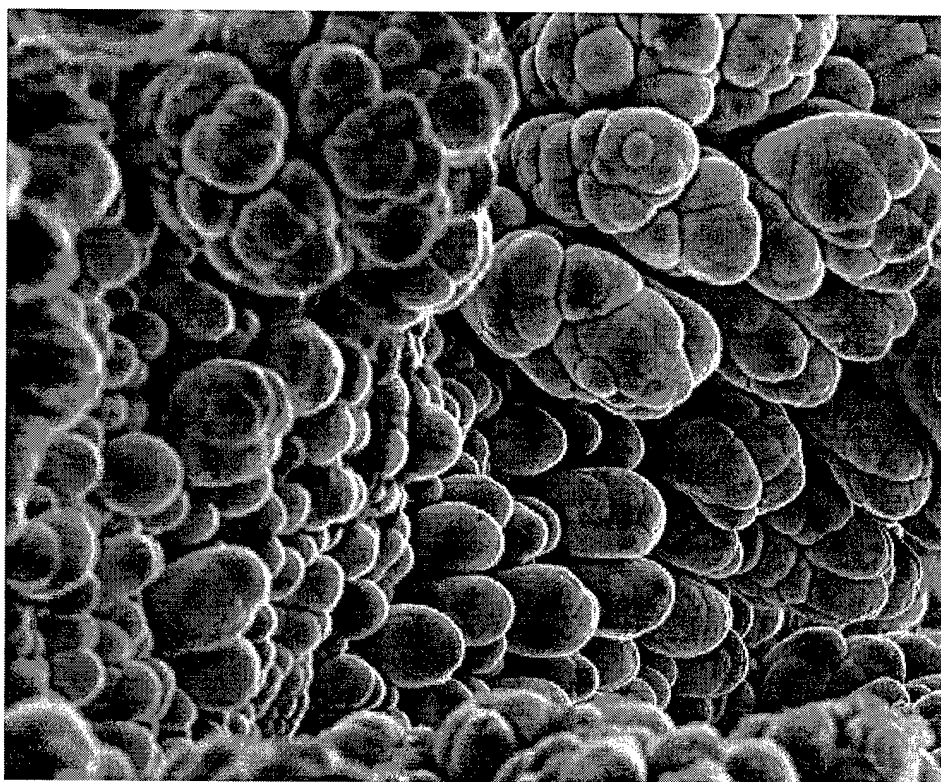


Figure 4.14 SEM secondary image of an iron electrodeposit. This deposit was prepared on a fixed copper wire from a 0.025 M solution of iron(II) in 60.0-40.0 m/o melt at $E_{\text{app}} = 0.35$ V.

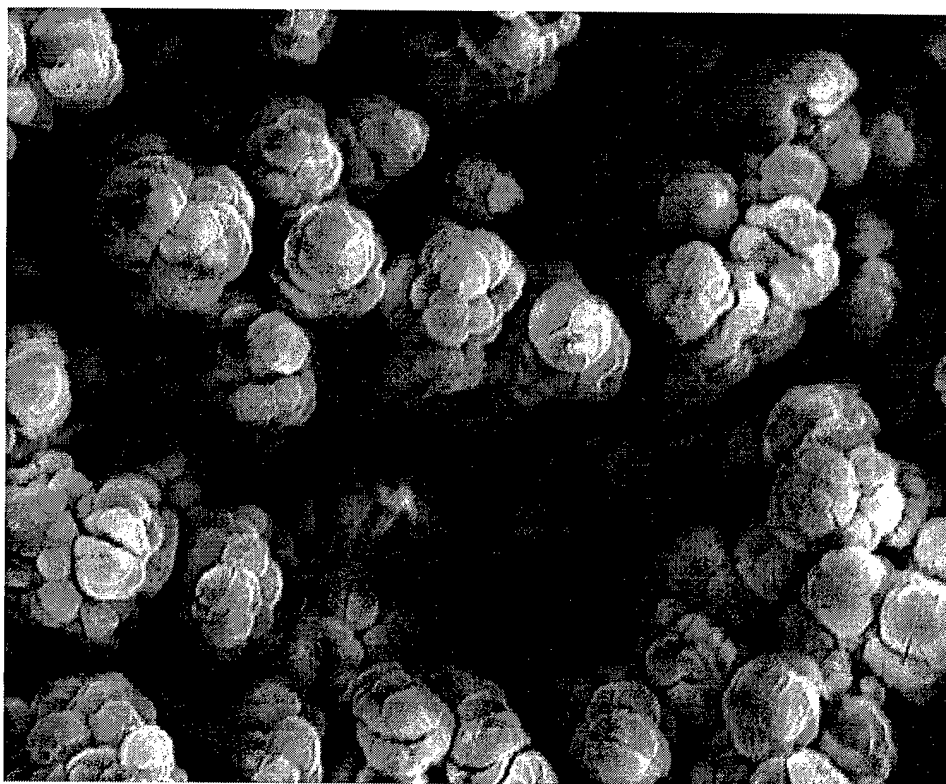


Figure 4.15 SEM secondary image of an iron electrodeposit. This deposit was prepared on a rotating copper disk electrode from a 0.025 M solution of iron(II) in 60.0-40.0 m/o melt at a current density of 30.1 mA cm^{-2} ($E_{\text{app}} = \text{ca. } -0.05 \text{ V}$).

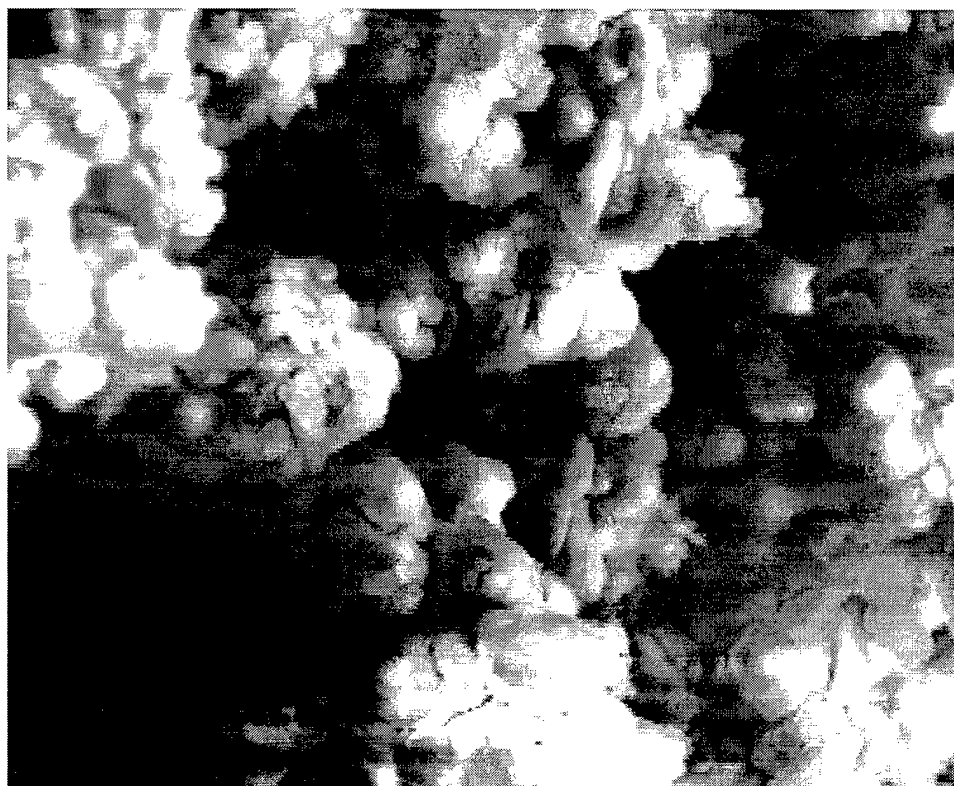


Figure 4.16 SEM secondary image of an iron electrodeposit. This deposit was prepared on a rotating copper disk electrode from a 0.025 M solution of iron(II) in 60.0-40.0 m/o melt at a current density of 75.3 mA cm^{-2} ($E_{\text{app}} = \text{ca. } -450 \text{ mV}$).

As the aluminum content increased, so did the chloride content. Thus, these results can only be used as qualitative indicators that as the potential is made more negative, the aluminum content of bulk deposits increases.

CHAPTER V. ELECTRODEPOSITION OF ANTIMONY

5.1 Anodic dissolution of antimony

Solutions of antimony(III) in the 60.0-40.0 m/o AlCl_3 -MeEtimCl melt were prepared by the controlled-potential coulometric anodization of an antimony rod working electrode at an applied potential of 1.2 V versus Al(III)/Al. To ensure that antimony(III) was the anodization product, the change in weight of the electrode was determined after the passage of a given charge, Q_{exp} . The results of several such controlled-potential coulometry experiments are given in Table 5.1. In this table, Δw_{Sb} is the change in the weight of the antimony electrode, m_{Sb} is the number of moles of antimony corresponding to this weight change, and $Q_{\text{theory}} (n = 1)$ is the theoretical charge based on m_{Sb} for $n = 1$. These calculations confirm that antimony(III) was the anodization product.

RDE voltammetry was used to determine E° ; E_{eq} was estimated from the zero current crossover point on the return sweep. The Nernst equation yielded $E^{\circ} = 1.02 \pm 0.03$ V at the 95 % confidence level. Data from 22 RDE experiments were used in the calculation of E° .

5.2 Voltammetry of antimony(III)

Stationary and RDE voltammograms for the electrodeposition and stripping of antimony on platinum, tungsten, and gold electrodes from a 0.025 M solution of

Table 5.1. Results for the anodization of antimony

Δw_{Sb} (g)	$10^4 m_{\text{Sb}}$ (mol)	$Q_{\text{theory}}(n = 1)$ (C)	Q_{exp} (C)	n
0.0225	1.83	17.68	43.43	2.46
0.0965	7.97	76.5	236.15	3.11
0.0607	4.99	48.1	180.91	3.80
0.0187	1.54	14.82	50.94	3.44
0.0213	1.75	16.88	50.00	2.96

avg: 3.0 ± 0.6

antimony(III) are shown in Figures 5.1 to 5.3 respectively. The stationary electrode voltammograms recorded at platinum, tungsten and gold are very similar; however, only the results for platinum (Figure 5.1a) will be described in detail. This voltammogram exhibits two reduction waves. A rather small wave appears first at ca. 0.952 V with $E_p^c = 0.76$ V on the forward scan. On the reverse scan, two oxidation waves are evident with $E_p^a = 1.29$ V for the major wave and $E_p^a = 1.45$ V for the second smaller wave. The position of the oxidation waves were independent of the switching potential. It has been shown in this laboratory that multiple stripping waves can be an indication of aluminum alloy formation (36, 42). However, voltammetry at a glassy carbon electrode (Figure 5.4a) shows no evidence of a second oxidation wave. This indicates that the second wave is probably not an Sb-Al alloy formed through the co-deposition of aluminum, but rather a surface alloy formed between antimony and the electrode (65). To investigate these results further, bulk deposits were made on platinum flags to determine if the second oxidation wave seen so clearly in the stationary electrode voltammograms, but absent from the RDE voltammograms is antimony or an antimony-aluminum alloy. The first deposit was made by performing a slow scan (0.001 V s^{-1}) voltammogram with a switching potential of 0 V. This cyclic voltammogram was stopped at 1.47 V, just prior to the second wave. SEM-EDAX of the resulting electrode deposits revealed that only antimony and platinum were present. A second deposit was made by stepping the potential of the platinum flag from the rest potential to 0 V and holding it there for 300 seconds. The deposit was then stripped by carrying out the anodic sweep, and it was also stopped at 1.47 V. The SEM-EDAX again showed that only antimony and

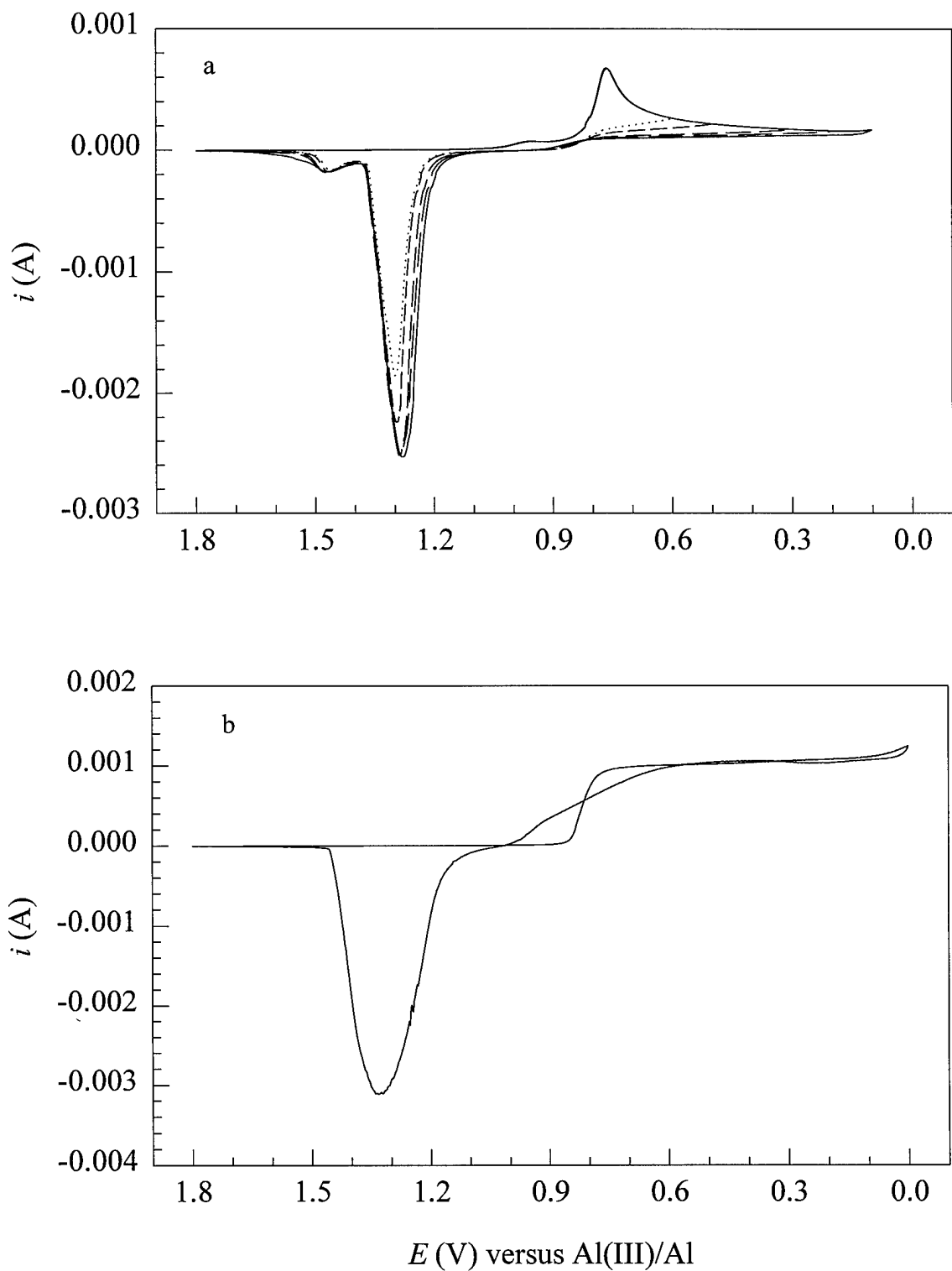


Figure 5.1 Voltammograms recorded at a platinum electrode in a 0.025 M solution of Sb(III) in 60.0-40.0 m/o AlCl_3 -MeEtimCl at 25 °C: (a) stationary electrode (scan rate = 0.050 V s^{-1}), (b) RDE (rotation rate = 104.7 s^{-1}).

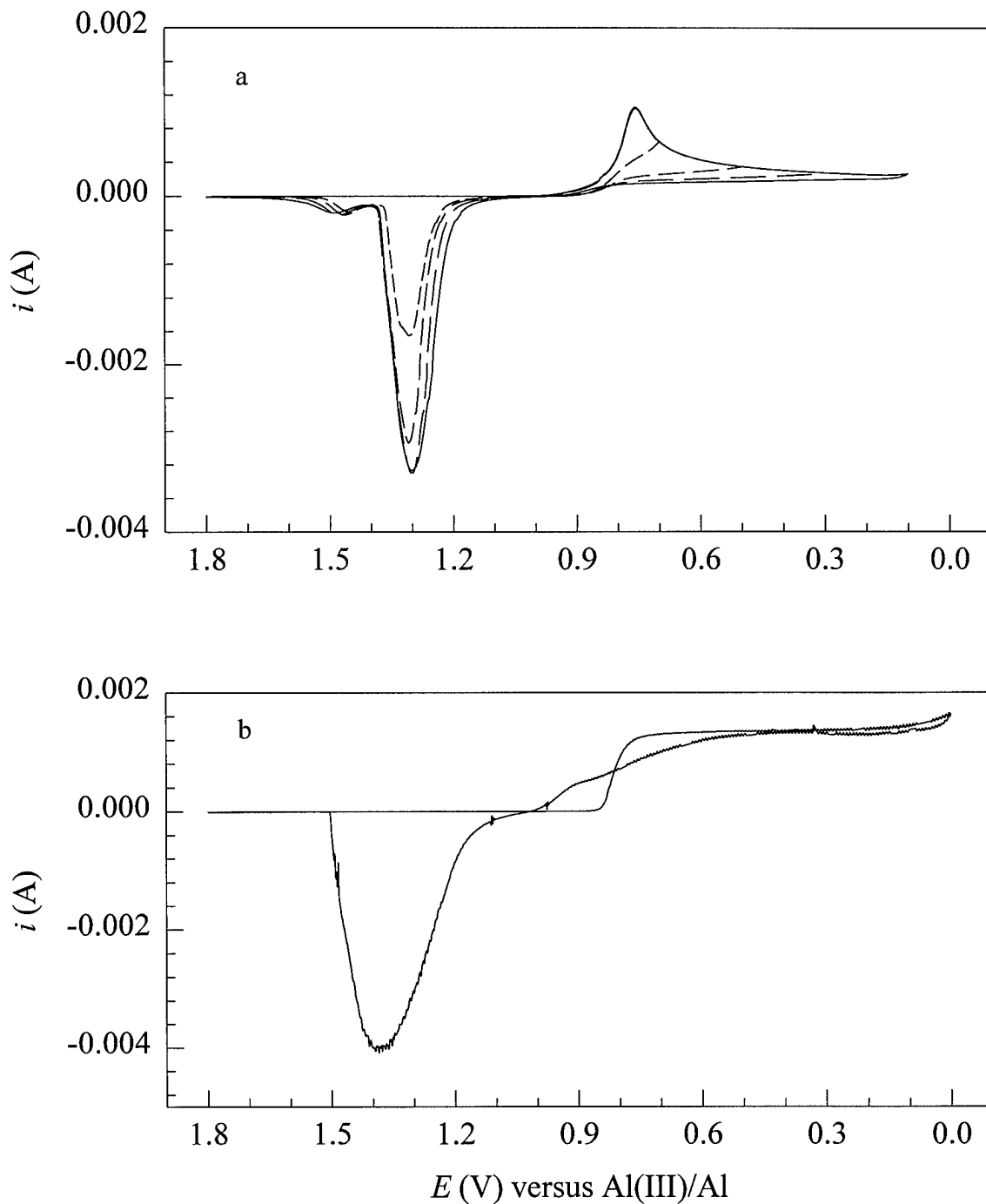


Figure 5.2. Voltammograms recorded at a tungsten electrode in a 0.025 M solution of Sb(III) in 60.0-40.0 m/o AlCl_3 -MeEtimCl at 25°C : (a) stationary electrode (scan rate = 0.050 V s^{-1}), (b) RDE (rotation rate = 104.7 s^{-1}).

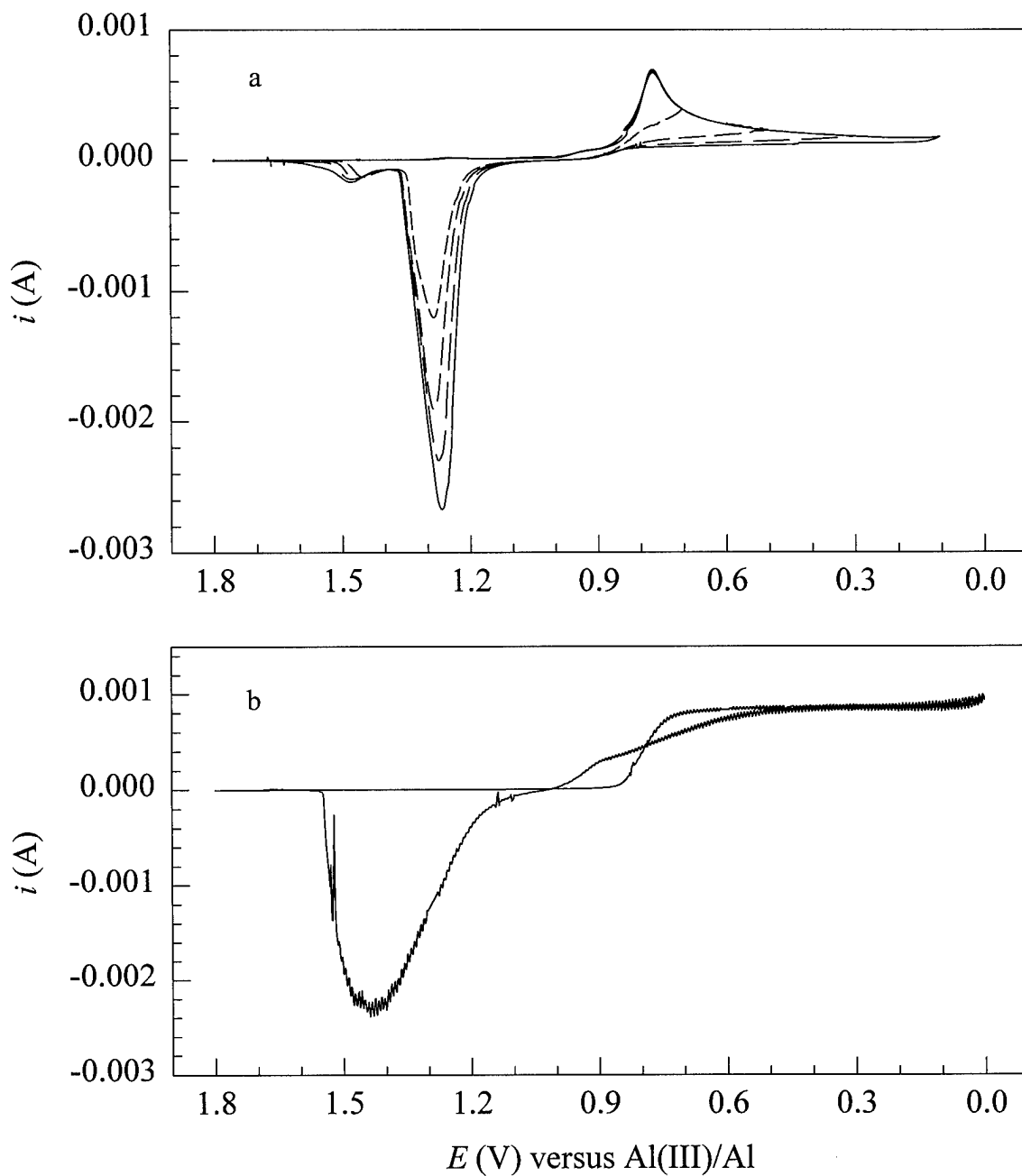


Figure 5.3. Voltammograms redorded at a gold electrode in a 0.025 M solution of Sb(III) in 60.0-40.0 m/o AlCl_3 -MeEtimCl at 25 °C: (a) stationary electrode (scan rate = 0.050V s^{-1}), (b) RDE (rotation rate = 104.7 s^{-1}).

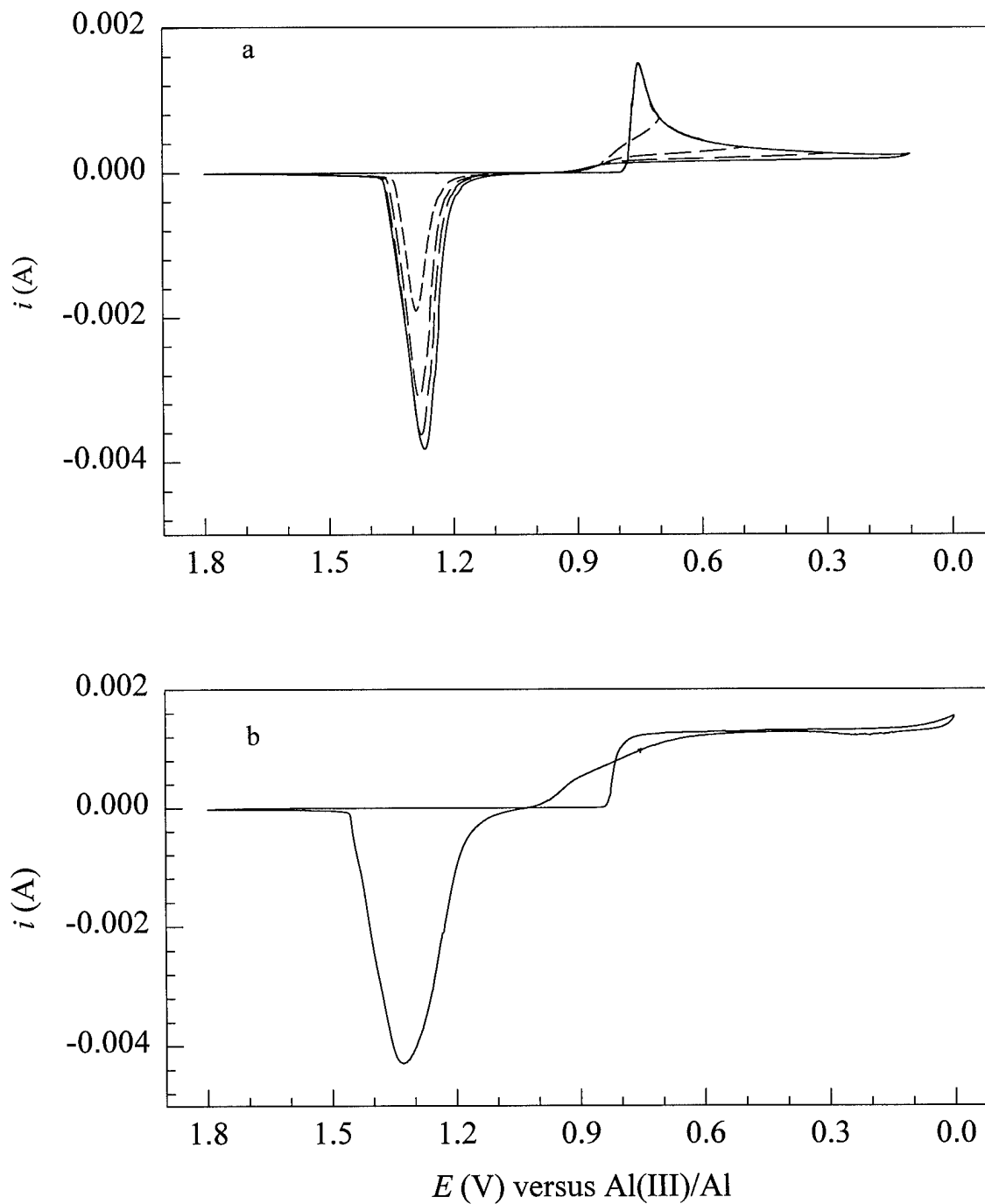


Figure 5.4. Voltammograms recorded at a glassy carbon electrode in a 0.025 M solution of Sb(III) in 60.0-40.0 m/o AlCl_3 -MeEtimCl at 25 °C: (a) stationary electrode (scan rate = 0.050 V s^{-1}), (b) RDE (rotation rate = 104.7 s^{-1}).

platinum were present. Thus, the reduction and oxidation waves in these voltammograms can be attributed to the reduction of antimony(III) solvated by the melt to antimony metal and to the oxidation of the antimony surface deposit to freely diffusing antimony(III), respectively.



Some typical data resulting from a series of stationary electrode cyclic voltammetric experiments at different scan rates, v , are shown in Table 5.2. Examination of the data in this table reveals that E_p^c shifts cathodically and that $i_p^c/v^{1/2}$ decreases as the scan rate is increased. For a reversible electrode reaction involving the deposition of an insoluble substance, $|E_p^c - E_{p/2}|$, where $E_{p/2}$ is the half-peak potential, should have a value of $0.77RT/nF$ or $0.0199/n$ V at 25 °C (72). However, $|E_p^c - E_{p/2}|$ in Table 5.2 clearly exceeds the value of 0.007 V expected for the reaction given in Equation 5.1, even at the slowest scan rate. Also note the inordinately large values of $E_p^c - E_p^a$ in Figure 5.1a; this large separation is indicative of a slow electron transfer. Taken together, the results presented above indicate that the antimony electrode reaction is at best quasi-reversible. Similar quasi-reversible behavior was found for the Ag(I)/Ag (19) and Sn(II)/Sn (29) electrode reactions at platinum in acidic AlCl_3 -MeEtimCl melt.

Figure 5.1b illustrates a typical RDE voltammogram for the deposition and stripping of antimony at the same polycrystalline platinum electrode that was used to acquire the stationary electrode voltammograms. A limiting current is evident as the electrode potential

Table 5.2. Cyclic voltammetric data for the reduction of Sb(III) at tungsten ($A = 0.196 \text{ cm}^2$), platinum ($A = 0.126 \text{ cm}^2$), and gold ($A = 0.126 \text{ cm}^2$) electrodes.

v (V s^{-1})	$10^4 i_p^c$ (A)	$10^3 i_p^c/v^{1/2}$ ($\text{A s}^{1/2} \text{ V}^{-1/2}$)	E_p^c (V)	E_p^a (V)	$ E_p^c - E_{p/2} $ (V)
platinum electrode					
0.010	3.68	3.68	0.790	1.272	0.040
0.030	5.65	3.26	0.774	1.290	0.056
0.050	6.80	3.04	0.764	1.298	0.066
0.070	7.60	2.87	0.758	1.306	0.476
0.090	8.23	2.74	0.752	1.312	0.482
tungsten electrode					
0.010	5.51	5.51	0.790	1.274	0.026
0.030	8.56	4.94	0.768	1.296	0.032
0.050	10.35	4.63	0.758	1.308	0.038
0.070	11.63	4.39	0.748	1.322	0.044
0.090	12.82	4.27	0.747	1.338	0.045
gold electrode					
0.010	3.77	3.77	0.756	1.304	0.058
0.030	5.77	3.33	0.762	1.298	0.046
0.050	6.91	3.09	0.768	1.292	0.036
0.070	7.77	2.94	0.776	1.280	0.028
0.090	8.41	2.80	0.794	1.262	0.010

is scanned below ca. 0.74 V, and a prominent, symmetrical oxidation wave is observed at ca. 1.32 V on the reverse scan.

The RDE voltammograms for the electrodeposition of antimony on platinum, tungsten, gold, and glassy carbon all exhibit well-defined limiting current plateaus. Thus, the Levich equation can be used to determine the diffusion coefficient from the limiting currents. Plots of j_l versus $\omega^{1/2}$ were linear and passed through the origin (Figure 5.5). This is indicative of a convective diffusion controlled reaction within the potential region of the limiting current.

The average values of $D_{\text{Sb(III)}}$ and $D_{\text{Sb(III)}}\eta/T$ for antimony(III) in the 60.0-40.0 m/o AlCl_3 -MeEtimCl melt at 25°C were calculated from the limiting currents of the four voltammograms shown in Figure 5.1b to 5.4b. The resulting values are $(1.1 \pm 0.1) \times 10^{-6} \text{ cm}^2 \text{ s}^{-1}$ and $5.98 \times 10^{-10} \text{ g cm s}^{-2} \text{ K}^{-1}$, respectively.

5.3 Sampled-current voltammetry of antimony(III)

Sampled-current voltammograms were constructed from chronoamperometric current-time transients resulting from experiments at each electrode in an unstirred solution containing electrogenerated antimony(III). In these experiments, the potential was stepped from an initial value of 1.50 V, where no Faradaic processes occur, to potentials ranging from 0 to 0.80 V; the solution was stirred before the application of each potential pulse to assure a uniform concentration and then allowed to rest for 60 seconds prior to the pulse. The current was then sampled at the same elapsed time for each current-time transient and plotted as a function of potential. In order to produce a reproducible response, the electrode surface was cleaned anodically by stepping the electrode potential to 1.8 V for 60 s prior to each

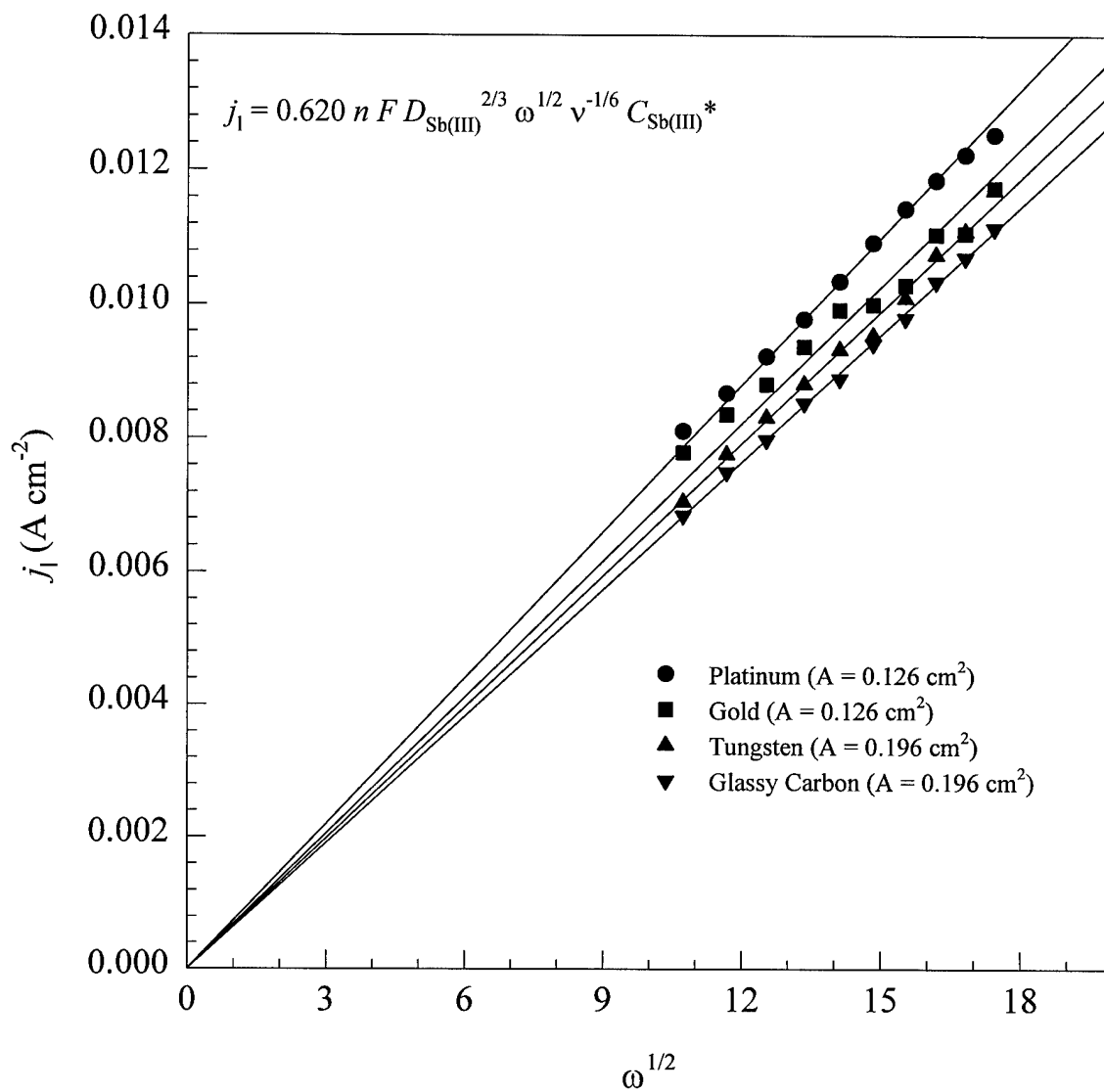


Figure 5.5 Plots of the limiting cathodic current density for the reduction of Sb(III) in 60.0-40.0 m/o AlCl_3 -MeEtimCl melt at 25 °C at platinum, gold, tungsten, and glassy carbon electrodes versus the square root of the electrode rotation rate ($\omega^{1/2}$).

potential step experiment while the electrode was rotated. The sampled-current voltammograms that resulted from these experiments are shown in Figure 5.6. Like the RDE voltammograms, these sampled-current voltammograms exhibit well-defined limiting currents, and it can be concluded from these waves that no appreciable co-deposition of aluminum occurs prior to the bulk deposition of aluminum at 0 V during the electrodeposition of antimony. Additional support for this conclusion is obtained from bulk deposition experiments (*vide infra*). In order for an antimony-aluminum alloy to form at potentials more positive than 0 V versus Al(III)/Al, the UPD of aluminum on antimony must occur. To demonstrate that the UPD of aluminum can occur on an antimony surface, cyclic voltammetric experiments were conducted at a polycrystalline antimony electrode in blank 60.0-40.0 m/o melt at 25 °C. Figure 5.7 shows the voltammogram recorded under those conditions. The voltammogram is characterized by a reduction wave on the forward scan with $E_p^c = 0.65$ V and a well defined stripping wave with $E_p^a = 0.55$ V. Thus the UPD of aluminum onto antimony is demonstrated, and this indicates that aluminum may co-deposit with antimony at potentials positive of 0 V. Therefore, the conclusion that aluminum does not co-deposit with antimony is somewhat unexpected because of the UPD of aluminum can be predicted theoretically on the basis of the work function difference for aluminum and antimony, $\phi_{Al} = 4.28$ eV and $\phi_{Sb} = 4.55$ (81- 83), and observed experimentally. Yet, no such co-deposition occurs. A phase diagram of the aluminum-antimony alloy system indicates that the solubility of aluminum in antimony is very small (84) showing the formation of a single line compound, AlSb. Thus, it appears that the difference in work functions and the solubility of aluminum in the depositing transition metal must both be favorable if the co-deposition

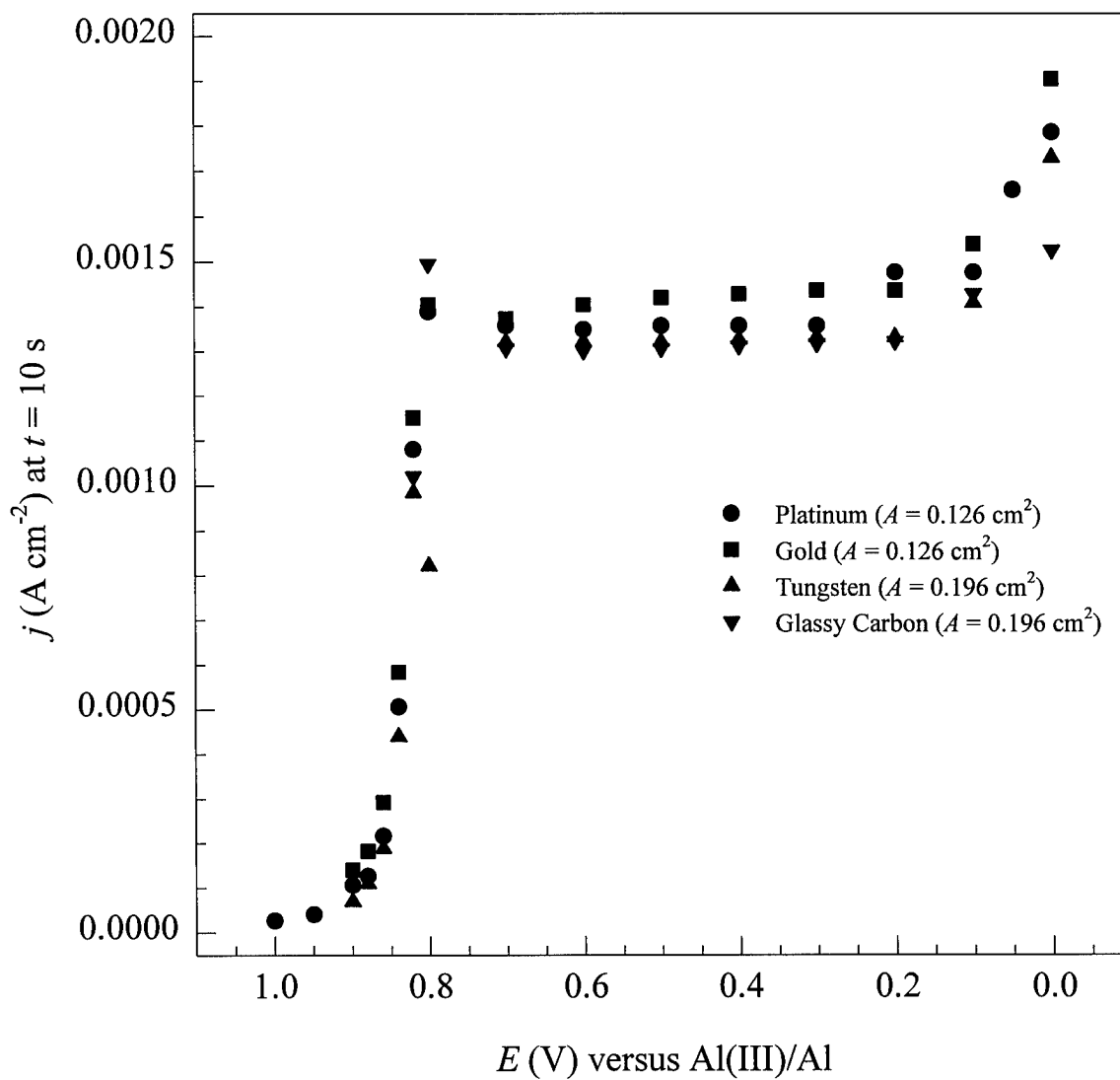


Figure 5.6 Sampled-current voltammograms for the reduction of Sb(III) in 60.0-40.0 m/o melt at platinum, gold, tungsten and glassy carbon electrodes.

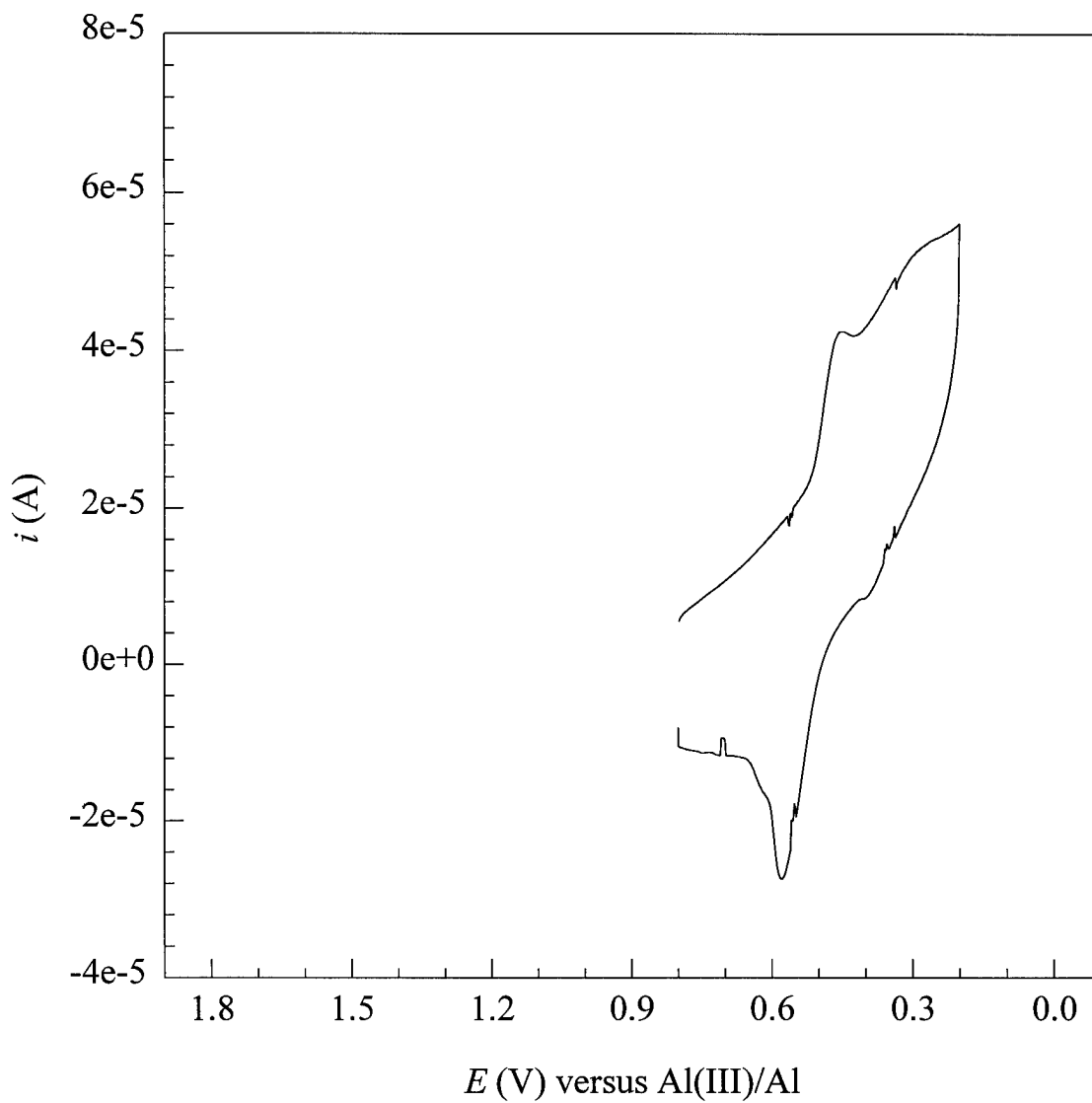


Figure 5.7 Underpotential deposition of aluminum onto an antimony working electrode. This cyclic voltammogram was acquired in pure 60.0-40.0 m/o melt.

of aluminum with transition metals is to occur at $E_{app} > 0$ V is to take place.

The average values of $D_{Sb(III)}$ and $D_{Sb(III)}\eta/T$ for antimony(III) in the 60.0-40.0 m/o $AlCl_3$ -MeEtimCl melt at 25°C were calculated from the chronoamperometric current-time transients by using the Cottrell equation. Plots of j_1 versus $t^{-1/2}$ are linear and pass through the origin (Figure 5.8). The

resulting values are $D_{Sb(III)} = (1.12 \pm 0.1) \times 10^{-6} \text{ cm}^2 \text{ s}^{-1}$ and $D_{Sb(III)}\eta/T = 5.98 \times 10^{-10} \text{ g cm s}^{-2} \text{ K}^{-1}$, respectively, in excellent agreement with the results from the RDE experiments.

5.4 Nucleation of antimony on glassy carbon

Stationary and RDE voltammograms for the electrodeposition and stripping of antimony at a glassy carbon electrode are shown in Figure 5.4. The current loops seen in both voltammograms after reversal of the forward scan are typical of those associated with an overpotential-driven nucleation process. These current loops occur because the deposition of antimony on glassy carbon during the forward scan requires an overpotential in order to initiate the nucleation and subsequent growth of an antimony deposit; after the scan is reversed, the reduction of antimony continues at more positive potentials because antimony is deposited on an antimony surface rather than on the hostile glassy carbon surface.

Plots of $(i/i_m)^{2/3}$ versus t that were constructed from data taken from the rising portions of the experimental current-time transients in Figure 5.9a were linear; therefore the intercepts of these plots were used to obtain estimates of t_0 . The resulting values of t_0 are shown in Table 5.3. Figure 5.10 shows a plot of the log of the induction time versus the overpotential.

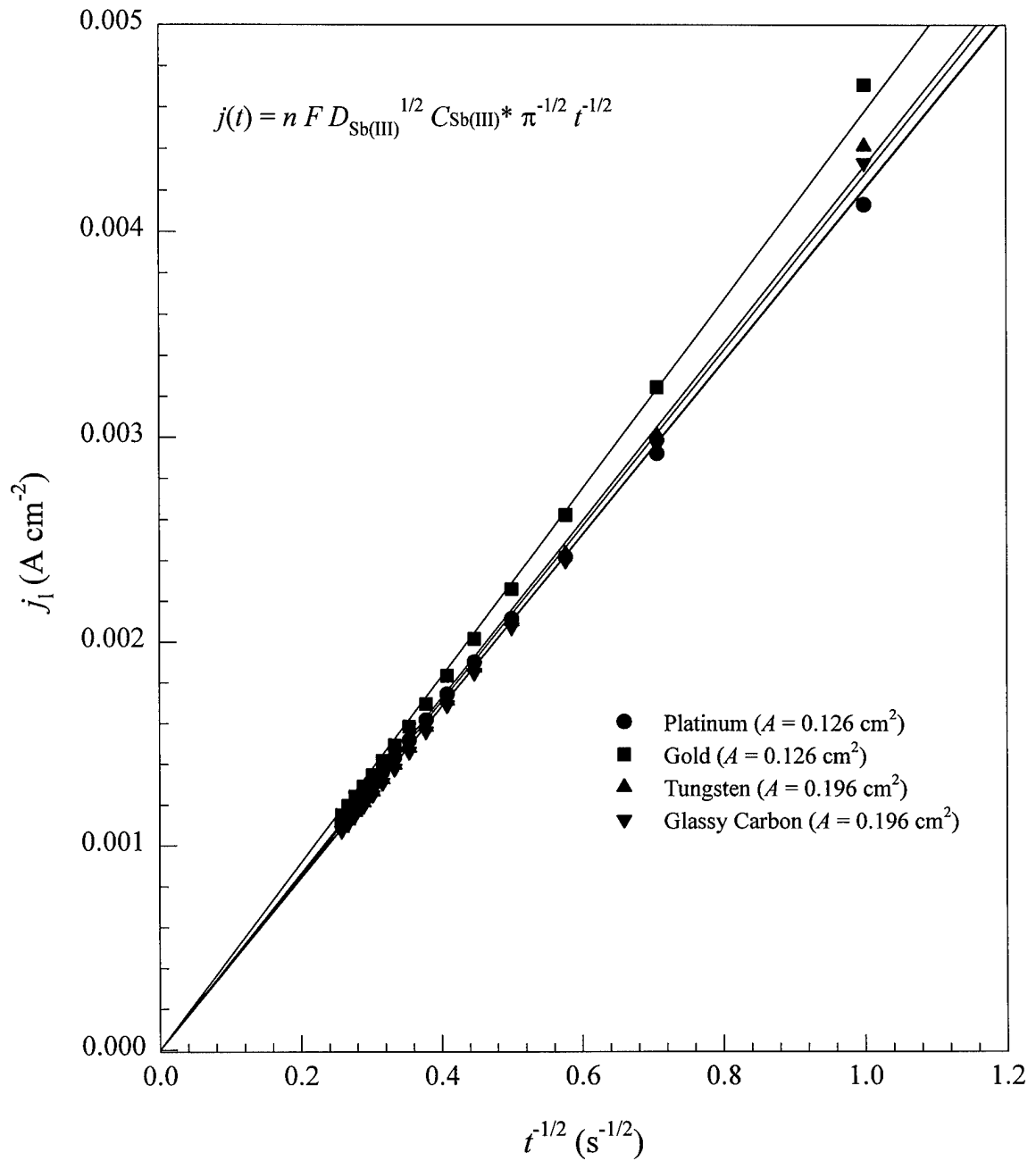


Figure 5.8 Plots of the limiting cathodic currents for the reduction of Sb(III) in 60.0-40.0 m/o melt versus the reciprocal of the square root of time ($t^{-1/2}$). These plots were constructed from chronoamperometric data.

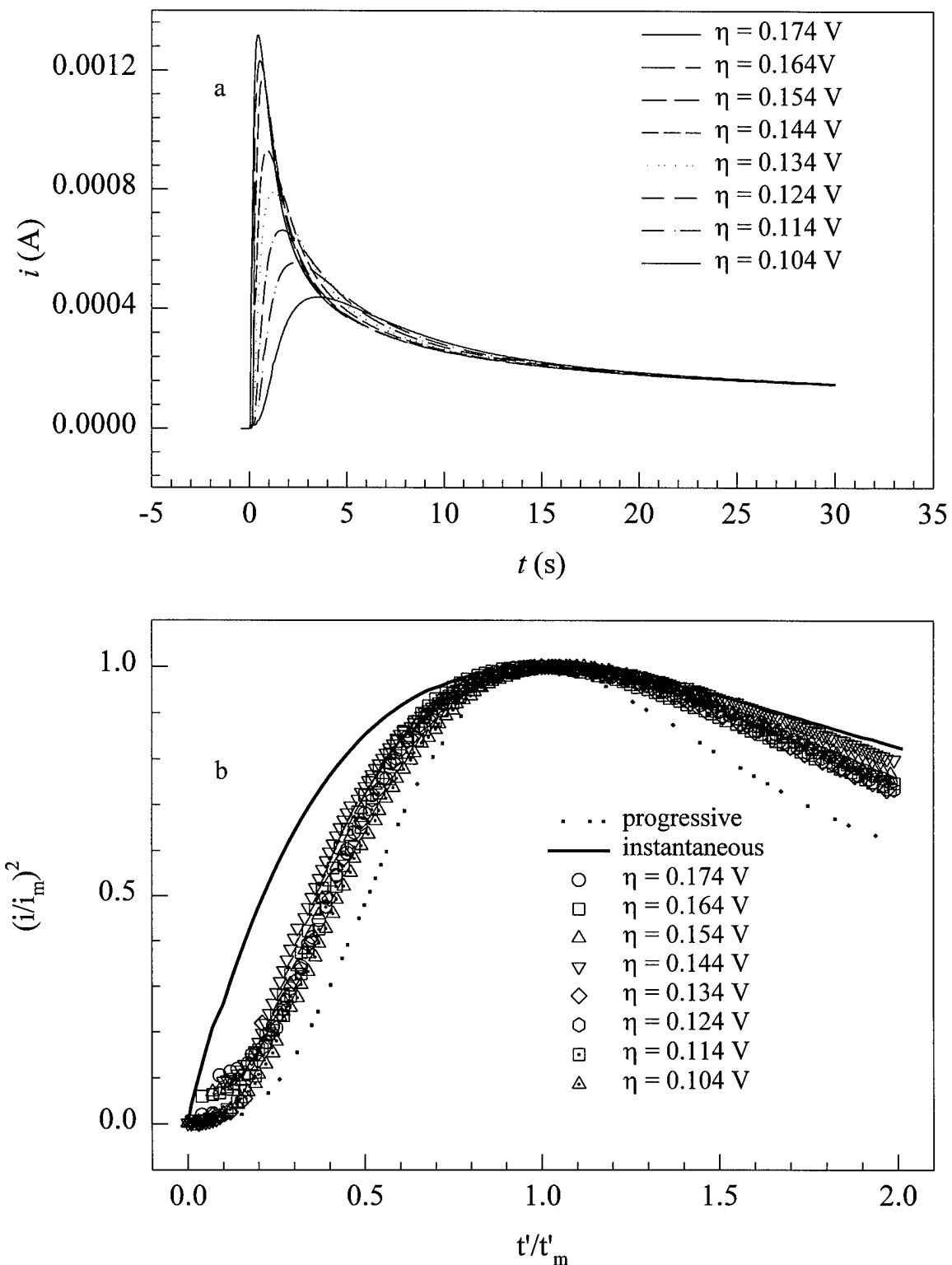


Figure 5.9 (a) Dimensionless experimental current-time transients for the reduction of Sb(III) in 60.0-40.0 m/o melt at glassy carbon. (b) comparison of the current-time transients in part a to the theoretical transients for progressive and instantaneous 3-DHDCG.

Table 5.3. Nucleation data for the electrodeposition of antimony on glassy carbon.

E_{app} V	η V	i_m A	t_m s	t_0 s	$10^7 i_m^2 t_m'$ $A^2 s$	α	x	$10^{-7} N_0$ cm^{-2}	A_t s^{-1}	$10^{-8} N_0 A_t$ $\text{cm}^{-2} \text{s}^{-1}$
0.730	0.174	0.001317	0.43	0.03	6.88	0.4151	2.018	1.28	11.31	1.45
0.740	0.164	0.001249	0.49	0.05	6.85	0.3732	2.010	1.12	10.99	1.23
0.750	0.154	0.001078	0.62	0.07	6.41	0.3313	1.854	0.816	9.03	0.737
0.760	0.144	0.000799	1.01	0.09	5.90	0.1646	1.543	0.417	9.28	0.387
0.770	0.134	0.000790	1.20	0.12	6.72	0.4931	2.151	0.489	3.64	0.178
0.780	0.124	0.000662	1.69	0.19	6.59	0.5110	2.172	0.351	2.52	0.0883
0.790	0.114	0.000553	2.25	0.27	6.04					
0.800	0.104	0.000439	3.35	0.40	5.69					
0.810	0.094	0.000333	5.60	0.76	5.37					
0.820	0.084	0.000245	9.00	1.54	4.48					
0.830	0.074	0.000166	16.05	3.33	3.50					

$$E_{\text{eq}} = 0.904 \text{ V}$$

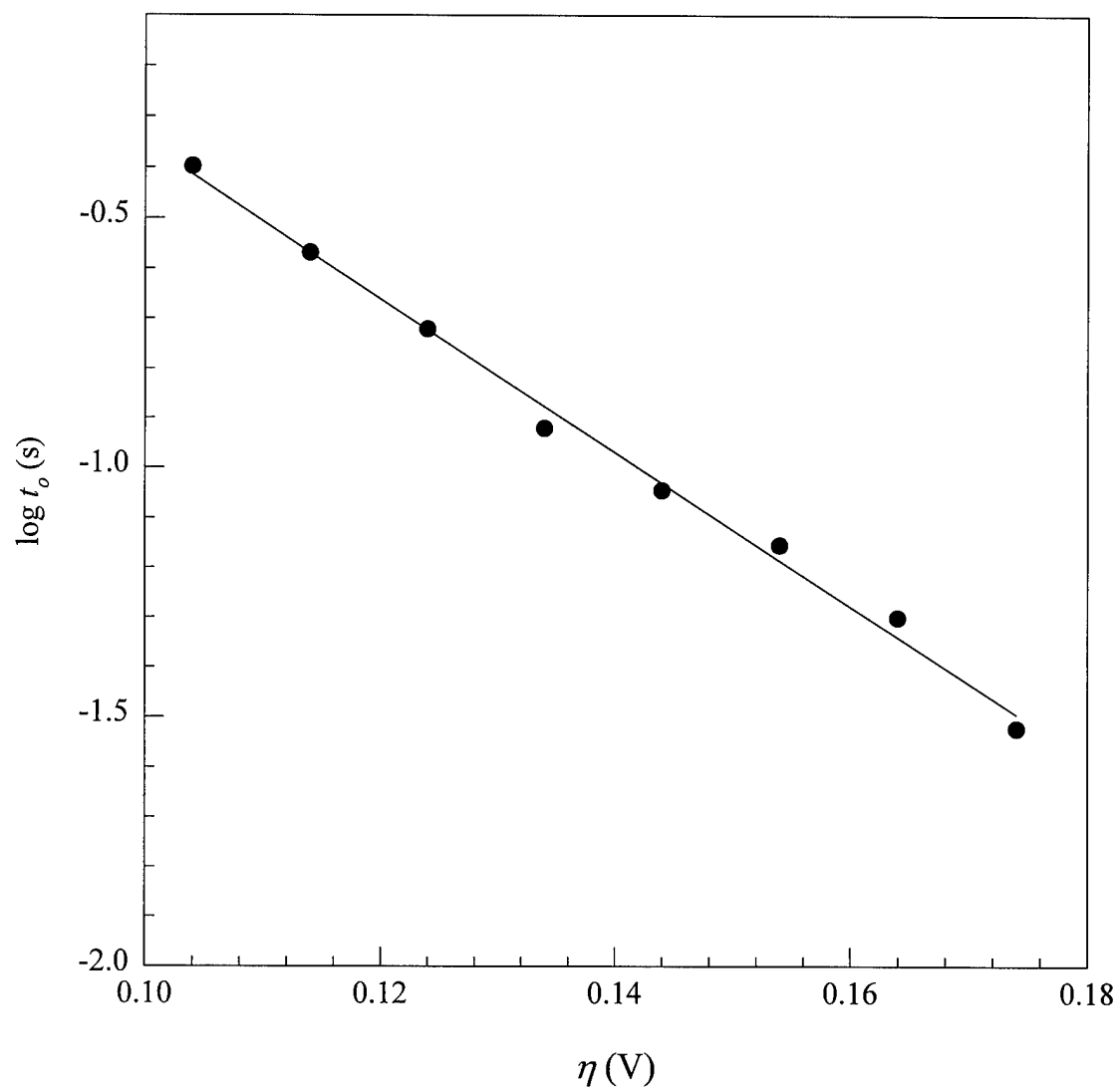


Figure 5.10 Plot of $\log t_0$ versus η from the transients given in Figure 4.9a. The slope of this plot equals 0.0648 V.

According to Ramamurthy and Kuwana, (85) the decrease of the induction time with overpotential, as seen in Figure 5.10, indicates that the rate of nucleation is limited by a heterogeneous electron-transfer process. In describing a similar exponential behavior observed during the nucleation of PbO₂, Chang and Johnson (86) proposed that the inverse relationship between induction time and overpotential is similar to the relationship between current and overpotential as given by the Tafel equation (72).

$$\log i/(1-e^{-\eta}) = \log i_0 - \alpha n F \eta / 2.3 RT \quad [5.1]$$

The slope in Figure 5.10 is 0.0648 V; this value is in excellent agreement with the slope determined by Phillips *et al.* (87), (0.066 V), during an investigation of the electrodeposition of Tl₂O₃ on glassy carbon.

Table 5.3 also lists the product $i_m^2 t_m'$ as a function of overpotential. The overpotentials that were applied during each chronoamperometry experiment correspond to the limiting currents in Figure 5.4. Under these conditions, the growth process is considered to be diffusion controlled, *i.e.*, $C_{Sb(III)}(x=0) \approx 0$, if $i_m^2 t_m'$ does not vary with η ; (54) the data in Table 5.3 indicate that this is not the case, unless $E_{app} < 0.78$ V.

In Figure 5.9b, the experimental dimensionless current-time transients from several experiments are compared to the theoretical transients that were calculated from Equations 1.17 and 1.18. The experimental transients appear to fall between the limiting models for progressive and instantaneous nucleation, suggesting that the deposition of antimony on glassy carbon involves progressive three-dimensional nucleation on a finite number of active

sites with hemispherical diffusion-controlled growth of the nuclei(68). The theoretical transient for this model is represented by Equation 1.19 (68). Equation 1.19 was fit to the experimental data by adjusting the values of α , t_o , and x using a curve fitting program based on the Marquardt-Levenberg algorithm. The adjustable parameters α and x contain information about N_0 (cm^{-2}), and A_t (s^{-1}) as given by Equations 1.25 and 1.26 (68). The curve fitting results are collected in Table 5.3 along with the value N_s , which is calculated from $A_t N_0$ according to Equation 1.23 (61).

According to the atomistic theory of nucleation, the slope of a plot of $\log(A_t)$ versus η gives information about the critical number of atoms required for the formation of a stable nucleus, n_k (66). A plot of $\log A_t$ versus η that was constructed from the data in Table 5.3 is shown in Figure 5.11. It is linear with a slope of $17.6 \text{ s}^{-1} \text{ cm}^{-2} \text{ V}^{-1}$ and a correlation coefficient of 0.965. n_k is related to this slope by Equation 1.24, where k is the Boltzmann constant, e_0 is the elementary charge, and α is the cathodic transfer coefficient (88). If α is assumed to have a value of 0.50, then Equation 9 gives $n_k \approx 0$. This indicates that active sites on the electrode surface probably act as the critical nucleus (89) during the electrodeposition of antimony on glassy carbon from acidic AlCl_3 -MeEtimCl. Values of n_k ranging from 0 to 1 were reported for the electrodeposition of cadmium (90), copper (91), lead (92, 38), and silver (93, 94) on glassy carbon in aqueous solutions.

5.5 Characterization of bulk antimony deposits

Bulk electrodeposits were prepared on 1 mm diameter nickel wire electrodes. The plating solutions were gently stirred with a Teflon-coated stir bar during electrodeposition

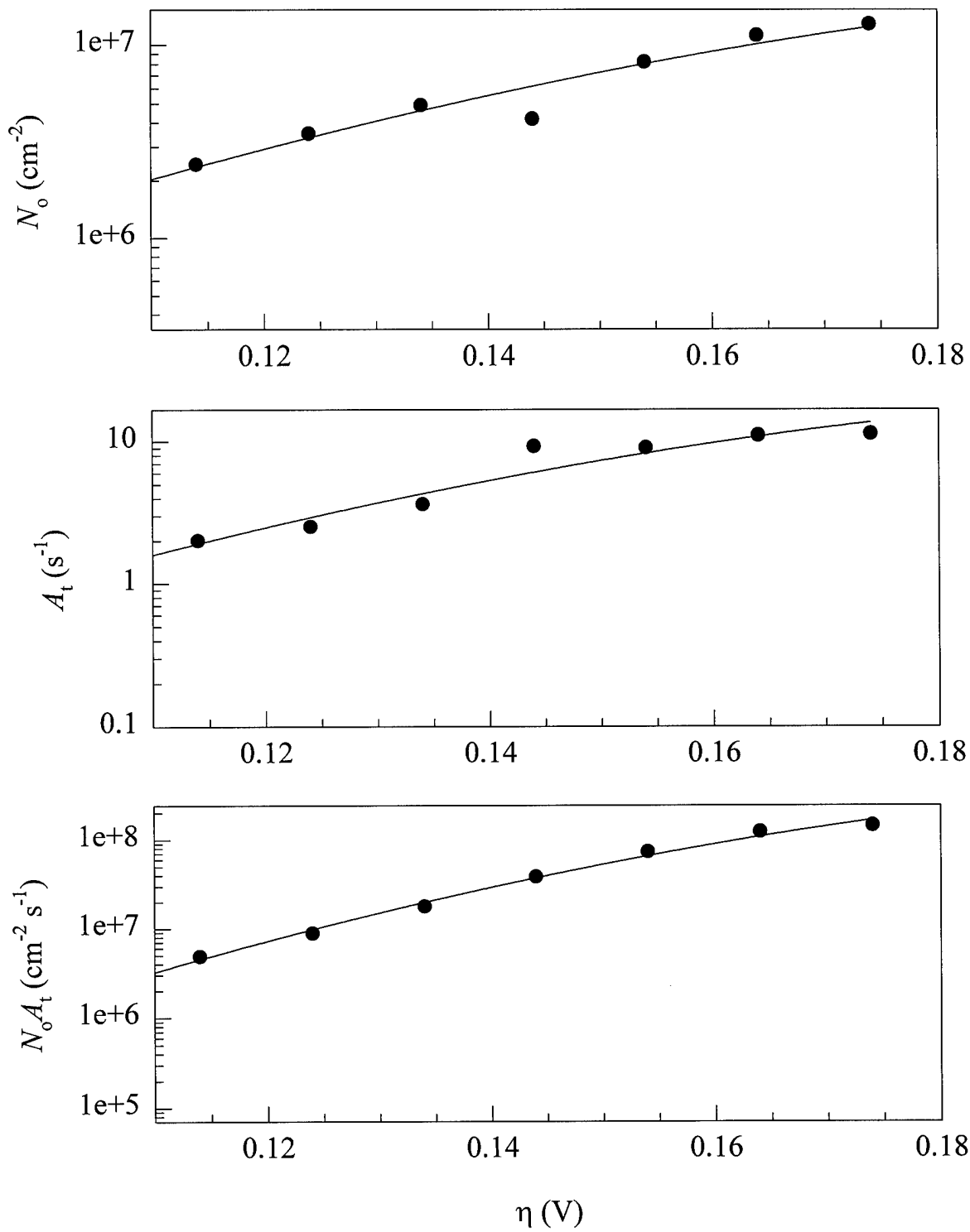


Figure 5.11 Plots of N_o , A_t and $N_o A_t$ versus η that were constructed from data in Table 5.3.

experiments. Following each experiment, the deposits were immediately taken from the plating bath while under cathodic protection and washed with dry benzene to remove any plating bath residue. They were then removed from the glove box and washed in succession with ethanol, acetone, and water. Deposits were prepared at a charge density of approximately 50 C cm^{-2} at applied potentials of 0.80, 0.70, 0.50, 0.30, 0.10, and 0 V. Deposits were also made at constant current with an approximate charge density of 50 C cm^{-2} . The current densities used ranged from 6.37 to 20.47 mA/cm^2 , and the resulting negative potentials ranged from -120 mV to -375 mV, respectively.

SEM-EDAX results revealed that the constant current deposits consisted of approximately 60% aluminum and 40% antimony. A small amount of chloride (< 1%) was found and is believed to come from the incorporation of the AlCl_3 -MeEtimCl melt into the deposit. Deposits produced under constant potential conditions were found to be pure antimony at all potentials. Only trace amounts of aluminum and chloride were detected and were attributed to incorporation of melt into the deposit. The as-deposited surface morphologies of the constant potential electrodeposits are shown in Figure 5.12, and they showed virtually no significant variation as a function of potential. All constant potential electrodeposits between 0 and 0.8 V have the same densely packed grape-like nodular appearance. EDS analysis of these deposits indicated that they were pure antimony and free of chloride contamination. This is not unexpected and confirms the results of the sampled-current voltammetry. The as-deposited surface morphologies of the constant current electrodeposits are shown in Figure 5.13. The deposition potentials for all of these deposits were negative. The potentials ranged from -120 mV at $j_{\text{app}} = 5 \text{ mA}$, to -375 mV at $j_{\text{app}} = 20$

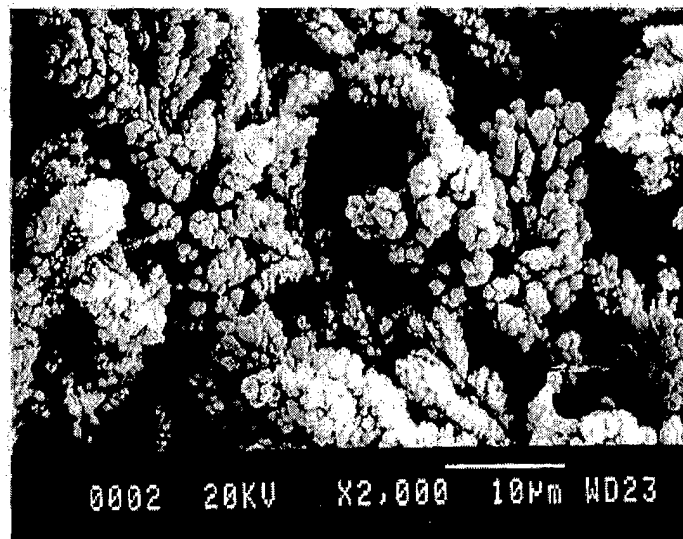
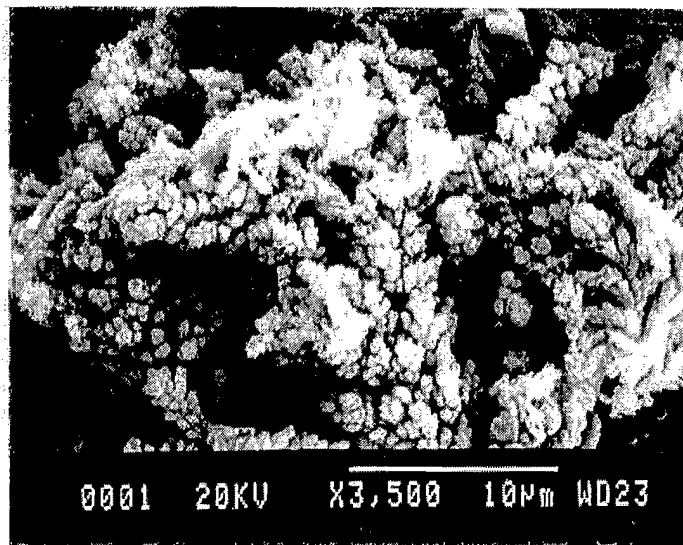


Figure 5.12 SEM images of antimony electrodeposits. (top) $E_{app} = 0$ V. (bottom) $E_{app} = 0.8$ V.

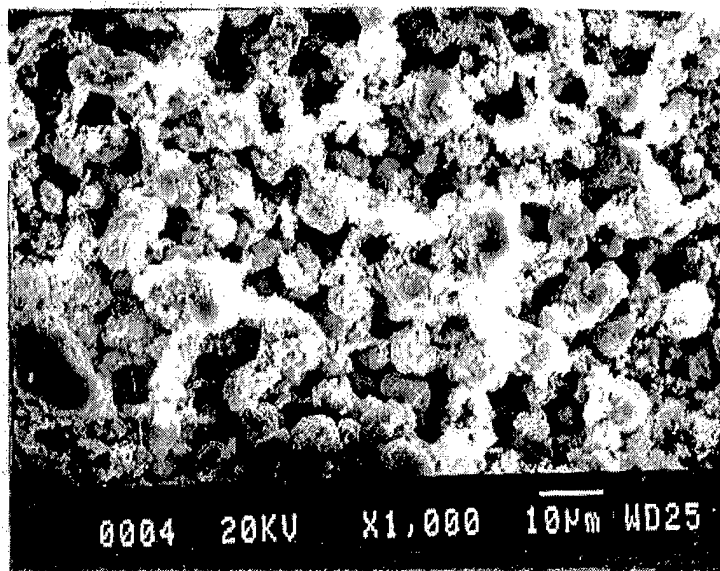
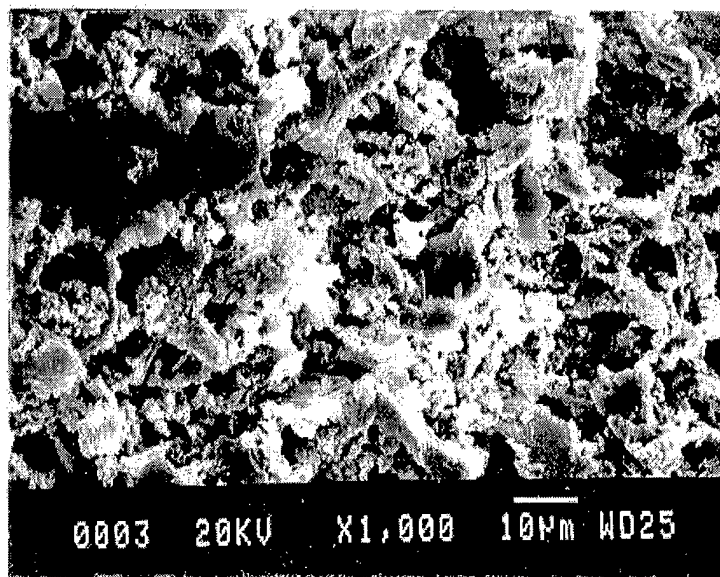


Figure 5.13 SEM images of antimony electrodeposits. (top) $i_{app} = 5.0$ mA. (bottom) $i_{app} = 20$ mA.

mA. The as-deposited surface morphology again showed little variation. All of the constant current deposits have a similar coral like appearance, distinctly different from the that of the constant potential deposits. These deposits have a less nodular appearance and a more coral like separation with a more complete and uniform coverage. The most significant aspect of these deposits is their aluminum content. At these negative potentials it is possible to co-deposit aluminum and antimony and obtain deposits containing as much as 60 atomic % aluminum.

CHAPTER VI. SUMMARY AND CONCLUSIONS

The results reported in the preceding chapters demonstrate that Co-Al, Fe-Al, and Sb-Al alloys can be electrodeposited from the acidic AlCl_3 -MeEtimCl room-temperature molten salt. The Co-Al and Fe-Al alloys were found to co-deposit at potentials positive of the Al(III)/Al couple ($E_{\text{app}} = 0$ V, i.e., at underpotentials. However, the Sb-Al alloy was only deposited at potentials negative of 0 V.

When the work function of aluminum is lower than the work function of the other metal there is a free energy advantage for underpotential co-deposition of aluminum with the metal. In view of the fact that the work function difference between Sb-Al is similar to that of Co-Al and Fe-Al, the underpotential co-deposition of Al with Sb was expected. However, this study revealed that the electrodeposition of antimony was not accompanied by the co-deposition of aluminum at potentials less than those required to initiate the bulk deposition of aluminum. One reason for this behavior may be that the solubility of aluminum in antimony is very small (84). Thus, two important factors that must be considered in order to predict the underpotential co-deposition of aluminum with transition and main group metals appear to be the difference in work functions and the solubility of aluminum in the depositing metal.

The mole fraction of aluminum found in bulk deposits was sometimes lower than that predicted on the basis of the various voltammetric measurements. This discrepancy is believed to arise from the oxidative leaching of aluminum from the alloys by the more noble

transition metal cations present in the plating bath during the electrodeposition process. It is possible for this to occur if the alloy deposits are very dendritic and become detached and "electrically isolated" from the electrode. In the case of thin-layer voltammetric deposits produced during chronoamperometric experiments, the charge passed during these measurements is so small that dendritic deposits can not form and furthermore, leaching of aluminum from the alloy does not take place because the deposit is under continuous cathodic protection.

The technique developed during this research project that involves anodic linear sweep voltammetry at a rotating ring-disk electrode, (ALS_V-RRDE) proved to be a powerful *in situ* tool for gaining quantitative insight (74-76) into the phase composition of alloys electrodeposited at underpotentials such as Co-Al and Fe-Al. The efficacy of this technique was validated by current-sampled voltammetry.

Chronoamperometry was used to investigate the fundamental aspects of the nucleation and growth of cobalt, iron, and antimony on glassy carbon substrates in the AlCl₃-MeEtimCl molten salt. The results obtained for the electrodeposition of different metals at different substrates are compared in Table 6.1. The dimensionless experimental current-time transients were in good agreement with the theoretical model for progressive three dimensional hemispherical diffusion controlled growth (3D-HDCG) (Table 6.1). Using the atomistic theory of nucleation, it was determined in all three cases that the critical number of atoms required to form a stable nucleus was zero, *i.e.*, during the nucleation and growth of cobalt, iron, and antimony nuclei on glassy carbon, active sites on the glassy carbon surface

Table 6.1. Summary of the different electrodeposition mechanisms observed in the 60.0-40.0 m/o AlCl₃-MeEtimCl molten salt at 25 °C.

metals	glassy carbon	substrate		
		gold	platinum	tungsten
cobalt	progressive 3D-HDCG	UPD	UPD	
iron	progressive 3D-HDCG	UPD	UPD	
antimony	progressive on a finite number of active sites	UPD	UPD	

act as critical nuclei. This appears to be a general result for glassy carbon because similar results were obtained during the electrodeposition of zinc (36).

Thermodynamic data about the M^{n+}/M couples and transport data about the M^{n+} species were obtained. The formal potentials of the M^{n+}/M couples were determined by either constructing Nernst plots, or using the cross-over potentials from RDE voltammetry experiments. The formal potentials for each of the electrochemical couples measured during this research are collected in Table 6.2. The reduction potentials of these couples in aqueous solution are shown for comparison. The lack of a correlation between these two sets of E^0 values provides solid evidence that the various metal ions are solvated very differently in these two solvents. The diffusion coefficients and Stokes-Einstein products of cobalt(II), iron(II), and antimony (III) in the 60.0-40.0 m/o $AlCl_3$ -MeEtimCl molten salt are collected in Table 6.3.

Table 6.2 Formal potentials of the redox couples studied in this research.

Redox couple	$E^{\circ'}$ (molten salt)	E° (aqueous)
	V versus Al(III)/Al	V versus NHE
Co(II)/Co	0.86 ± 0.02	-0.28
Fe(II)/Fe	0.52 ± 0.01	-0.41
Sb(III)/Sb	1.02 ± 0.01	-0.51

Table 6.3 Diffusion coefficients and Stokes-Einstein products of species studied in this research.

Species	$10^6 D_0$	$10^{10} \eta D_0 / T$
	$\text{cm}^2 \text{s}^{-1}$	$\text{g cm s}^{-2} \text{K}^{-1}$
Co(II)	3.4 ± 0.1	1.8
Fe(II)	2.6 ± 0.3	0.14
Sb(III)	1.1 ± 0.1	5.98

LIST OF REFERENCES

LIST OF REFERENCES

1. *Mineral Commodity Summaries*, U.S. Dept. of the Interior, Bureau of Mines, pg. 20, Jan.1994.
2. W. A. Badawy and B. A. Sabrah, *J. App. Electrochem.* **18**, 220-224 (1988).
3. *Amorphous Metallic Alloys*, E. Lubrosky, Editor, Butterworths, London (1983).
4. S. Annyanov and G. Sotirova-Chakarova, *J. Electrochem. Soc.*, **139**, 3454 (1992).
5. W. C. Grande and J. B. Talbot, G. R. Stafford, *J. Electrochem. Soc.*, **140**, 675 (1 993).
6. Y. P. Lin and J. R. Selman, *J. Electrochem. Soc.*, **140**, 1304 (1993).
7. F. H. Hurley and T. P. Wier, *J. Electrochem. Soc.*, **98**, 203 (1951).
8. F. H. Hurley and T. P. Wier, *ibid.*, **98**, 207 (1951).
9. F. H. Hurley, U. S. Pat. 2,446,331, Aug. 3, 1948.
10. T. P. Wier and F. H. Hurley, U. S. Pat 2,466,349, Aug. 3, 1948.
11. T. P. Wier, U. S. Pat. 2, 446, 350, Aug. 3, 1948.
12. R. A. Carpio, L. A. King, R. E. Lindstrom, J. C. Nardi, and C. L. Hussey, *J. Electrochem. Soc.*, **126**, 1644 (1979).
13. J. S. Wilkes, J. A. Levisky, R. A. Wilson, and C. L. Hussey, *Inorg. Chem.*, **21**, 1263 (1982).
14. C. L. Hussey, in *Chemistry of Nonaqueous Solutions: Current Progress*, G. Mamantov and A.I. Popov, Editors, pp. 227-275, VCH, New York (1994).
15. R. A. Osteryoung in "*Molten Salt Chemistry: An Introduction and Selected Applications*," NATO ASI Series C: Mathematical and Physical Sciences, Vol. 202, G. Mamantov and R. Marassi, Editors, p. 329, Reidel, Dordrecht (1987).

16. G. R. Stafford, *J. Electrochem. Soc.*, **141**, 945 (1994).
17. T. P. Moffat, G. R. Stafford, and D. E. Hall, *J. Electrochem. Soc.*, **140**, 2779 (1993).
18. T. P. Moffat, *J. Electrochem. Soc.*, **141**, L115 (1994).
19. T. P. Moffat, *J. Electrochem. Soc.*, **141**, 3059 (1994).
20. W. Obretenov, U. Schmidt, W. J. Lorenz, G. Staikov, E. Budevski, D. Carnal, U. Muller, H. Siegenthaler, and E. Schmidt, *J. Electrochem. Soc.*, **140**, 692 (1993).
21. J. Robinson and R. A. Osteryoung, *J. Electrochem. Soc.*, **127**, 122 (1979).
22. R. T. Carlin, W. Crawford, and M. Bersch, *J. Electrochem. Soc.*, **139**, 2720 (1992).
23. C. L. Hussey and T. M. Laher, *Inorg. Chem.*, **20**, 4201 (1981).
24. R. T. Carlin, P. C. Truelove, and H. C. DeLong, *J. Electrochem. Soc.*, **143**, 2747 (1996).
25. C. L. Hussey and X-H. Xu, *J. Electrochem. Soc.*, **138**, 1886 (1991).
26. B. Scharifker and G. Hills, *Electrochim. Acta*, **28**, 879 (1983).
27. T. P. Moffat, *J. Electrochem. Soc.*, **141**, 3059 (1994).
28. X-H. Xu and C. L. Hussey, *J. Electrochem. Soc.*, **139**, 1295 (1992).
29. X-H. Xu and C. L. Hussey, *J. Electrochem. Soc.*, **140**, 618 (1993).
30. C. L. Hussey and X. Xu, *J. Electrochem. Soc.*, **138**, 1886 (1991).
31. R. J. Gale, B. Gilbert, and R. A. Osteryoung, *Inorg. Chem.*, **18**, 2723 (1979).
32. T. M. Laher and C. L. Hussey, *Inorg. Chem.*, **21**, 4079 (1982).
33. S. Pye, J. Winnick, and P. A. Kohl, *J. Electrochem. Soc.*, **144**, 1933 (1997).
34. B. J. Piersma and J. S. Wilkes, Technical Report FJSRL-TR-82-0004, F. J. Seiler Research Laboratory, U. S. Air Force Academy, CO (1982).
35. X-H. Xu and C. L. Hussey, *J. Electrochem. Soc.*, **139**, 3103 (1992).
36. W. R. Pitner, Ph. D. Dissertation, The University of Mississippi, University, MS (1997).

37. H. C. DeLong, J. S. Wilkes, and R. T. Carlin, *J. Electrochem. Soc.*, **141**, 1000 (1994).
38. J. Mostany, J. Parra, and B. R. Scharifker, *J. Appl. Electrochim.*, **16**, 333 (1986).
39. L. Heerman and W. D'Olieslager, in *Proceedings of the Ninth International Symposium on Molten Salts*, C. L. Hussey, D. S. Newman, G. Mamantov, and Y. Ito, Editors, PV 94-13, p. 441, The Electrochemical Society Proceedings Series, Pennington, NJ (1994).
40. W. R. Pitner, C. L. Hussey, and G. R. Stafford, *J. Electrochem. Soc.*, **143**, 130 (1996).
41. R. T. Carlin, P. C. Truelove, and H. C. De Long, *J. Electrochem. Soc.*, **143**, 2747 (1996).
42. B. J. Tierney, M. S. Thesis, The University of Mississippi, University, MS. (1996).
43. M. Matsunaga, T. Kitazaki, K. Hosokawa, S. Hirano, and M. Yoshida, in *Proceedings of the Ninth International Symposium on Molten Salts*, C. L. Hussey, D. S. Newman, G. Mamantov, and Y. Ito, Editors, pp. 422-425, The Electrochemical Society, Inc., New Jersey (1994).
44. M. Rostom, A. Nishikata, and T. Tsuru, *Electrochim. Acta*, **42**, 2347 (1997).
45. G. R. Stafford, *J. Electrochem. Soc.*, **141**, 945 (1994).
46. T. P. Moffat, G. R. Stafford, and D. E. Hall, *J. Electrochem. Soc.*, **140**, 2779 (1993).
47. G. R. Stafford, *J. Electrochem. Soc.*, **136**, 635 (1989).
48. T. P. Moffat, *J. Electrochem. Soc.*, **141**, L115 (1994).
49. B. V. Ratnakumar, S. Di Stefano, and G. Halpert, *J. Electrochem. Soc.*, **137**, 2991 (1990).
50. T. P. Moffat, *J. Electrochem. Soc.*, **141**, 3059 (1994).
51. M. Fleischmann, R. D. Armstrong, and H. R. Thirsk, *Trans. Faraday Soc.*, **61**, 514 (1965).
53. P. Allongue and E. Souteyrand, *J. Electroanal. Chem.*, **286**, 217 (1990).
54. B. R. Scharifker and G. Hills, *Electrochim. Acta*, **28**, 879 (1983).
55. Y. P. Lin and J. R. Selman, *J. Electrochem. Soc.*, **140**, 1299 (1993).

56. E. Budevski, G. Staikov, and W. J. Lorenz, *Electrochemical Phase Formation and Growth: An Introduction to the Initial Stages of Metal Deposition*, VCH Publishers, New York (1996).
57. G. J. Hills, D. J. Schiffrin, and J. Thompson, *Electrochim. Acta*, **19**, 657 (1974).
58. A. Milchev, B. R. Scharifker, and G. J. Hills, *J. Electroanal. Chem.*, **132**, 277 (1982).
59. A. Milchev, E. Vassileva, and V. Kertov, *J. Electroanal. Chem.*, **107**, 323 (1980).
60. B. R. Scharifker, *Electrochemistry in Transition*, Oliver S. Murphy, Editor, pp. 499-508, Plenum Press, New York (1990).
61. G. Gunawardena, G. Hills, I. Montenegro and B. Scharifker, *J. Electroanal. Chem.*, **138**, 225 (1982).
62. V. Tsakova and A. Milchev, *J. Electroanal. Chem.*, **235**, 237 (1987).
63. *Comprehensive Inorganic Chemistry*, J. C. Bailar, H. J. Emeleus, R. Nyholm, and A. F. Trotman-Dickerson, Editors, Vol. 1, pp.1003-1007, Pergamon, Oxford (1973).
64. T. Støre, G. M. Haarberg, T. E. Jentoftsen, and R. Tunold, in *Proceedings of the Tenth International Symposium on Molten Salts*, R. T. Carlin, S. Deki, M. Matsunaga, D. S. Newman, J. R. Selman, and G. R. Stafford, Editors, PV 96-7, p. 290, The Electrochemical Society Proceedings Series, Pennington, NJ (1996).
65. G. Gunawardena, G. Hills, I. Montenegro, and B. R. Scharifker, *J. Electroanal. Chem.*, **138**, 225 (1982).
66. A. R. Despic', in *Electrochemistry in Transition: From the 20th to the 21st Century*, O. J. Murphy, S. Srinivasan, and B. E. Conway, Editors, pp. 453-467, Plenum, New York (1992).
67. M. Lipsztajn and R. A. Osteryoung, *J. Electrochem. Soc.*, **130**, 1968 (1983).
68. B. R. Scharifker and J. Mostany, *J. Electroanal. Chem.*, **177**, 13 (1984).
69. C. L. Hussey, in *Chemistry of Nonaqueous Solutions Current Progress*, G. Mamantov, and A. I. Popov, Editors, pp. 236, VCH, UK (1994).
70. X-H. Xu, Ph.D. Dissertation, The University of Mississippi, University, MS (1997)
71. I. W. Sun, E. H. Ward, and C. L. Hussey, *Inorg. Chem.*, **26**, 4309 (1987).
72. A. J. Bard and L. R. Faulkner, *Electrochemical Methods: Fundamentals and Applications*, John Wiley and Sons, New York (1980).

73. J. S. Stevanovic, A. R. Despic, V. D. Jovic, *Electrochim. Acta*, **42**, 873 (1997).
74. S. Swathirajan and S. Bruckenstein, *Electrochim. Acta*, **28**, 877 (1983).
75. S. Swathirajan and S. Bruckenstein, *J. Electrochem. Soc.*, **143**, 167 (1983).
76. S. Swathirajan and S. Bruckenstein, *J. Electrochem. Soc.*, **112**, 25 (1980).
77. P. C. Andricacos, J. Tabib, and L. T. Romankiw, *J. Electrochem. Soc.*, **135**, 1172 (1988).
78. K. H. Wong, and P. C. Andricacos, *J. Electrochem. Soc.*, **137**, 1087 (1990).
79. S. Swathirajan, *J. Electrochem. Soc.*, **133**, 671 (1986).
80. V. D. Jovic, R. M. Zejnilovic, A. R. Despic, and J. S. Stevanovic, *J. Appl. Electrochem.*, **18**, 511 (1988).
81. H. Gerischer, D. M. Kolb, and M. Przasnyski, *Surf. Sci.*, **43**, 662 (1974).
82. D. M. Kolb, M. Przasnyski, and H. Gerischer, *J. Electroanal. Chem.*, **54**, 25 (1974).
83. M. J. Nicol, and H. I. Philip, *J. Electrochem. Soc.*, **70**, 233 (1976).
84. M. Hansen, *Constitution of Binary Alloys*, McGraw-Hill, New York (1958).
85. A. C. Ramamurthy, and T. Kuwana, and H. I. Philip, *J. Electrochem. Soc.*, **135**, 243 (1982).
86. H. Chang, and D. C. Johnson, *J. Electrochem. Soc.*, **136**, 17 (1989).
87. R. J Phillips, T. D. Golden, M. G. Shumsky, and J. A. Switzer, *J. Electrochem. Soc.*, **141**, 2391 (1994).
88. D. Kascheiev, *J. Chem. Phys.*, **76**, 5098 (1982).
89. A. Milchev, S. Stoyanoy, and I. L. Kaishev, *Thin and Solid Films*, **22**, 255 (1974).
90. G. Gunawardena, G. Hills, and I. Montenegro, *J. Electroanal. Chem.*, **184**, 371 (1985).
91. G. Gunawardena, G. Hills, and I. Montenegro, *J. Electroanal. Chem.*, **184**, 357 (1985).
92. J. Mostany, I. Mozota, and B. R. Scharifker, *J. Electroanal. Chem.*, **177**, 25 (1984).
93. A. Milchev and E. Vassileva, *J. Electroanal. Chem.*, **107**, 337 (1980).

94. G. Gunawardena, G. Hills, and I. Montenegro, *J. Electroanal. Chem.*, **138**, 241 (1982).